UiT The Arctic University of Norway

Faculty of Science and Technology

Network Analysis and Boosting the Distribution to Local Consumers at Northern Senja, Norway with Potential Renewable Generation using Power Flow Control

Karl Henrik Rochmann

EOM-3901 Master's thesis in Energy, Climate and Environment

June 2022

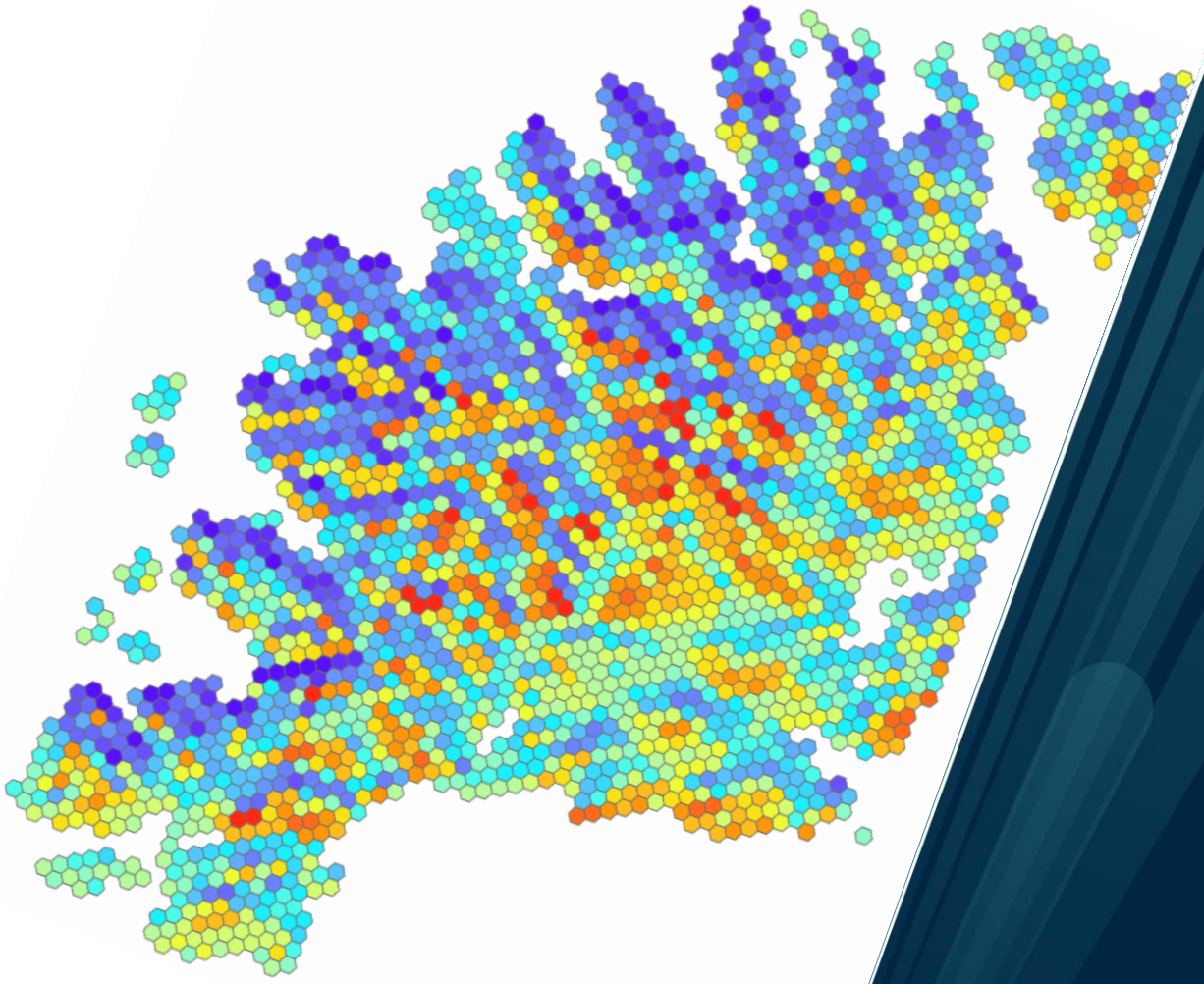

Abstract

Renewable generation and power flow control are increasing its importance for power systems. The promising development in the technology increases the efficiency for transferring energy. With increasing consumption, remote locations benefit from close laying power production due to reduced transfer losses. In these recent years, energy storage system and local renewable energy production injected into the distribution grid has increased. The use of energy storage systems to supply active power has increased its relevance, especially battery energy storage systems. Senja's power systems suffers from limited transmission transfer capacity and increasing power demand is estimated in the following years. The northern part of Senja is heavily driven by the fishery industry, which needs to expand to meet the global seafood demand. In this thesis, the distribution network is simulated with power flow control injected with the distributed renewable generation. Through simulation, the solar and wind power production on the island is quantified. In addition is battery energy storage simulated to preform peak load shaving control to reduce the voltage variations for the local fishery industry. The combined effect of energy storage system and added power production impacts on the network performance is discovered. The potential energy resources show promising results. The wind power shows results of a capacity factor on over 50 %, which is higher than the average capacity factor in Europe. The implementation of power flow control with combined energy solutions show impressive results, especially for the battery energy storage. The peak load shaving can reduce the larger loads from 40-55 %, where the smaller loads peaks reduce with 5-10 %. The voltage drops are significantly reduced during the heavy load periods, including reduction in network losses. The local network gets the highest value with a combination of solar power and battery energy storage, rising the overall voltage of 2-3 %. The networks efficiency is increased, and the frequent power failures will most likely reduce. From the results in this thesis, it is obvious to consider these components for the possibility to enhance the network performance at Senja. From the results established in this thesis, further study and analysis is proposed.

Acknowledgement

I'd like start by thanking my fellow co-students for making the studies at the University of Tromsø a memorable time. These past five years has been one of my best and most frustrating periods in my life. Even though a global pandemic made social gatherings harder, I'm forever grateful for all the good times we have shared together, both academically and personally. Throughout these five years, I have received tons of support and valuable guidance from my family. I am forever thankful for this.

I would also like to Professor Matteo Chiesa for the supervision of this thesis and teaching in subject which were custom-made for a group of students. In addition, I want to thank Ronald Hardersen for helpful guidance and getting me in touch with *Arva AS*. A huge thanks to Arva for making the thesis possible with relevant data and taking the time to listen. Thank you, Ph.D. Candidate Odin Foldvik Eikeland for supplying me with data and a quick start on AROME-Arctic.

You'll Never Walk Alone

Contents

List of Figures

List of Tables

Acronyms

AC Alternating current

ALADIN Aire Limitée Adaptation Dynamique Développement International

AM Air Mass

BESS Battery Energy Storage System

CF Capacity Factor

DC Direct Current

ECMWF European Centre for Medium-Range Weather Forecasts

EoT Equation of Time

ESS Energy Storage System

HAWT Horizontal Axis Wind Turbine

HIRLAM High Resolution Limited Area Model

HRA Sun Hour Angle

HRES High Resolution Realisation

HTESSEL Land Incorporating Land Surface Hydrology

IFS Integrated Forecast System

LMT English: Agrometeorology Norway / Norwegian: Landbruks Meteorologisk Tjeneste

LST Local Solar Time

LSTM Local Standard Time Meridian

LT Local Time

MAE Absolute Mean Error

MBE Mean Bias Error

MET The Norwegian Meteorological Institute

MPP/MP Maximum Power Point

MPPT Maximum Power Point Tracking

NCSS Norwegian Centre for Climate Services

NIBIO The Norwegian Institute of Bioeconomy Research

NOCT Nominal Operating Cell Temperature

NORCE Norwegian Research Centre

NVE English: The Norwegian Water Resources and Energy Directorate / Norwegian: Norges Vassdrags og Energidirekorat

NWP Numerical Weather Prediction

pf Power Factor

PR Performance Ratio

PV Photovoltaic

PV Photovoltaic

RMSE Root Mean Square Error

STC Standard Test Conditions

TC Time Correction

TC Time Correction

TC Time Correction

TDS THREDDS Data Servers

TSO Transmission System Operator

uf Utilization Factor

UiT The Arctic University of Norway

UTC Universal Coordinate Time

VAWT Vertical Axis Wind Turbine

Nomenclature

α	Solar Elevation Angle	degrees
$\bar{x}$	Mean Sample Value	
δ	Declination Angle	degrees
$\dot{m}$	Mass Flow Rate	kg/s
η	Efficiency	%
γ	Impedance Angle	degrees
ω	Voltage	rad/s
Φ	Azimuth Angle	degrees
ϕ	Latitude	degrees
ρ	Density	kg/m^3
σ	Sample Standard Deviation	
σ^2	Sample Variance	
θ	Phase Angle	degrees
a	Transformer Turn Ratio	
C	Capacitance	F
E	Energy	$W \cdot h$
f	Frequency	Hz
GHI	Horizontal Irradiance	W/m^2
I	Current	A
I_D	Direct Intensity	W/m^2
I_{BC}	Direct Beam Radiation Collector	W/m^2
I_{DC}	Diffuse Radiation Collector	W/m^2
I_{RC}	Reflected Radiation Collector	W/m^2
L	Inductance	H
m	Mass	kg
N	Winding Number	

P	Active Power	W
Q	Reactive Power	VAr
R	Resistance	Ω
r	Pearson Correlation Coefficient	
S	Apparent Power	VA
S_T	Thermal constraint	W
U	Voltage	V
u	Wind Speed	m/s
v	Speed	m/s
X	Reactance	Ω
Z	Impedance	Ω
z	Height	m
z_0	Surface Roughness Length	m

1 / Introduction

1.1 Background

In today's modern society, electricity is an obvious part of the regular daily life. With a significant shift towards renewable sources of energy due to the global warming and agreements such as the Paris agreement, oil and gas production has been a less favourable solution to energy production. In Norway, the consumption of electricity from 1990 to 2020 has increased 14.6 % within these 30 years. The electric energy production has on the other hand increased with 26.5 % in 30 years (1990-2020), where Norway produced roughly 154 TWh of electricity and exported ≈ 25 TWh in 2020 [SSB, 2021]. At the start of 2022, 1739 hydro power plants is installed with a combined installed capacity on 33 403 MW [NVE, 2019]. The hydro power plants produced 136.4 TWh in 2020, which is around 90 % of the total Norwegian total power production [Energy Facts Norway, 2021].

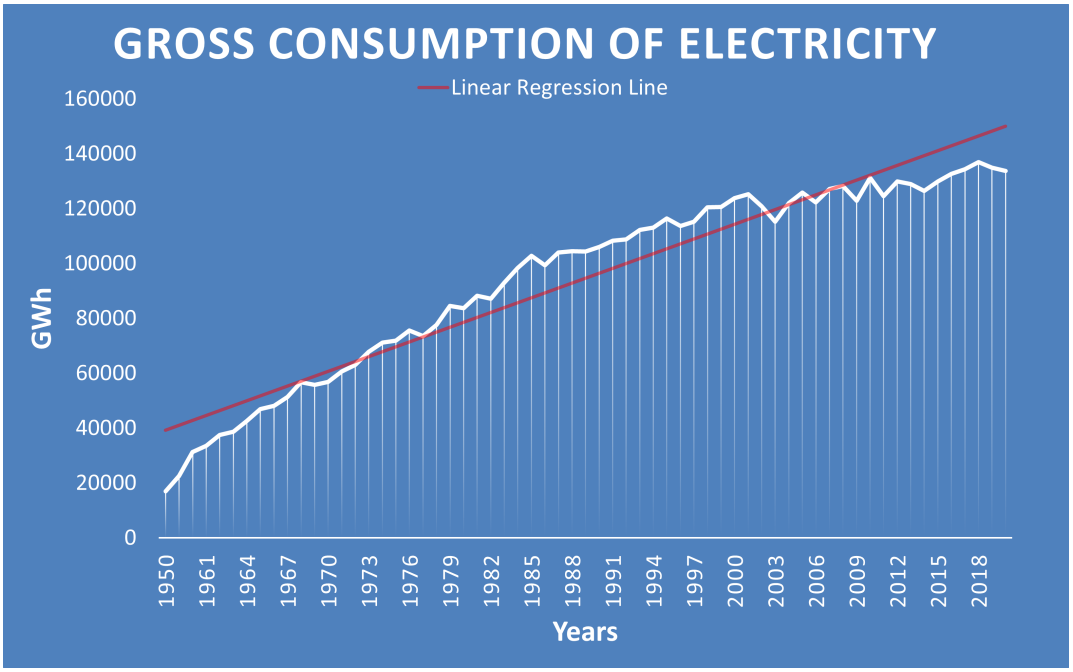

Figure 1.1: The monthly electrical production in Norway from January 2010 to September 2021 with data from SSB. The linear trend line is added, indicating an increasing trend on power production [SSB, 2021].

A steady increase in both the demand and production forces improvement on the electrical power grid and increment of energy production. As technology further advances, machinery becomes more sensitive to the electrical quality and has higher electrical requirements. Similarities could be associated with the increase of personal electrical vehicles and the amount of distribution of chargers. From the Norwegian electrical car association in 2019 around 200 000 electrical cars and 1700 fast chargers was registered, and it is expected to drastically increase in the following years [Elbilforening, 2019].

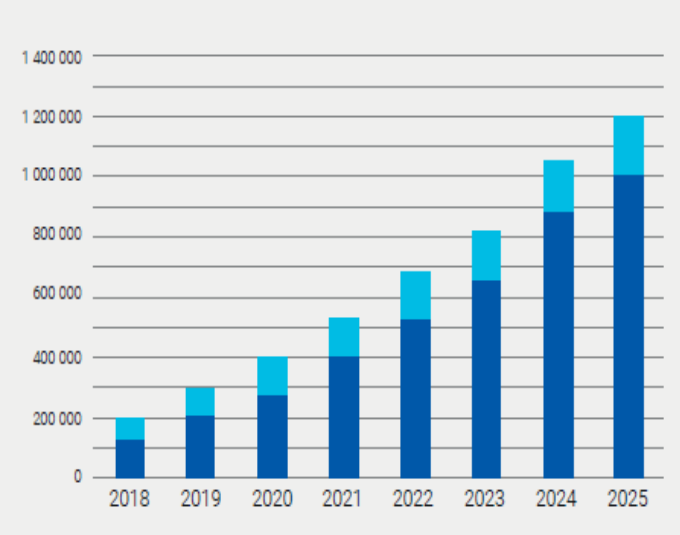

(a) An estimation on the imported and sold electrical cars towards 2025 with historical values from 2018 to 2020. The estimate predicts 1.2 million electrical cars in 2025. The light blue bars indicates the sales of new electrical cars, and the dark blue bars indicates the already registered electrical cars [Elbilforening, 2019].

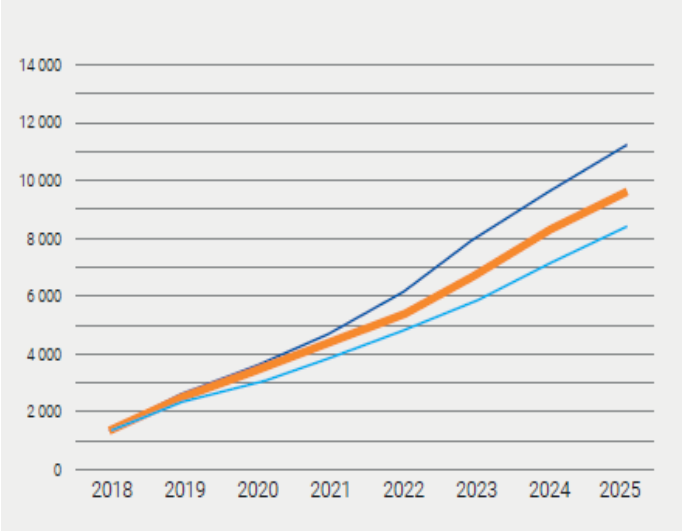

(b) An estimation on increasing demand of fast/super chargers where an estimate of 1.2 million electrical cars in 2025. Dark blue bars: 100 cars per charger, light blue bars: 150 cars per charger and orange bars: 125 cars per charger [Elbilforening, 2019].

Figure 1.2: Total electrical car and chargers in Norway towards 2025.

The increased focus on new electricity generation capability from renewable goes hand in hand with an effort to further develop our distribution system. There exist different new technologies whose integration in a the current system require a holistic thinking that can be obtained throughout the execution of pilot projects. *Troms Kraft* owns the distribution network at Senja and leads projects such as *Smart Senja*. The main goals are to utilise local terrain or use local area to harvest natural sources for energy generation, where their target is to stabilise the power distribution using different resources and techniques. Since the ongoing industry at Senja is expanding, the electrical loads increases and the distribution grid experiencing problems due to electrical instability. To localize the sources of these instabilities, the grid is becoming more digitalized and different parameters are monitored real time. *Arva* (a merged company by *Troms Kraft* and *Bodø Energi*) is the head of the project with partners [Troms Kraft, 2019].

The distribution networks are at its limits during the wild caught fishery high season, especially from January to April. The local coastal community at Senja exports enormous amounts of seafood to accommodate the global demand. An industrial expansion is necessary to meet the global demand, where electrical network capacity issues limit the expansion rate. In a rapport from *Sjømatklyngen Senja* (partnership of over 40 seafood corporation at Senja), catch-based fishery and aquaculture industry annual power consumption are expected to reach 45 500 MWh and 140 700 MWh in 2030 [Sjømaklyngen Senja, 2021]. The islands today's power supply is distributed through a 66 kV, which is close to its maximum capacity. The 22 kV distribution network is used to feed the end point, which feature long radial line networks. The end points are exposed to low voltage during heavy load periods, which results risk of instability and inadequate power supply. This can have significant consequences for the local industrial establishments, due to thigh production time frames and dependency on stable power supply for predictable production.

1.2 Scope of Study

Troms Kraft is the local power distributor for Senja. With access on data by their subsidiary Arva, an examination of possible renewable energy resources on Senja is performed. The propose is to increase the robustness of the distribution network for long radial distances at the local consumer. In this thesis renewable energy production and power flow control will be simulated. The objective is to minimise the voltage drops, and is done by limit the current flow in the transmission lines. If results are effective and acceptable, measures could be taken and reduce investment cost on the transmission lines and other necessary components. An economic analysis is not evaluated in this thesis.

The Norwegian distribution grid consist of long radial transmission lines in the distribution grid. Power over long distances get exposed to voltage drops and are in some areas at its maximum capacity. These networks rely on hydro power plants and impose high requirements for the distribution operation. By utilising local distributed generation, local injection of power production near critical locations limits the transmission distance. This would help or resolve the transmission capacity on the network which are subject to bottleneck problems. In the simulations done in this thesis, potential solar and wind production is used for application on local distributed generation. Yearly output for production is given, and four periods of 8 days is simulated for the power flow.

The photovoltaic system is set on rooftop at Husøy and Senjahopen for the fishery companies *Brødrene Karlsen AS* and *Nergård Seafood AS*. Two similar photovoltaic configurations are considered, which are orientated southwards. The rated capacity is 190 kW, 200 kW for Husøy and 380 kW, 400 kW for Senjahopen. The wind farm is located near by the fishery industri at northern Senja at a mountain ridge. Three turbines are considered where the highest installed capacity is used in power flow simulation. The three proposed farms have an installed capacity on 32 MW, 12 MW and 3.2 MW. The yearly performance will be evaluated and the performance on injection into the network. The objective is to study the potential released capacity power plant can achieve. The fishery industry expect to expand their production, where transfer capacity is going to be crucial for the future.

As transfer capacity is distributed in the radial network, the island is constrained, especially the northern part. External influence such as wind gust, load pattern constrains the network. Thermal capacity is not considered to be a problem, and wind gust are not considered during simulation. The power flow control simulation will be conducted with already mentioned system in addition to a battery storage system. The purpose of this study is to reduce power losses and increase voltage regulation during high load patterns. The increased performance on higher voltages can reduce investments, increase components lifetime and enable sustainable grid operations on the existing network.

1.3 Outline of the Thesis

The thesis is divided into the following chapters, excluding the introduction:

- **Chapter 2** - Theoretical background on the subject related to this thesis. This chapter provide necessary knowledge on theory related to power systems and renewable energy sources.
- **Chapter 3** - The chosen location for this case study in this thesis. It contains brief information about the fishery industry location, power failure log and the existing distribution network with the existing hydro power plants. In addition, key points from an investigation from *Arva* introduced.
- **Chapter 4** - Introduction on methods used, where statistical methods is presented including the different data used in the thesis.
- **Chapter 5** - The potential output from the performance of renewable energy sources and discussion of the results.
- **Chapter 6** - The results from the network power flow control improved performance and discussion of the proposed components.
- **Chapter 7** - Summary of the results, concluding remarks and discussion on further work.

2 / Theoretical Background

2.1 The Norwegian Transmission and distribution grid

The transmission grid/network is the backbone of transferring power from electrical generation to the end users. The electrical transmission amount is delivered using alternating current (AC) or direct current (DC). The vast majority of the world uses aerial lines of three phase AC, where several voltage magnitudes are utilise in order to transfer power most efficient and cost effective [Nagsarkar and Sukhija, 2014]. The Norwegian transmission grid is mainly divided into three categories [Energy Facts Norway, 2019]:

- **Transmission Grid** - The grid connects producers with users nationwide and is also interconnected with other nations. The designated transmission system operator (TSO) is *Statnett*, which is state owned by the Norwegian government. The transmission grid has the highest level of voltages, which is 420 kV, 300 kV and 132 kV. Due to long distances transferring of power, the high voltage is set to limit power losses.

- **Regional Grid** - The grid is often used to link the transmission grid to the distribution grid. In some cases, there is production included to fed higher voltages to the consumption radials. The regional grid carries voltages of 33 kV up to 132 kV.

- **Distribution Grid** - It's the local electrical grids which supply power to smaller end users. Carrying voltages up to 22 kV, where its divided high-and low voltage segments. The dividing segments consist of voltages of 1 kV (high) and 400 V or 230 V (low). It's mostly featured in a radial structure, often having voltage drops. If the operation of the distribution grid is exposed new high loads and pattern, fluctuations will cause instability [Nagsarkar and Sukhija, 2014].

Figure 2.1: Top: The Norwegian transmission grid [NVE, 2021]. Bottom: An illustration on how the power is distributed [BKK, 2021].

2.2 Power

In this section, the key characteristics of transmission network will be presented and the function of the parameters. The equivalent circuit for a single-phase transmission line is shown in figure 2.2. The grid impedance consist of the resistance in the cable $R = U/I$, which follows Ohm's law. The reactants X consists of both capacitance C, inductance L and are non-linear, creating a phase shift for voltage and current. If the current is leading the voltage by 90°, it's a purely capacitive circuit. If the current is lagging by the voltage by 90°, the circuit is purely inductive, shown in figure 2.4. The capacitance and inductance occur due to its magnetic and electric fields around the electric conductor (transmission line). L and C do not contribute to the active power transfer, but deliver an alternate power S in an opposite manner to each other and are the source of reactive power Q. This create an alternating current (AC) system, where the power is *complex* [Nagsarkar and Sukhija, 2014].

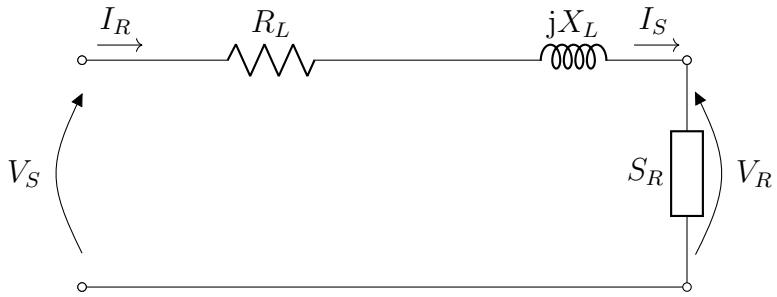

Figure 2.2: Single phase circuit sketch of a transmission line, inspired by [Saadat, 2010].

The reactants can be calculated as $X_L = \omega L$ (inductance) and $X_C = 1/\omega C$ (capacitance), but its often used a complex notation on these to calculate in polar form, $X_L = j\omega L$ and $X_C = 1/j\omega C$, where $\omega = 2\pi f$ and f is the frequency.
The total impedance Z can then be calculated as $Z = R + jX$, where j is the imaginary unit for the complex numbers (i mixes with current symbol occurs). The calculation of the circuit 2.2 can also be given in matrix form [Nagsarkar and Sukhija, 2014]:

$$\begin{bmatrix} V_s \\ I_S \end{bmatrix} = \begin{bmatrix} 1 & Z \\ 0 & 1 \end{bmatrix} \begin{bmatrix} V_R \\ I_R \end{bmatrix} \tag{2.1}$$

The active power (P) is defined as the true power or the power that is being utilised in an AC system. The reactive power (Q) is the power that oscillates back and forth in a system, meaning reactive power is not utilised. The apparent power (S) is the product of root mean square (RMS) value of voltage and current. From the power triangle in figure 2.3, the different powers can be

calculated as:

$$\begin{aligned} P &= UI \times \cos\theta \\ Q &= UI \times \sin\theta \\ S &= P + jQ = UI^* = \sqrt{P^2 + Q^2} \end{aligned} \tag{2.2}$$

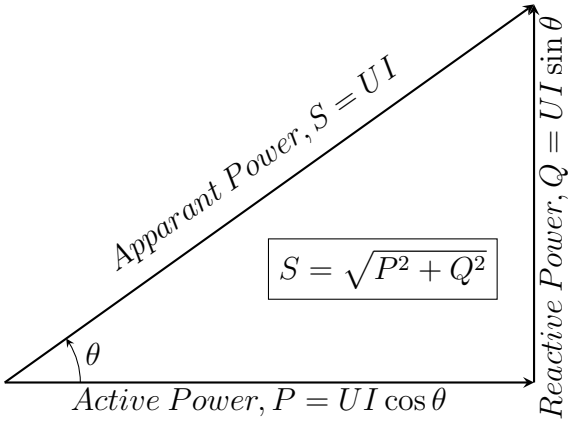

Figure 2.3: A power triangle, formed by the power components. The power factor is $\cos\theta$, where θ is the phase angle [Nagsarkar and Sukhija, 2014]

The resistance and reactance forms a relation on if the lines is resistive or inductive. The impedance phase angle γ can be found in different ways, using figure 2.3 or the relation which is expressed as [Saadat, 2010]:

$$\gamma = \arccos\left(\frac{R}{|Z|}\right) = \arccos\left(\frac{P}{S}\right) = \arccos(\theta) \tag{2.3}$$

The inductance and reactance are depends on different parameters. Inductance in lines is influenced by the flux linkage between conductors, where the magnitude is proportional with the phase. Reactance in lines is determined by the conductivity of the line length, conducting material and cross section area of conducting material. The active power losses (P_L) for the transmission lines is due to line resistance, therefore the real three phase power losses are expressed as [Saadat, 2010]:

$$P_{L(3\phi)} = 3I^2R = \frac{3R}{U^2}\left(P^2 + Q^2\right) \tag{2.4}$$

As seen in equation 2.4, the power losses in inversely proportional to the voltage squared. Transporting power at very high voltages will then decrease the power loss. In order to amplify the voltage, transformers are used to step up the voltage to a certain level. Typically, voltage is stepped up at electrical generation and steps the voltage down to the appropriate level for usage. The voltage is changed using a *turn ratio* (a), which is descibed as [Nagsarkar and Sukhija, 2014]:

$$a = \frac{U_1}{U_2} = \frac{N_1}{N_2} \tag{2.5}$$

U_1 is denoted as the primary side and U_2 is the secondary side voltages. The subscript i represent their representative side and N is the winding number. Transformers have the ability to change these number of winding's by using different methods. A short explanation of the methods is to change connecting taps, which allow for variable turn ratios to be selected. Voltages taken to an extremely high level is exposed to losses through such as the corona effect, which is an electrical discharge caused by the ionization of air or a fluid surrounding the conductor [Nagsarkar and Sukhija, 2014].

The apparent power in transmission lines is limited to a specific flow due to heat generated as power losses, causing the lines to stretch with increased loads (non-uniform lines). Dangling transmission lines might cause damage and are considered as irreversible; therefore a thermal constraint is defined to prevent dangling lines. To prevent reducing the lifetime of components, the thermal constraint on power flow is expressed in 2.6. Where U and I_T are per phase values [Saadat, 2010].

$$S_T = 3U \cdot I_T \tag{2.6}$$

2.2.1 Voltage Drop in Transmission Lines

As shown earlier in figure 2.2, the current which flows through the transmission lines induces a potential in the opposite direction of the current's directions. Due to opposite directions, voltage will reduce with the length of the line. There are multiple transmission lines models available, where some are more complex and are more fitting to long distance transfer of high voltages. A linear approximation for lines >80 km is called short-length lines model, consist of the receiving current I_R, sending current I_S, where the conducting material is assumes to be uniform. The lines will have in series a resistance R_L and a inductance jX_L, where V_R and V_S is the receiving and sending voltages. The receiving end apparent load power is S_R, which is affected of the voltage drop across the line [Nagsarkar and Sukhija, 2014].

Regulation of the voltage is dependent on the line impedance and a power factor (pf) at loads, which is defined as the ratio of apparent to active power consumption. The reactive power consumption sign will determine if a load is leading or lagging power factor. If reactive power is consumed at a load, the reactive power is inductive and is lagging. If reactive power is injected into the grid, the reactive power is capacitive and is leading [Masters, 2013]. Considering a single line, a capacitive load has opposite flow direction relative to the power flow which will grant a rise in line voltage. The current increases as well, thus will some active power be lost due to this effect.

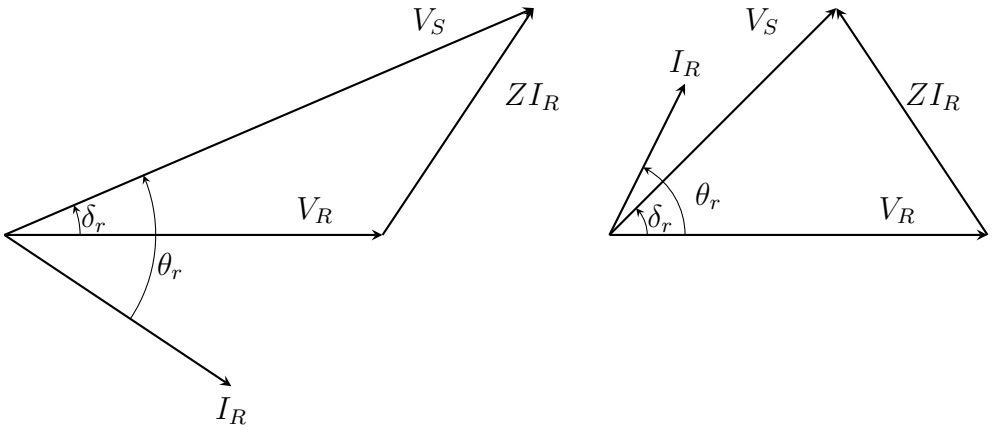

Figure 2.4: Left: Phasor diagram for a lagging pf load. Right: Phasor diagram for a leading pf load. Image is inspired by [Saadat, 2010].

Where δ_r is the difference in voltage phase angle between sending and receiving end. θ_r is the angular difference between current and voltage phasors. If a power factor is lagging or leading, an unwanted voltage characteristics is present and some compensation is required [Saadat, 2010].

2.2.2 Network Strength

The distribution network strength is a measurement of the stability based on the short circuit performance at a point. The measurement can determine if a network is considered strong or weak. Short circuit performance with a value on less than 1.1 kA is considered weak and typically are characterised by a high impedance. The high impedance will expose the voltage at the point to be more sensitive to changes in demand or production [Kirkeby and Seljeseth, 2014]. There is found for Norway a substantial number of distribution networks categorised as weak networks or has a short circuit performance lower than 1.1 kA [DNV, 2019].

2.2.3 Norwegian Power Quality Regulation

To ensure a standard for the electrical power users, regulation on power quality is present. The Norwegian power system delivers a satisfactory quality regardless of where they live. *NVE* (Norges Vassdrags og Energidirekorat) has formulated some key regulations concerning power quality, which are [Olje- og energidepartementet, 2020]:

- **Slow variations in voltage magnitude** - At the low voltage network, the slow voltage variations need to be within a range of ±10 of the nominal voltage. The variation needs to measure as an average over one minute in the common low voltage point. High voltage networks, 11 kV and 22 kV, are only permitted to have a maximum stationary voltage drop on 5 % when transmitting power.
- **Over-voltages, under-voltages and voltage changes of low duration** - The number of occurrences deviated of 3 % over steady state voltage, or 5 % over maximum allowable voltage must not exceed 24 occurrences in 24 hours.
- **Voltage asymmetry** - The Asymmetry between phases in the network should not exceed 2 % on average over a 10-minute period.

2.3 Hydropower

Hydropower takes advantage of flowing water from a water reservoir which stores potential energy due to its height difference from top to the outlet. By pressuring water through the intake which flows in an connected penstock will drive a electrical generator. The goal is transfer of hydroelectrical power plant is to transfer as much as possible into useful electrical power in an optimal way. A schematic of a typical hydroelectric power plant is illustrated in figure 2.5

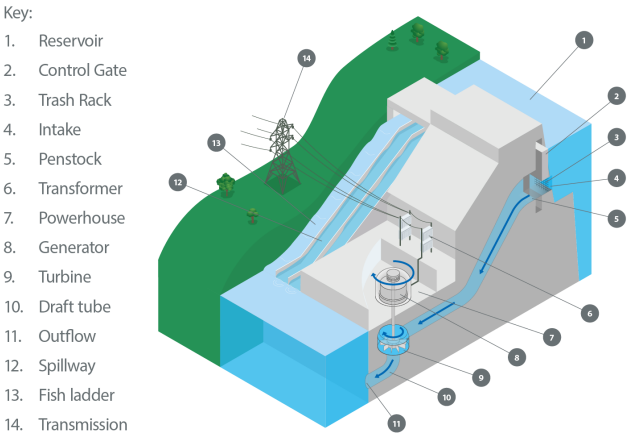

Figure 2.5: A typical schematic of a Hydroelectric Power Plant, figure is from www.hydropower.org.

The electrical conversation from mechanical rotation is done by using a turbine/electrical generator. These generators are synchronous generators, which uses the electromagnetic principle to generate electricity [Masters, 2013]. This thesis does not describe the generators functions in details. Large amount of water is usually kept in reservoirs to provide energy dispatch by letting water flow in response on load changes over a period. Since reservoirs are able to keep large amounts, the hydro plant is relatively cheap due low operation cost and minimal impact on the environment. However, a construction of a dam/artificial reservoirs requires high capital cost and is more destructible to the environment instead of a natural reservoirs. Construction of a dam could have serious social and environmental consequences due to impact on displacement of population and water quality [Andrews et al., 2021].

2.3.1 Power Output of Hydroelectric Power Plant

When considering a hydroelectric power plant there are some key parameters to address. A key parameter is the *head* of a dam, which is the vertical distance between the upper level in the reservoir and the turbine. This parameter is strongly correlated to power output and are important in choice of turbine type. For low/medium head dams, Francis or Kaplan turbine is typically

used. These turbine utilises large volume flow rates, and spins relatively slowly. For large head dams, typically Pelton turbine are used, due to small volume flow rates and spins relatively fast. Figure 2.6 shows what turbine type which is typically used with given head and volume flow rate. Water flows through the *penstock* towards the turbine having a flow rate, where the turbine is completely submerged into the water. Potential energy is converted to kinetic energy creating a flow, where the kinetic energy is transferred into mechanical energy forcing the turbine to spin [Andrews et al., 2021].

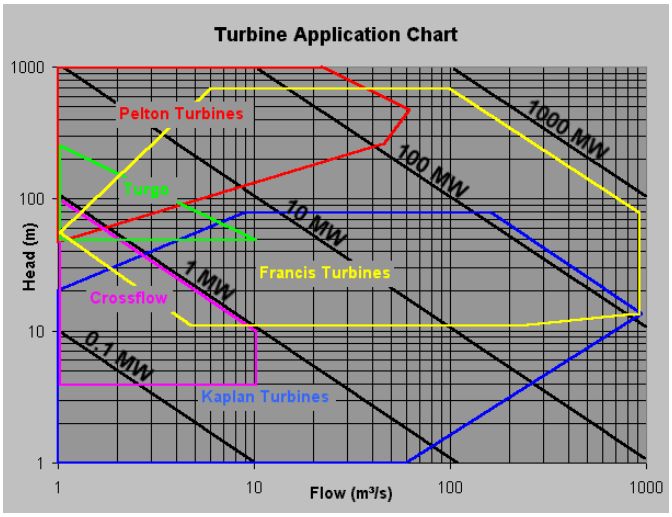

Figure 2.6: A schematic on which turbine type to choose, based on head and flow. Image is from https://en.wikipedia.org/wiki/Water_turbine.

The power output can be defined as these energy conversions. The potential energy from the water is expressed as $E_P = \rho_w g h$. The density (ρ_w) of the water given in kg/m^2. The water fed through the intake flowing through the penstock to the turbine is the volume flow rate Q, which is given as volume per unit time m^3/s. In this process losses will occur due to friction, turbulence, and other external forces. The losses in conversation to mechanical power is tiny, therefore are they considered insignificant. The total loss can be expressed as an efficiency constant η_h, where its typically around 90 % [Andrews et al., 2021]. The total power output for a hydroelectric power plant becomes:

$$P = \eta_h \rho_w g h Q \tag{2.7}$$

2.3.2 Control of Power Output

As mentioned in section (2.3), the goal is to transfer as much energy as possible in an optimal way. Owners of the plant primarily optimise the production in favour of maximising economical profit or network stability (to meet requirements). The hydro plant systems output is controlled by a governor system. The system regulates the intake gate, where the position is altered to regulate

the flow rate which control the power output. If a reaction turbine is used, blades can be adjusted to slow down the rotational speed of the turbine. If an impulse turbine is used, valves can adjust their outlet to alter the turbines rotational speed. By continuously monitoring key parameters such as frequency, voltage waveform, the regulation control is optimised in terms with the owner's strategy [Andrews et al., 2021], [Machowski et al., 2008].

2.4 Solar Radiation

The solar radiation which radiates on the Earth's atmosphere is almost constant. At the terrestrial level (earths surface), it is more complicated. The radiation may vary due to several different factors, this is such as atmospheric effects, local variations, weather, season of the year, etc. When the gases, dust and aerosol in the atmosphere absorbs some of the radiation energy, the light will also scatter (Rayleigh scattering), which makes us differentiate between diffuse and direct radiation.

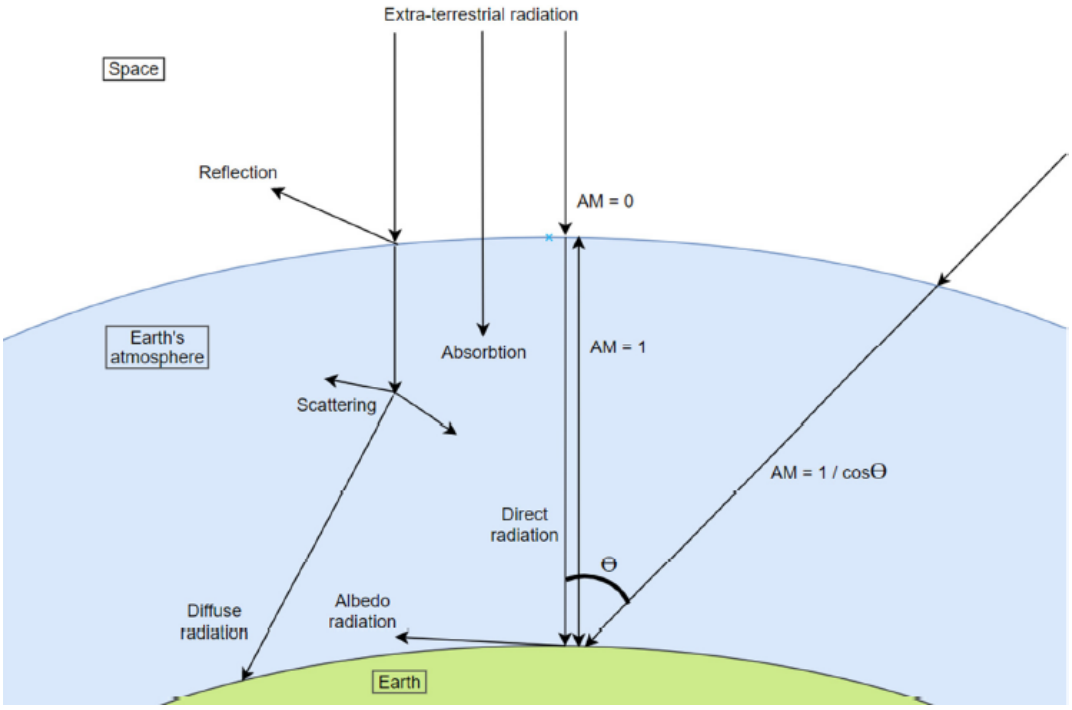

Figure 2.7: The extra-terrestrial radiations interaction on the atmosphere. Illustration is made by [Løvvold, 2020]

To represent the shortest pathway on for the light travels, Air Mass (AM) was defined. It tells the reduction of the energy due to atmosphere; this means AM0 has no atmosphere and AM1 travels at a perfectly straight overhead with an angle at 0° ("one atmosphere"). The AM value is calculated using equation 2.8,

$$AM = \frac{1}{\cos\theta} = \sqrt{1 + \left(\frac{s}{h}\right)^2} \tag{2.8}$$

Where θ is the incoming angle of the light from the sun. Another way to calculate AM is using the length of the shadow of an object (s), the height (h) and use Pythagoras's theorem.

The use of AM value can determine the of the direct intensity on a component throughout the day in equation 2.9.

$$I_D = 1.353 * 0.7^{AM^{0.678}} \tag{2.9}$$

The values given in the equation above arrives from the solar constant 1.353 (kW/m^2), and about 70 % of the direct light gets transmitted to the earth's surface. The power term 0.678 arrives from an empirical fit to observed data, and it takes non-uniformities in the atmospheric layers into account [Masters, 2013].

2.4.1 Solar Path

Including to the characteristic of the solar radiation, the position to the sun relative to the earth is a major factor to the amount of received radiation. Since the Earth rotates around its own axis, time of day changes, the highest point of the sun on the horizon vary from local time (LT) since noon is defined as 12 o'clock. The reason for the difference in time is due to geographical properties such as longitude within time zones [Honsberg and Bowden, 2019]. To differentiate between LT and the Local Solar Time (LST) a certain reference point for every time zone is applied, named *Local Standard Time Meridian* (LSTM). This value is calculated as [Honsberg and Bowden, 2019]:

$$LSTM = 15^\circ \cdot \Delta T_{UTC} \tag{2.10}$$

Where ΔT_{UTC} is the difference of the Local Time (LT) from Universal Coordinated Time (UTC) in hours. Finding LST is given as:

$$LST = LT + \frac{TC}{60} \tag{2.11}$$

Where TC is the Time Correction Factor (in minutes), which is an equation depending on Longitude and the eccentricity of the earth's orbit. The calculation of TC is given in appendix A.4.3 [Honsberg and Bowden, 2019]. To further look at the LST, it can be converted into the Sun Hour Angle (HRA) given in degrees. The measurement is the angle away from noon (0°), which implies the morning value is negative. To find HRA, the equation is given as [Honsberg and Bowden, 2019]:

$$HRA = 15^\circ(LST - 12) \tag{2.12}$$

The earth orbits around the sun, creating seasonal changes. The earth spins around its axis with a tilt on 23.5° relative to the earth's orbit plane.To calculate the irradiance on the horizon, the declination angle δ need to be quantified. The formula for δ is given as [Honsberg and Bowden, 2019]:

$$\delta = 23.45° \sin\left(\frac{360}{365} \cdot (d + 284)\right) \tag{2.13}$$

From our reference point on the earth's surface, some quantities need to be addressed to point out the necessary solar path. With the information in this section, two angles are important to calculate.[Honsberg and Bowden, 2019]

- **Elevation angle** ($\boldsymbol{\alpha}$) - The elevation angle describes the angular height on the sun beam measured from the horizon. It is related to the zenith angle as $\alpha = 90° - \theta_Z$, where α is given in 2.14 [Honsberg and Bowden, 2019].
- **Azimuth angle** ($\boldsymbol{\Phi}$) - The Azimuth angle described the compass direction from where the sun beam radiates from. Φ is given in 2.15 [Honsberg and Bowden, 2019].

Underneath the elevation angle of a certain time of day is given,

$$\alpha = \arcsin\left[\sin(\delta)\sin(\phi) + \cos(\delta)\cos(\phi)\cos(HRA)\right] \tag{2.14}$$

and the azimuth angle at any given time, where ϕ is the longitude of the location of interest [Honsberg and Bowden, 2019].

$$\Phi = \arccos\left[\frac{\sin(\delta)\cos(\phi) - \cos(\delta)\sin(\phi)\cos(HRA)}{\cos(\alpha)}\right] \tag{2.15}$$

2.4.2 Incline Surface Insolation

The elevation angle can be used to calculate the amount of solar radiation incident on an incline surface. Due to the incident of solar radiation on the tilted module, the radiation is perpendicular. The geometry of the solar modules and solar radiation is given in figure A.7. The solar elevation angle could then be expressed as $\alpha = 90 + \delta - \phi$, where ϕ is the given latitude [Honsberg and Bowden, 2019]. The radiations are divided into three categories, direct beam radiation, diffuse radiations and reflected radiation. Direct beam radiations are the beam insolation (I_B) striking the collectors capture side. By addressing the the solar elevation an azimuth angles an incident angle ($\cos\theta$) is possible to calculate [Masters, 2013].

$$\cos\theta = \cos\alpha\cos\left(\phi_S - \phi_C\right)\sin\theta_T + \sin\alpha\cos\theta_T \tag{2.16}$$

Where θ_T is the angle of the incline surface, ϕ_C collector azimuth and ϕ_S solar azimuth (measured relative to south, where positive ϕ_C is easterly and positive is westerly direction). The direct beam insolation on the collector is expressed as [Masters, 2013]:

$$I_{BC} = I_B \cos\theta \tag{2.17}$$

The diffuse radiation is defined as $I_{DH} = I_B C$, where C is a sky diffuse factor where the formula is given in appendix A.4.2. Since the diffuse radiation scatter around and eventually is captured and collected only half is absorbed unless a module has bifacial collectors. Therefore, a coefficient of the I_{DH} is given as $(\frac{1+\cos\theta_T}{2})$, hence the equation [Masters, 2013]:

$$I_{DC} = I_{DH}\left(\frac{1+\cos\theta_T}{2}\right) = I_B C\left(\frac{1+\cos\theta_T}{2}\right) \tag{2.18}$$

The reflected radiation (I_{RC}) is a portion of the radiations which scatter on the surface and reflect radiation. The amount which being reflected is given as a parameter so-called ground reluctance or albedo (ρ) ranging from 0 to 1, where 1 is full reactance. Fresh snow has around 0.8 and 0.1 for gravel-roofs. Since both direct and diffuse radiation reflects on a type of surface, the collected radiation on the incline surface is given as [Masters, 2013]:

$$I_{RC} = \rho\left(I_{BH} + I_{DH}\right)\left(\frac{1+\cos\theta_T}{2}\right) = \rho I_H\left(\frac{1+\cos\theta_T}{2}\right) = I_B\rho\left(C+\sin\alpha\right)\left(\frac{1+\cos\theta_T}{2}\right) \tag{2.19}$$

The total insolation on the collector is therefore [Masters, 2013]:

$$I_C = I_{BC} + I_{DC} + I_{RC} \tag{2.20}$$

2.5 Photovoltaic Cells

Photovoltaic cells also known as PV, is a material which has the ability to convert the energy contained in the photons into electric voltage and current. The making of a PV-cell is by using the material of semiconductors, which conducts electrons when excited by the photon to the conduction band. When electrons get excited by a high energy photon to the conduction band, it leaves an empty slot refereed as a *hole*. The electron which is exited to the conduction band is referred to as a *carrier* [Masters, 2013].

The amount of the carrier concentration is entitled *Intrinsic Carrier Concentration*. The number of carriers is dependent on the band gap of the material and on the temperature of the material [Honsberg and Bowden, 2019]. To shift the balance in the chosen material, a process called doping will purposely apply impurities to the crystal lattice. When the electrons are the major carriers and holes are the minority carriers, the material is n-doped. When its opposite, electrons are the minority carriers and holes the major carriers, the material i p-doped. Combining both material to a p-n junction, an electric field exist between p-side and n-side, creating a drift current of electrons. Therefore, when solar cells absorbs light, the photons may hold higher energy than the band gap, which gives the opportunity to excite electrons [Honsberg and Bowden, 2019].

With the PV cells flowing through an external circuit under illumination it's described in the following IV-equation [Masters, 2013].

$$I = I_{sc} - I_0(e^{qV/kT} - 1) \tag{2.21}$$

Where I_{sc} is the short-circuit current which is the maximum current the PV cell can produce, and I_0 is the so called "dark current" (no illumination)). q is the electron charge on $1.602 \cdot 10^{-19}$C, k is the Boltzmann constant ($k = 1.381 \cdot 10^{-23}$) [Masters, 2013].

The equivalent circuit for a solar PV cell is described most accurate with a resistance in series (R_s) and a shunt resistance (R_{sh}). The resistances will adjust the IV-curve, which impacts a drop in current of magnitude $\frac{V}{R_{sh}}$ and voltage shift by IR_s [Masters, 2013]. To reduce the effect of the internal resistance in a cell, R_{sh} should be as high as possible. This will limit current to pass through the resistance R_s [Honsberg and Bowden, 2019]. A schematic of the equivalent circuit is given in figure 2.8.

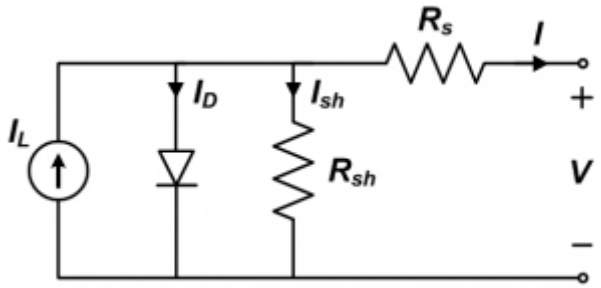

Figure 2.8: Equivalent circuit for a PV cell with series and shunt resistance. The figure is from pvpmc.sandia.gov.

To calculate the total current from the equivalent circuit, the resistance is taken into account and an extension of 2.21 is required. The cell current is given as [Honsberg and Bowden, 2019]:

$$I = I_{ph} - I_0(e^{q(V-IR_s/kT} - 1) - (\frac{V + IR_s}{R_s h}) \tag{2.22}$$

Here I_0 is the diode reverse saturation current. To solve for I_{sc}, $V = 0$ and to solve the open-circuit voltage (V_{OC}), $I = 0$. These conditions give the highest obtainable values, and the dynamic can be summarised in an IV-curve for the cell.

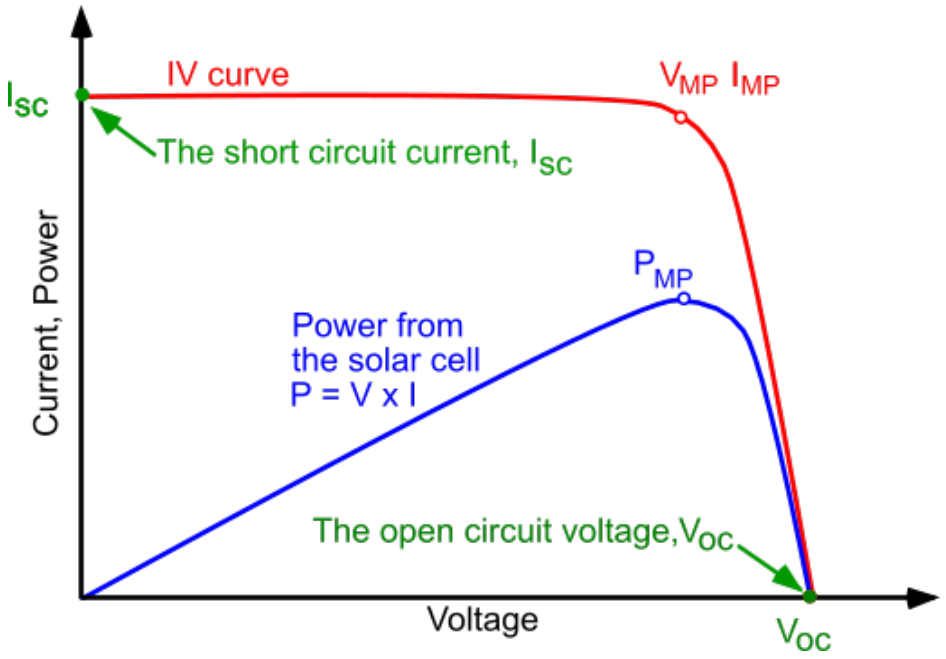

Figure 2.9: Typical IV curve for a PV cell, with the maximum power point. Figure is from [Honsberg and Bowden, 2019]

2.5.1 Maximal Power Point Tracking

For a PV system to get the maximum power production, a process called *Maximum Power Point Tracking* (MPPT) is necessary. By adding a *buck-boost converter* to alter the DC voltage, to a magnitude which is most optimal to the IV characteristics. The algorithm for the tracking exists in several variations, including the dP/dV and dP/dI feedback control loops. The feedback loops are indirect tracking since the utilize algoritems, but indirect tracking uses true I-V data to determine the true maximum power point (MPP/MP) [Masters, 2013].

2.5.2 PV characteristics

Fill factor is an essential measurement for the quality of a PV cell. It describes the ratio between maximum power output (P_{max}) from the solar cell and the product of the open-circuit voltage (V_{OC}) and short-circuit current (I_{SC}). The fill factor can be expressed as [Smets et al., 2015]:

$$FF = \frac{P_{max}}{I_{SC}V_{OC}} = \frac{I_{mpp}V_{mpp}}{I_{SC}V_{OC}} \tag{2.23}$$

The conversation efficiency of the PV cell is defined as the ratio between the maximal generated power and the incident radiation power (S_{in}). The efficiency η is expressed as:

$$\eta = \frac{P_{max}}{S_{in}} = \frac{I_{mpp}V_{mpp}}{S_{in}} = \frac{I_{SC}V_{OC}FF}{S_{in}} \tag{2.24}$$

It's typical to test the solar cells under the standard test conditions (STC), where the incident light is AM1.5 and has a constant irradiance on 1000 W/m^2. In figure 2.10 the years of development of solar cells show the increase in the cell efficiencies [Smets et al., 2015].

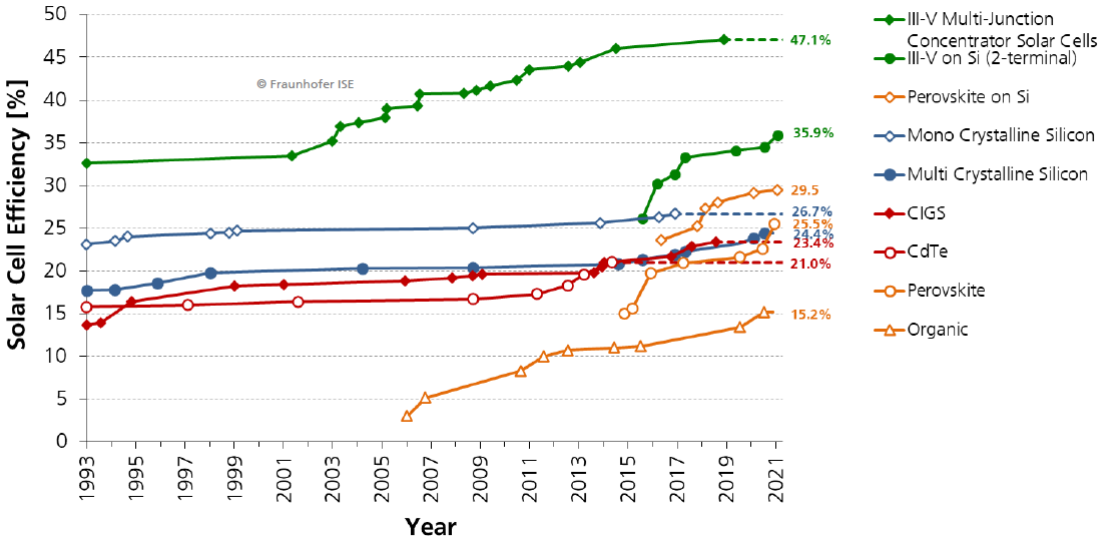

Figure 2.10: The progress of different techniques on development of laboratory solar cell efficiencies. Figure is produced by [Fraunhofer Institute for Solar Energy Systems, 2022].

In solar cells, there is a theoretical limit called *Shockley-Queisser limit*. The limit will define the maximum conversation in a single-junction direct bandgap cell. With a spectrum on AM1.5 with a bandgap at 1.34 eV, the limit is calculated in [Smets et al., 2015] to be 33.1 % and for AM0 with 1.26 eV the limit is 30.1 %.

Not only do the Shockley-Queisser set limitations on the PV cells efficiencies,, but there are also several factors and phenomenons. Photons with lower wavelengths than the bandgap in a semiconductor fails to excite electrons in the conduction band. This leads to only heat absorption, which also leads to energy loss. This also applies to higher wavelength, where the excess energy does not get converted into something useful. *Carrier recombination* will also cause loss in efficiency due to the recombination mechanism, where electrons and holes recombine and are annihilated [Smets et al., 2015].

As mentioned, solar cells are tested under STC and in a controlled environment. In real operation environment the amount of power production would be significant lower. Higher irradiance would cause an increase in temperature and the voltage will decrease and hence output power. Therefore, a so-called *nominal operating cell temperature* (NOCT) is calculated together with STC [Smets et al., 2015]. In addition, a derating factor (f)is included to take into account environmental factors such as soiling, snow, ageing, etc. The PV power output can then be expressed as [Homer Energy, 2020]:

$$P_{PV} = Y_{PV} f_{PV} \frac{G_T}{G_{T,STC}} [1 + \alpha_p (T_C - T_{C,STC})] \tag{2.25}$$

Where Y_{PV} is the cells rated power outpur, G_T is the solar radiation on cell, α_p is the temperature coefficient of power and T_C is the cells temperature. The subscript STC indicate values which were used under testing, 25° and 1 kW/m^2.

2.5.3 Cell Temperature

The temperature of a solar cell will deviate from the STC at 25°. With an increase in temperature, the intrinsic carrier concentration increases due to a lower band gap, hence an increase in carrier recombination rate. Therefore, knowing a temperature coefficient of parameters such as V_{OC}, I_{SC}, P_{mpp} and the efficiency η, the behaviour of the cells with temperature can observed. V_{OC} will decrease by a considerable amount and the I_{SC} will slightly increase. i.e Voltage decreases due to increasing internal resistance and current increases slight due to reduction in the band gap. The PV cells temperature does not completely depend on the ambient temperature, but also the irradiance intensity. A combination of these factors will shift the IV characteristics and are illustrated in figure 2.11 [Masters, 2013].

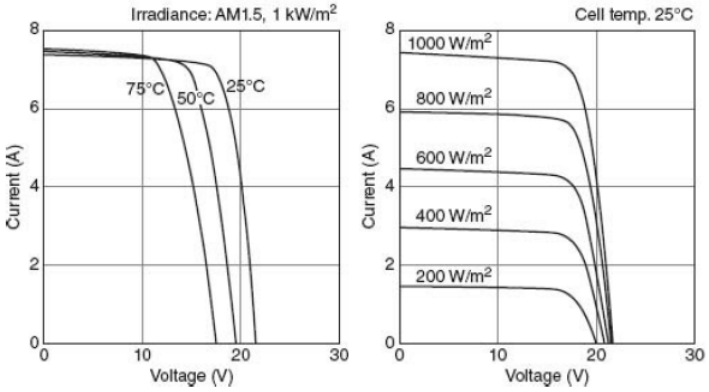

Figure 2.11: IV characteristic curves under various cell temperature and irradiance levels for a Kyocera KC120-1 PV module [Masters, 2013]

2.5.4 PV modules and configuration

The PV *modules* or solar panels is an assembly of photovoltaic cells/ solar cells. These cells are mounted into a framework to encapsel a configuration of series connected cells. The framework is meant to support the cells for mechanical stress, hindering corrosion on electrical contacts and easy installation. They vary in size and the number of cells, typically the modules have 60-128 cells. Since they are connected in a series, the voltage adds. For example, 60 cells with $V_{OC} = 0.7$ V has a module open circuit voltage on 42.0 V [Honsberg and Bowden, 2019].

As several modules are connected into a large system, the configuration of the system is titled *array*. The configuration is optimised for each location to obtain maximum efficiencies from the production. Modules connected in a series will add up voltage and keep current remaining constant. Parallel lined modules modules keep voltage constant, while the current is the sum of each module the current passes through. The array configuration will therefore often have series branches, which is connected parallel to each other. Strings of parallel wired modules is also an optional configuration, but the combined branches is preferred over strings, due to the fact of one string will not compromise production from other strings. By building up voltage in series and current in parallel, the configuration ultimately increase power to a desired specification [Honsberg and Bowden, 2019].

2.5.5 Shading and Bypass Diodes

If a cell/module is shaded from vegetation, dust, or something similar, the performance of power production will be negatively impacted. The shading could also mismatch between solar cells, which could cause a power loss due to different conditions. The diode in the shaded module will become reversed biased and has no flow of current and dissipate power. The reverse bias could potentially cause immense damage if its large enough. To prevent this, a so-called bypass is installed in the framework of the module. These are rapid switching transistors and capacitor which are almost lossless. They are connected in parallel for each cell in the series connection with opposite polarity [Honsberg and Bowden, 2019].

2.6 Wind as a resource

The main driver of global winds on the earth, is the sun. Solar radiation unevenly heats the earth's surface, causing a pressure differences across the globe. Due to variation in absorption of incoming energy, convective cells build up in the lower layer of the atmosphere. The cells gets heavily influenced by the earth's circulation causing motion, where the simplest model uses four atmospheric forces.[Manwell et al., 2010]. The convective cells are illustrated in figure 2.12 with their common name.

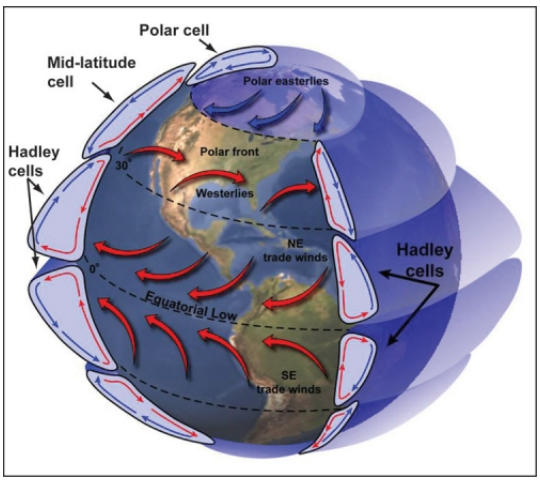

Figure 2.12: Hadley cells, Ferrel (mid-latitude) cells, and Polar cells characterize current atmospheric dynamics. Image obtained at https://groups.seas.harvard.edu/climate/eli/research/equable/hadley.html.

Pressure forces, the Coriolis force (from earth's rotation), internal forces (large-scale circular motion), and frictional forces (earth's surface). The atmospheric pressure field will cause air to move from high to low pressure, causing a pressure gradient vertical (usually cancelled by downward gravitational force) and horizontal. While the forces work on air, at the same time additional forces strive to mix air due to temperature differences and pressure air masses distributed across the earth's surface. The forces mentioned in the wind system will differ depending on the scale of the motion [Manwell et al., 2010].

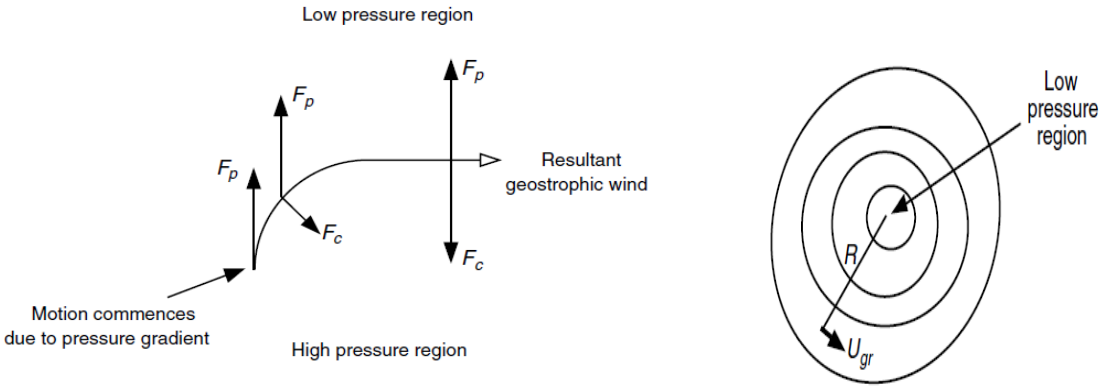

(a) Illustration of the geostrophic wind; F_p, pressure force on the air; F_c, Coriolis force [Manwell et al., 2010].

(b) Illustration of the gradient wind U_{gr}; R, radius of curvature [Manwell et al., 2010].

Figure 2.13: Illustration of the motion of a wind system [Manwell et al., 2010].

2.6.1 Wind Power

By defining a volume or a parcel of wind of mass m, determine the energy will be kinetic energy dependent on mass and speed. The kinetic energy of the parcel is given as [Andrews et al., 2021]:

$$E_k = \frac{1}{2}mv^2 \tag{2.26}$$

Where v is the wind speed. To derive at the power output, energy per time unit needs to be addressed. By finding the mass flow rate $\dot{m}$, the power output can be expressed as [Andrews et al., 2021],

$$P = \frac{dE}{dt} = \frac{1}{2}\dot{m}v^2 \tag{2.27}$$

Where $\dot{m}$ is the mass flow rate, which is given as $\dot{m} = \rho A v$. ρ is the air density and A is the cross-section of the area swept by the turbine blades. Hence [Andrews et al., 2021],

$$P_w = \frac{1}{2}\rho_{air} A v_{air}^3 \tag{2.28}$$

At standard test conditions (STC) the air density is 1.225 kg/m^3 and decrease or increase dependent on temperature. The power has Watt (W) as unit and since a cross section area is swept, the *specific power* output is measured as W/m^2. The power in the wind is therefore heavily relied on wind speed, since its cubed [Jung and Schindler, 2019].

2.6.2 Wind Turbine and Efficiency

Betz Limit

Betz limit is set as the theoretical maximum of what a wind turbine could possibly archive, derived by Albert Betz. As wind travel through the turbine, the wind slows down due to energy transferred to the turbine. The accumulation of the wind behind the turbine cannot lose all its velocity, causing an upstream wind going through a cross-section and then downstream of wind. By having infinent number of blades, air flow is homogenous and incompressible, steady, no friction (drag) and uniform spread on the rotor area the betz limit is set as [Andrews et al., 2021]:

$$\eta_{betz} = \frac{16}{27} = 59.26\% \tag{2.29}$$

Since this is the absolute maximum, the modern turbines archive around 80 % of the limit. On the best operating day, it has a range on 40-50 % converting efficiency into power [Masters, 2013].

Tip Speed

The rotor efficiency a property which often describe the turbines efficiency. Its found by taking the ratio of the turbines tip speed relative to the upstream wind speed. The measure is called Tip-Speed Ratio (TSR) and is calculated as

$$TSR = \frac{Rotor\ Tip\ Speed}{Wind\ Speed} = \frac{2\pi\omega_t r_b}{v_{wind}} \tag{2.30}$$

Here ω_t is the rotational speed of the turbine blades and r_b is the radius of the blades. Considering the parameters in TSR, the rotational speed and wind speed varies. This gives the option to express the TSR as a function to find the most optimal value to ensure the best TSR for maximum efficiency [Andrews et al., 2021].

Logarithmic profile

At any location given, wind speed varies considerably due to local variation. The wind speed will be affected by these variations and likewise the load on the turbines. It's also large fluctuations in the magnitude of the speed over a period of days. Due to frictional forces near the surface, the wind speed increases with height above the ground. The relationship between wind speed and height can be derived in many ways, but a logarithmic profile suits it well, derived from fluid mechanics [Manwell et al., 2010].

The derived equation for the profile does come with simplifications and assumptions. Where the air density is constant at all heights, making the pressure gradient also constant. By assuming a small pressure gradient, an expression on the relationship is given as:

$$\frac{u(z)}{u(z_{ref})} = \frac{\ln(\frac{z}{z_0})}{\ln(\frac{z_{ref}}{z_0})} \tag{2.31}$$

Where z_0 is the roughness length given in table 2.1, z_{ref} is the height where the measurement was taken from and z is the tower height. A plot of this given function is given in figure 2.14

Table 2.1: Typical roughness on common terrain kind, from [Saheb et al., 2014].

Terrain Description	Roughness Lengths z_0 [m]
Very smooth, ice or mud	0.00001
Calm open sea	0.0002
Blown surface	0.0005
Snow surface	0.003
Lawn grass	0.008
Rough pasture	0.01
Fallow field	0.03
Crops	0.05
Few Trees	0.10
Many trees, few buildings	0.25
Forest and woodlands	0.5
Suburbs	1.5
City center, tall Buildings	3.0

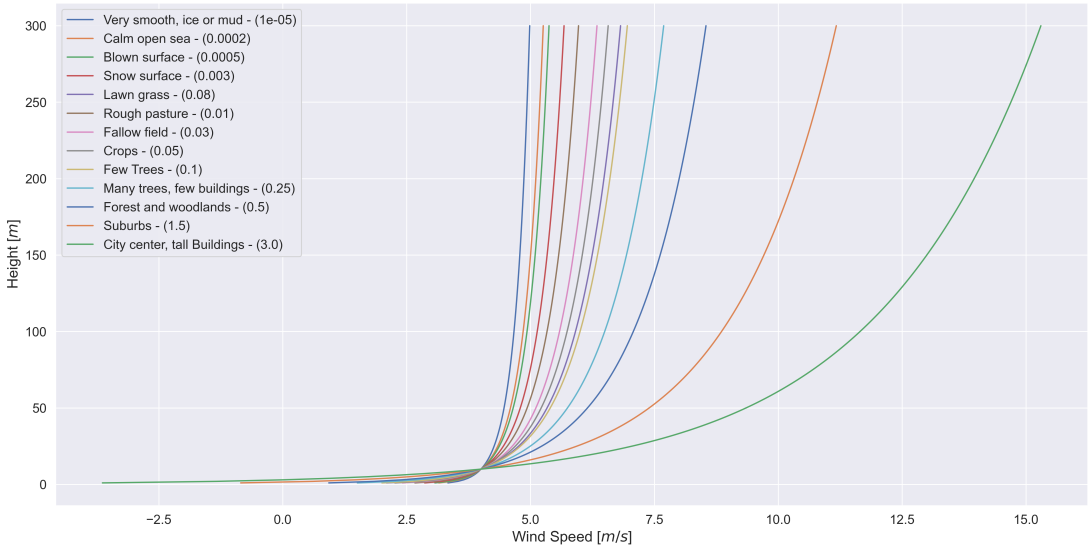

Figure 2.14: The wind speed profile for all the roughness lengths given in table 2.1, where z_{ref} is at 10 m and u_{ref} is at 6 m/s.

2.6.3 Power curve and operating of wind turbine

As mentioned earlier in section 2.6.1, the power of the wind is proportional to wind speed, i.e $v^3 \propto P$. Therefore, it's important to control and regulate the wind turbine according to the wind speed. The characteristics of a wind turbine power output relative to the wind speed is summarised in a power curve. In figure 2.15 a power curve is presented.

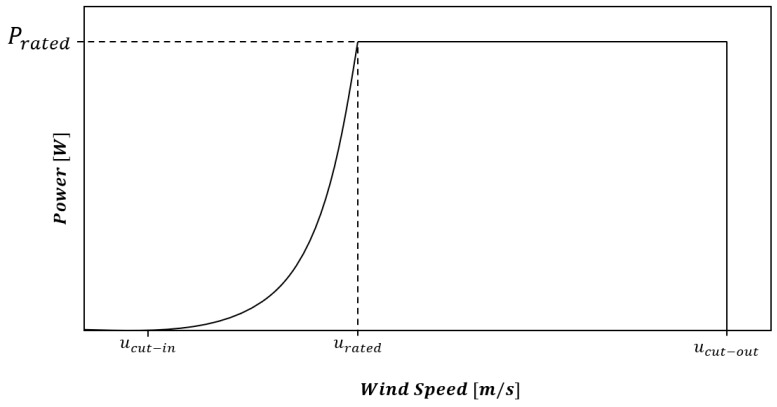

Figure 2.15: The ideal power curve for a wind turbine, inspired by [Andrews et al., 2021].

There are a few important parameters in a power curve, as seen in figure 2.15. These are essential for operating the turbines pitch of the blades and optimizing the power coefficient C_p, which is $C_p = P_0/P_w$ where P_0 is the maximum extraction to Betz limit and P_w is the power output from the turbine. Defining the parameter as [Andrews et al., 2021]:

- u_{cut-in} - The cut-in wind speed is the required speed to start power production. Lower wind speeds have to low energy to rotate the blades creating zero output.

- $u_{cut-out}$ - The cut-out wind speed is the highest tolerated wind speed for the wind turbine mechanical stress. The pitch control of the blades can be altered to shed power by reducing the angle of attack. This is why the power output stays the same during higher wind speeds until its reaches its maximum. When the operating control pitch the blades parallel with angle of attack, the production reaches zero and the maximum tolerated wind speed is reached.

- u_{rated} - The rated wind speed is the speed required to produce the maximum power output from the turbine. As seen in figure 2.15, higher wind speed than the rated will not produce any excess power. In these high wind conditions, controlling the operating blades is essential to not enhance stress but remain maximum output.

To change the power curve, there are mainly two measures to address. The swept area of the wind turbine will change the rated speed of the turbine and generate more power assuming two identical turbines with different blade radius. A larger swept area will reduce the rated speed but give a higher power output at any given wins speed. The second measure is changing the rated capacity of the generator, increasing the generator rating causing the rated wind speed to increase [Masters, 2013].

2.6.4 Design and Control

The wind turbines are categorised after which axis of operation, Horizontal Axis Wind Turbine (HAWT) or Vertical Axis Wind Turbine (VAWT). For large scale turbines, HAWT has been favoured due to being more efficient at larger scales. There are mainly to ways to extract power from the wind, *downwind turbines*, or *upwind turbines*. In downwind the wind will control the yaw operation of the turbine. It is however exposed to wind shadow effects which will comprise an even production. In Upwind the blades are facing the wind, meaning that no wind shadow effect is compromising the production. The yaw control must be optimised to ensure the highest performance [Andrews et al., 2021].

To generate rotational energy from the thrust at the turbine is done by shaping the turbine blades as aerofoils. The blades utilize Bernoulli's principle to generate lift which causes rotational motion on the rotor. It states if an object flow rate increases the pressure will decrease. The streamline of air moving along the topside of the airfoil will have a greater speed than underneath. This results in a higher pressure under the airfoil, which again results to a force pushing the airfoil

upwards, also known as lift. Since the lift is generated normal to the wind, and the blades faces normal to the wind, the blades will move in a rotating motion in y-axis if wind attack at x-axis. To obtain the preferred rotational speed, the angle of attack across the blades can be changed when blades are twisted [Masters, 2013].

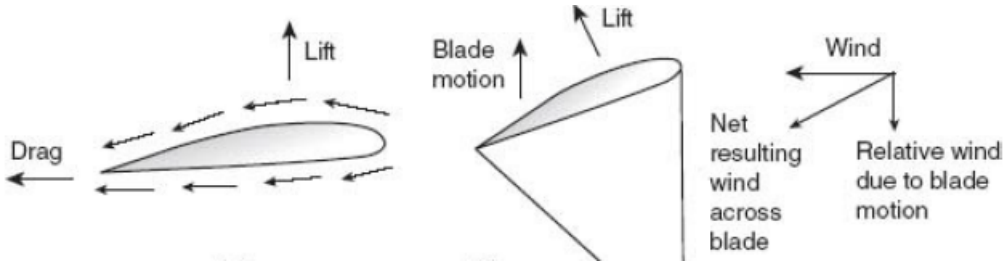

Figure 2.16: A airfoil where high velocity wind slides over the top of foil and generates lift (left). The actual wind and relative wind due to rotating motion from the blades, resulting in a generated lift (center). The working directions illustrated (right) [Masters, 2013].

To optimise the utilisation of extraction of energy from wind, two main approaches is used to control a wind turbine which is divided in *passive* and *active control*. Passive control optimises the design of the blades to improve energy conversion from the wind. If the angle of attack is increased, so does lift, and drag until to some extent, this is entitled stall/stalling. The active control is a mechanical system which could alter angle of attack of the blade. When increasing the angle of attack, induces stall and reduces efficiency due to lower wind speeds. This is called *Active Stall Control*. When angle of attack is reduced, lift is reduced, and the turbines output is reduced. This is called *Pitch Control* [Masters, 2013].

2.7 Energy Storage System

With increasing demand of energy and heavier loads on the power grid, Energy Storage System (ESS) facilitates high penetration on the grid with variable renewable energy. The integration of renewable energy increases the demand for distributed energy system sources. ESS plays a large and important role in making the operating capabilities reliable and stable, especially the non-dispatchable energy sources. The technology is already introduced to the power grid and has been available for years [Gao, 2015]. These recent ten years, connecting batteries to the distribution grid has increased, where different types of batteries are used. ESS has unique low and high energy management applications, where frequency control, voltage support, load shaving/leveling, etc. These applications improve the quality of the delivered power and enhance stability, i.e to sustain an optimal economy for the system [Birkeland et al., 2020].

2.7.1 Efficiency

The efficiency of an energy storage system is defined as the round trip efficiency (η_{rt}), i.e the efficiency of a full cycle of charging and discharging of a medium.

$$\eta_{rt} = \eta_c \cdot \eta_d \tag{2.32}$$

Long transmission lines to remote areas often are subjects to constraint on the delivered power, which cause problems for high demanding peaks in the load. This compromises the grid operations and are able to solve using ESS, more specific Battery Energy Storage System (BESS). Using BESS to peak shave loads, shift loads, or other strategies will strengthen the grid operation performance [Gao, 2015]. However, the large investments, regulations and the market structure delay the utilization of energy storage. The storage unit are yet not competitive enough for the energy market for majorities of countries, but R&D has caused a massive cost reduction and will likely continue [Robson and Bonomi, 2018].

The types of ESS can be divided into four categories, mechanical, electrochemical, electrical and thermal. All types hold their own characteristics, where the form of source of utilization is key for the choice of ESS technology. The most common technologies are listed underneath [Gao, 2015]:

- **Flywheel (Mechanical)** - The flywheel is a disk with a certain mass and spins at high velocity to store kinetic energy. Connecting the flywheel to an electrical machine, it can support immediate active power due to its high power density.
- **Pumped Hydro (Mechanical)** - Water reservoirs at a higher altitude has excess water elevated using electrical pumps, creating a pumped storage. The height difference between reservoirs access utilization of potential energy. Releasing the upper reservoir to a lower level through a type of turbine, generates electricity. The limitation of production is to inflow of water. The advantages of this system are high flexibility and high storage capacity.
- **Supercapacitors (Electrical)** - Is developed from electric double-layer theory. A two-layer capacitor are created when the electrode contacts the electrolyte. The supercapacitor consists of numerous capacitors arranged in parallels or series, depending on the required voltage. The arrangement is a so-called cell, which is also stacked in series. These are seperated using an electrical insulator that prevents physical contact of the electrodes but allows ion transfer. They are packed and sunk into an electrolytic solution forming a double

layer charge distribution. It has high power density, and the storage are usually 20-1000 times of a common capacitor.

- **Electrochemical Storage** - Taking advantage of the electrochemical process, batteries have increased in popularity. Batteries store energy through this process in various chemical configurations. Due to different configurations, the batteries have different properties. The batteries have a large role in improving operation capabilities due to its almost instantaneously respond. A list of the more common battery configurations is listed underneath.

  - **Lithium-Ion Batteries** - Lithium-ion battery resembles a capacitor due to its operating behaviour and consists of three layers. First is the anode and is made from lithium compound. Second layer is the cathode, made from graphite. The third layer is an insulator and are placed between the first and second layer. It has a life cycle on $<$ 10 000 times [% DoD], an efficiency on 80-97 % and an energy density on 75-200 $[Wh/kg]$.
  - **Lead-Acid Batteries** - Has existed over 100 years and is mostly used in rechargeable batteries, due to its low cost, high efficiency, and good surge capability. The lead-acid battery cells are connected in series and immersed in 20-40 % solution of sulfuric acid which act as an electrolyte. It has a life cycle on around 2000 times [% DoD], an efficiency on 70-80 % and an energy density on 30-50 $[Wh/kg]$.
  - **Sodium-Sulfur Battery** - To utilize the sodium, a high operating temperature needs to be achieved 350 (C°) due to liquefy sodium. The reason is to get the sodium to act as an anode and the molten sulfure to act as a cathode with a membrane in between. The difficulty with using this configuration is to have a cooling system, and liquid sodium is dangerous in contact with water in the atmosphere. It has a life cycle on around 2500-6000 times [% DoD], an efficiency on 75 to $<$ 90 % and an energy density on 100-250 $[Wh/kg]$.

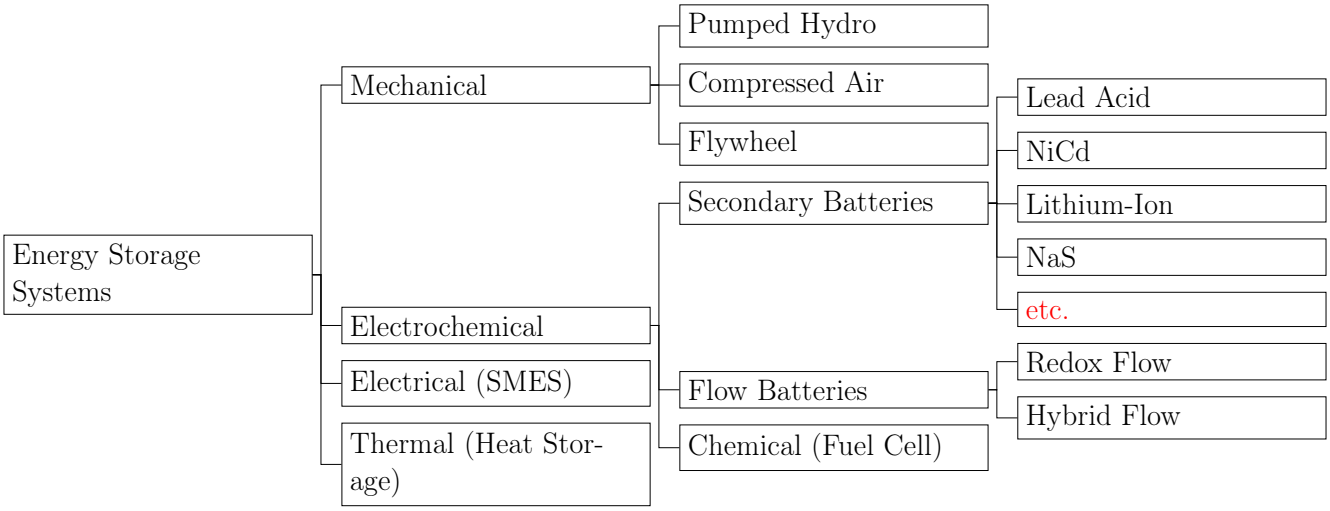

Figure 2.17: A diagram showing classification of ESS, where some has been explained in this thesis. Inspired by [Gao, 2015].

2.7.2 Important Parameters for Battery

MIT has made a guide to understand battery specifications, which makes it easier to understand the key parameters. There are several parameters for a battery, but the most relevant to this thesis will be described [MIT, 2008].

- **Depth of Discharge (DOD) [%]** - The definition of an amount of capacity used in a discharge, where a complete discharge will be a 100 %. DoD on 80 % is defined as a deep discharge.
- **State of charge (SoC) [%]** - The current capacity relative to the maximum capacity.
- **Energy Density [Wh/kg]** - The amount of stored energy per kilo.
- **Nominal Energy [Wh]** - Describes the amount of energy capacity, the total Watt-hours available.

3 / Case Study: Northern Senja

According to Norwegian mapping authority (Kartverket), Senja is the second largest island in Norway with an area of 1589.35 m^2. The island is located about 69° N along the coast in Troms and Finnmark, Norway. Senja is known for its mountainous terrain and excellent seafood. The coastal communities contribute for the Senja municipality to have the highest economic growth in fishery industry in 2019 [Sjømaklyngen Senja, 2021].

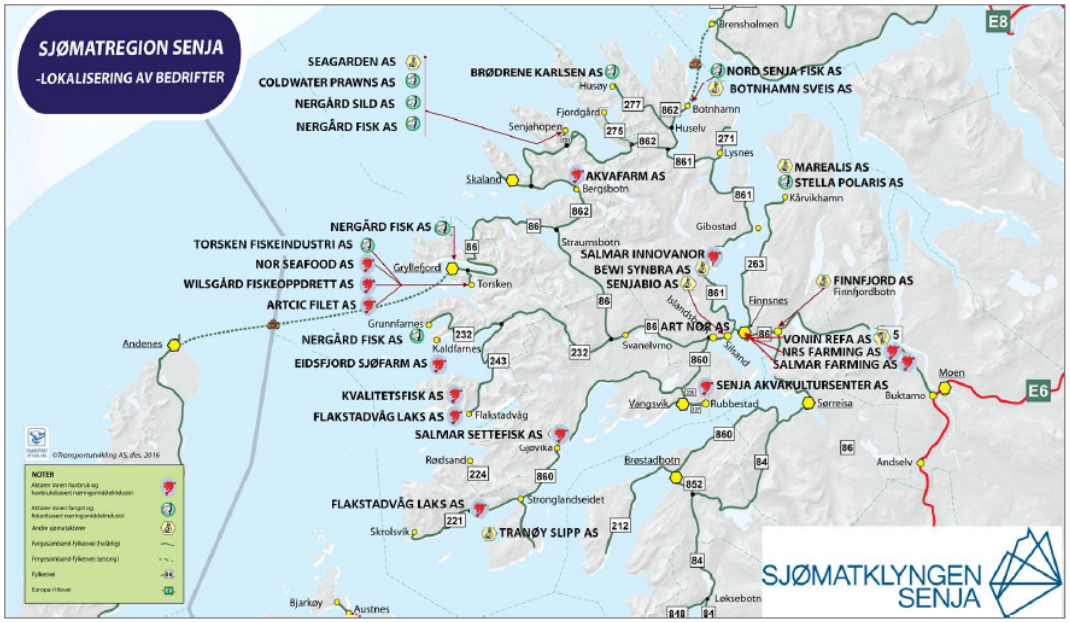

Figure 3.1: Map of the fishery industry at Senja, from [Sjømaklyngen Senja, 2021].

3.1 Overview

As mentioned earlier, an area which the alternative solution is being investigated is the northern part of Senja, more specific Husøy and Senjahopen. The main goal is to use the already existing power grid to sustain top modern machinery in the fishery industry. Due to higher loads on the grid which is almost at its fullest capacity, motivates the industry and energy companies to find an alternative solution [Smart Senja, 2021], [TKN, 2020b]. The long radial distances and mountainous terrain creates a vulnerable infrastructure which steady increases its power demand. This thesis is performed as a case study with an aim to inject high penetrating renewable energy

resources into the network to supply voltage support. Arva granted access to its power quality measurements, power failure/flicker log and load data. In addition to the data, information about the newly installed batteries at Husøy is used in this thesis. *The Arctic University of Norway* (UiT) collaborates with Arva on the project, access to the installed pyranometer and PV production data.

3.2 Distribution Grid

The network towards Senja is supplied with a 66 kV from the regional grid. From the transformation station, the power is supplied through 22 kV radial transmission lines to northern Senja. There are a total of three substations at Senja to step down voltage to local distribution. The substations are located at Silsand, Svanelvmoen and Bergsbotn, which is shown in figure 3.2 as red squares.

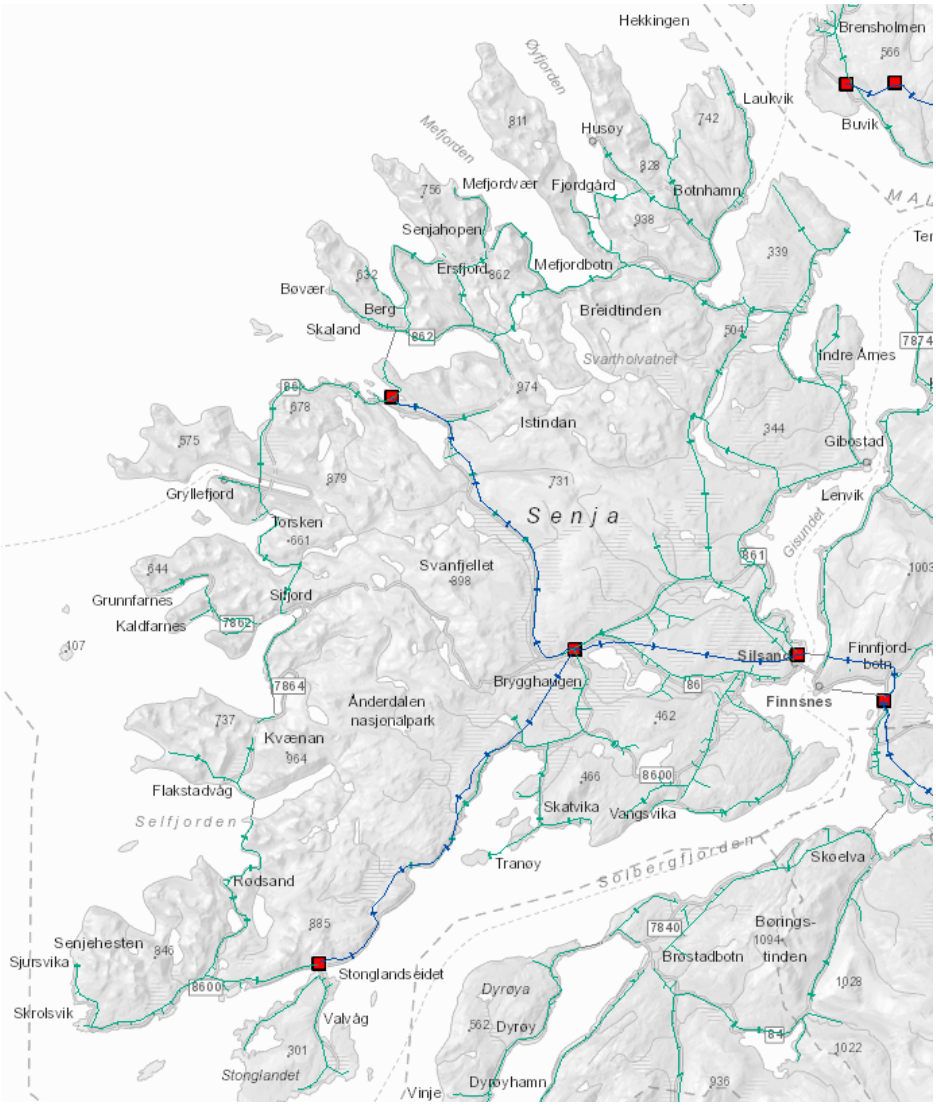

Figure 3.2: The topology of the distribution network and the hydroelectric power plants at Senja, including their reservoirs [NVE, 2021].

The power failure/flicker data shows periods with stability and instability. Primarily the instability occurs during high season of fishery, which creates high load periods. A visualisation on these measurements is given in figure 3.3.

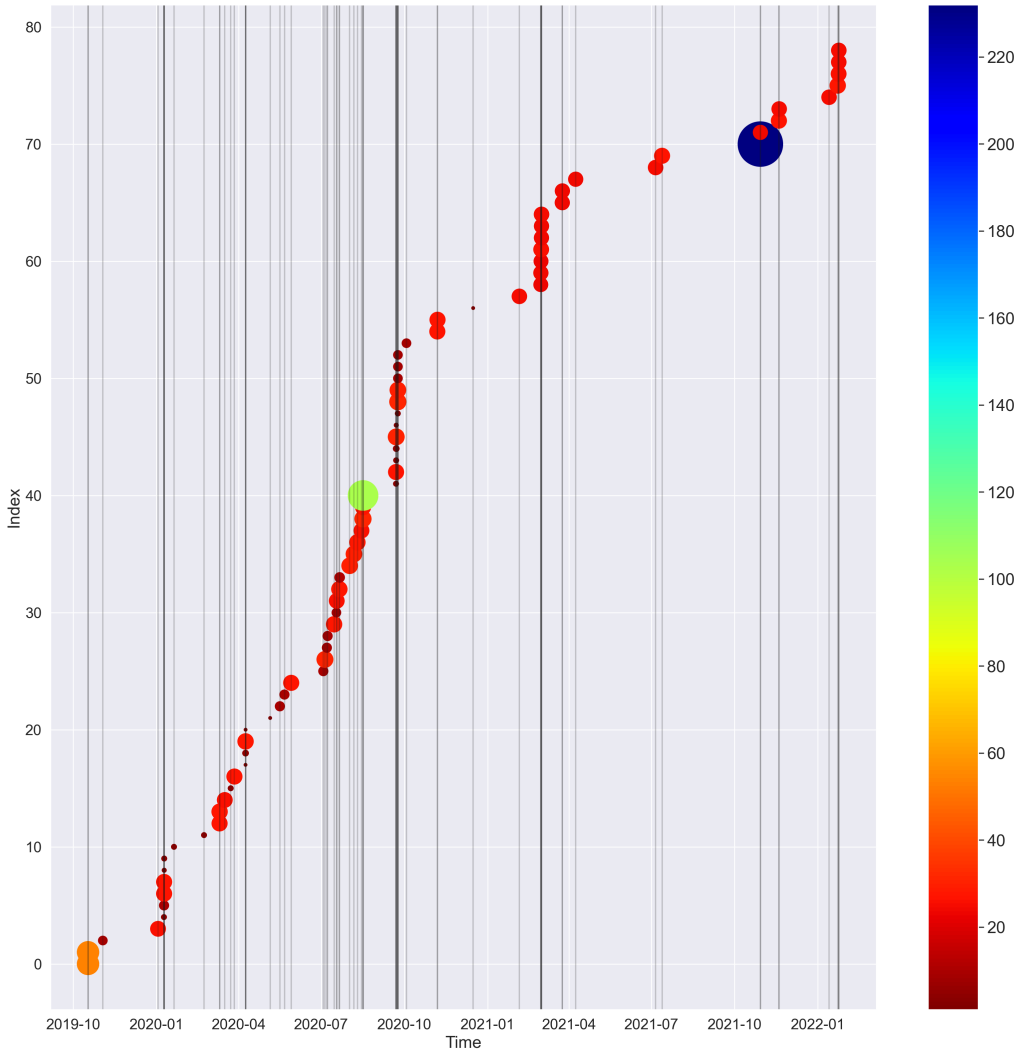

Figure 3.3: The power failures for whole Husøy in 2019/10 to 2022/01, where the points size and colour are the duration of the failures in seconds. The black horizontal lines are the timestamp of occurrences of failure.

Troms kraft has already applied for a concession to build 51 km of transmission lines, to connect Brensholmen and Silsand at a voltage level of 132 kV. It's also in addition applied to build a substation of 22/132 kV on 25 MVA at Kjosen. This is to keep up with new planned industrial establishments and increased network stability [TKN, 2020a].

3.3 Hydroelectric Power Plant at Senja

Senja has three hydro power plants, where two is located at the northern part of Senja, Bergsbotn and Lysbotn. The smallest power plant is located further southwest, which is shown in figure 3.4. These power plants are controlled using an economical dispatch strategy, meaning they produce power when highest profit is possible. The hydro power plants scale is categorised as small/medium, where the installed power is [TKN, 2021]:

	Bergsbotn	Lysbotn	Osteren
Installed Power [MW]	7.9	5.4	2.4
Reservoir Capacity [GWh]	21.59	21.59	1.73
Head [m]	354	106	137
Yearly Production 2021 [GWh]	31.10	35.01	14.64

The Lines from the hydroelectric power plant is approximated using measurement tools in ArcGIS. The three hydro power plants are assumed to be fully operative throughout the year.

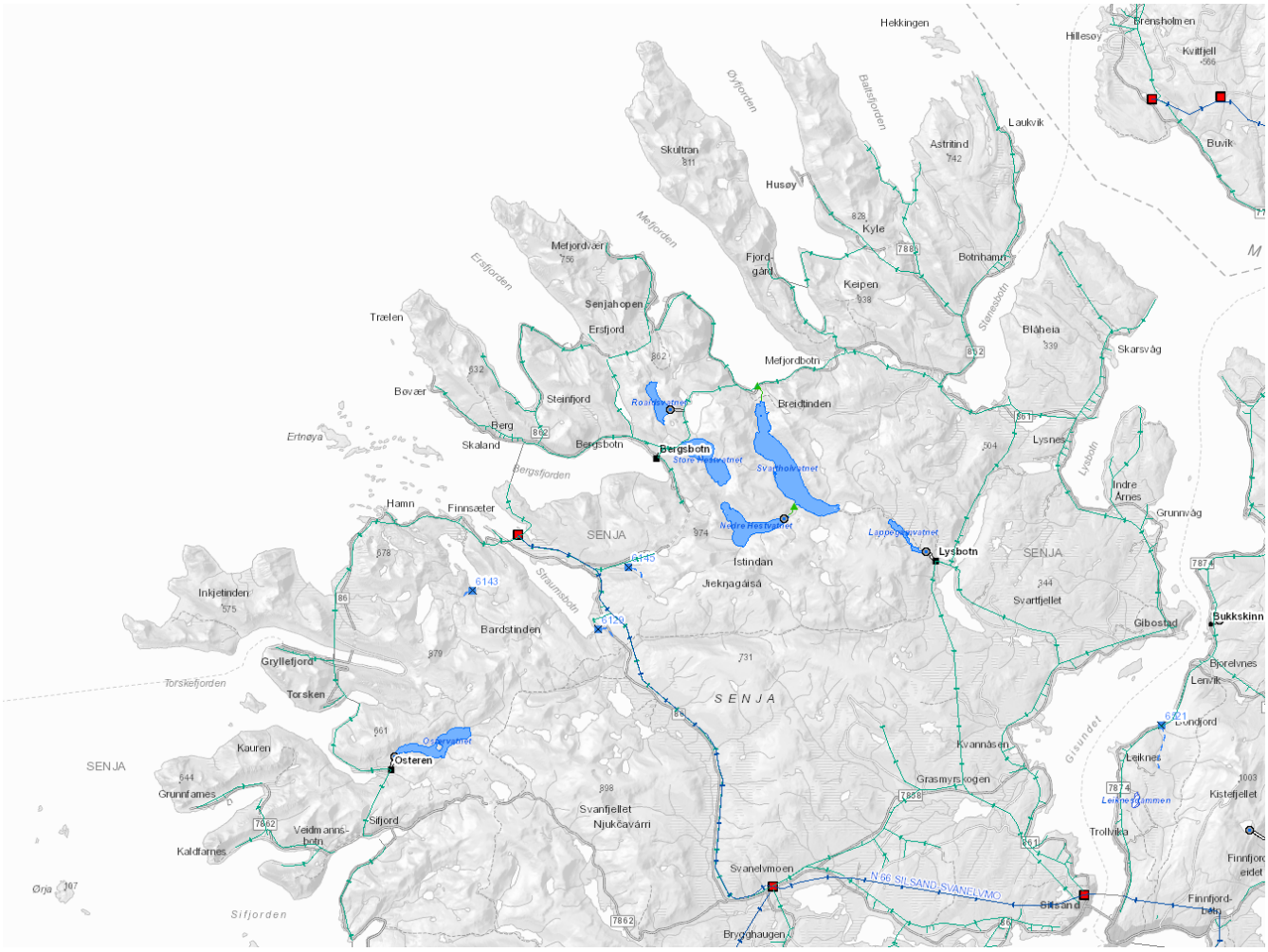

Figure 3.4: The topology of the distribution networks at Senja. The blue line is the 66 kV, cyan lines are 22 kV and red squares are substations [NVE, 2021].

3.4 Examination from Arva

In an examination from Arva in 2019 with a cooperation with *Sjømatklyngen Senja*, they estimate a growth of the peak load from 45 MW (2020) to almost 70 MW (2030). It's also a remark on the estimate made in 2015, it was considered passive, and the most uncertainties lies within new developing industrial projects [Troms Kraft, 2019].

One of the main challenges they are facing today is the voltage drop on the distribution grid towards Husøy. By setting a limit on the variations on the mean voltage to ± 4 %. The challenge for Husøy is to keep the voltage between the limits when introduced to a new load. This problem is shown in the figure 3.5 [Troms Kraft, 2019].

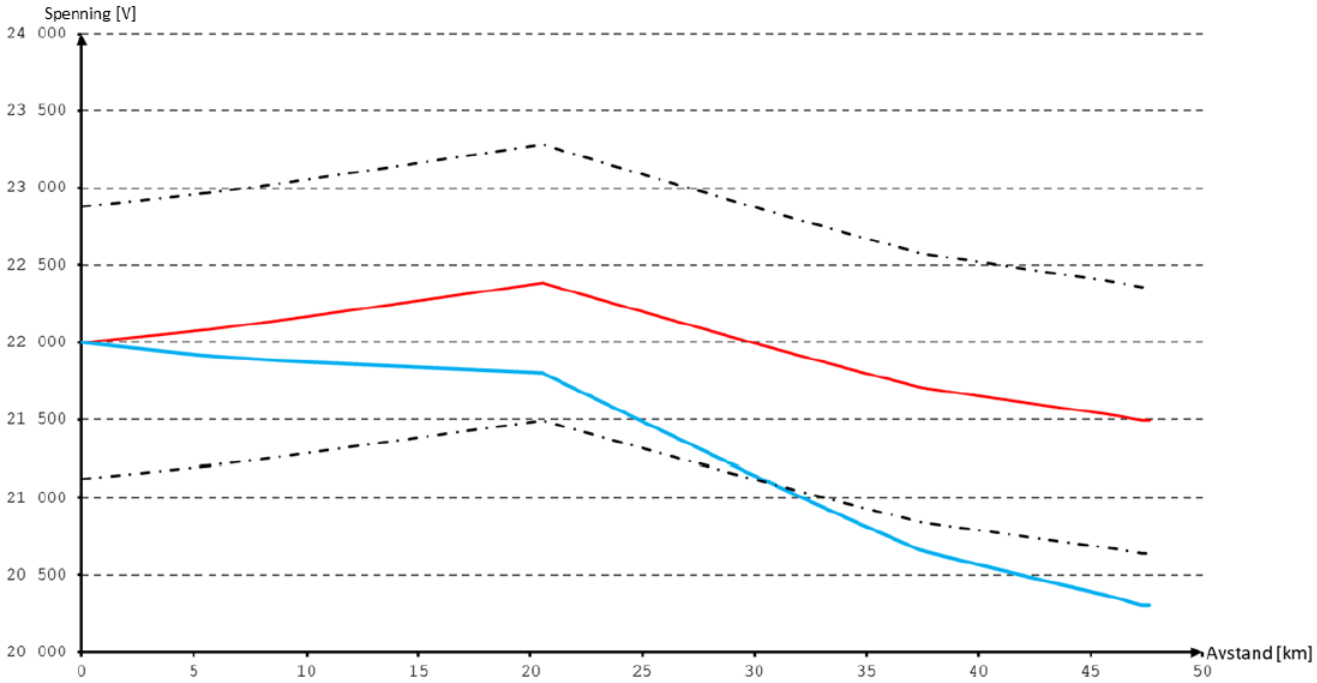

Figure 3.5: An example on voltage variation on the radial distribution network. The red line represents the yearly mean voltage and the blue line shows the scenario with a new loads. The sharp breaking point on the graphs represent Lysbotn hydro power plant [Troms Kraft, 2019].

To solve the low voltage supply problem, some conventional methods is proposed by Arva including the option of alternative methods. The proposed conventional way is to enhance the electrical network by increasing the regional network voltage from 66 kV to 132 kV, to give an overall improvement for whole Senja. Since the concession is already applied for connection between Brensholmen and Silsand with partly submarine cable. The optional option is to reinforce the 22 kV distribution network toward the heavy load points, but this will limit transfer capacity and will most likely not meet the need of increased power consumption. This is an expensive method and will presumably increase the grid rental cost drastically. Therefore, alternative solutions are explored to lower investment costs [Troms Kraft, 2019].

Since the upgrade of the distribution network will take time and inflict with planned industrial establishments, batteries have been purchased to compensate for instability and to acquire knowledge of batteries as power support. An example on how the batteries will compensate is estimated in [Troms Kraft, 2019] and shown in figure 3.6.

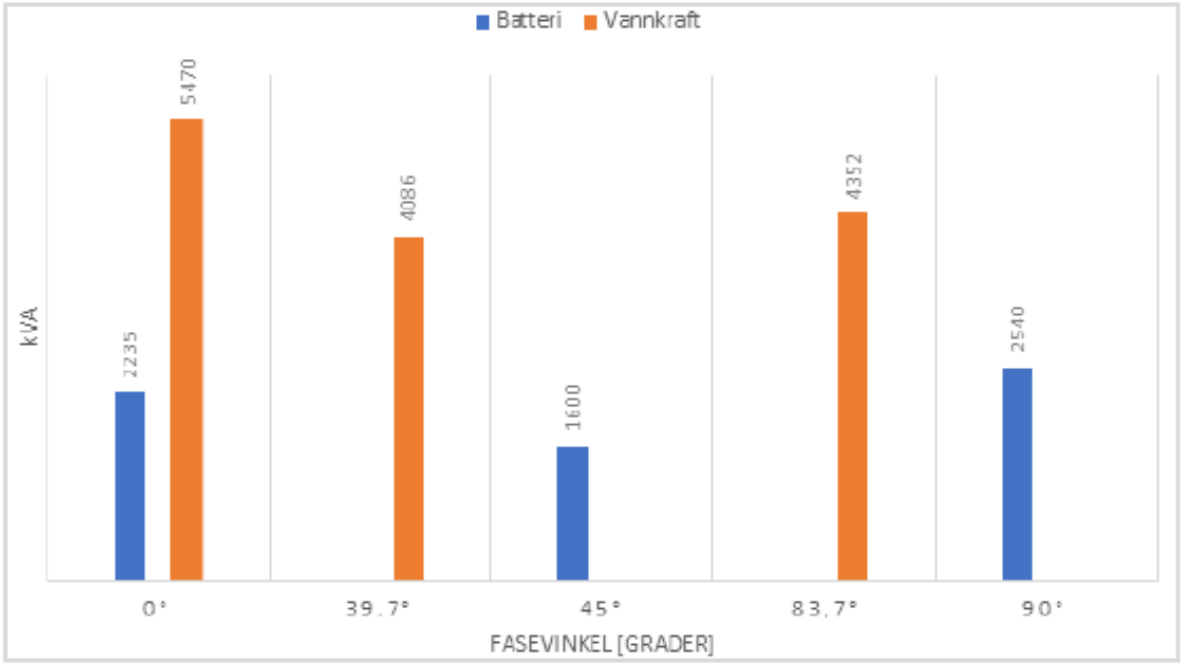

Figure 3.6: Blue is the battery compensation and orange is from Lysbotn hydro plant. x-axis is phase angel and y-axis are apparent power [Troms Kraft, 2019].

4 / Method and Data Collection

4.1 Statistical Methods

To validate the model's performance on real world observations, some parameters and statistical scores will indicate on how well the models forecasts the weather. The basic statistical parameters are used as a sample vector, i.e $\boldsymbol{x} = [x_1, x_2, ..., x_N]$ where N is the total number of indices in the vector. In our formulation of the statistical equations, x_i is the element value where i is the subscript of the element in the vector. The sample mean ($\bar{x}$) can be expressed as.

$$\bar{x} = \frac{1}{N}\sum_{i=1}^{N} x_i \tag{4.1}$$

Using the sample mean, the sample standard deviation (σ) is given as the square root of the sample variance (σ^2) [Freund and Wilson, 2003]. This can be expressed as:

$$\sigma = \sqrt{\sigma^2} = \left(\frac{1}{N}\sum_{i=1}^{N}(x_i - \bar{x})\right)^{\frac{1}{2}} \tag{4.2}$$

Using statistical scores gives an indication on the predicted values from different models with observations from local weather stations. Finding the relationship between predicted and actual values could be done in several ways, but in this thesis the mean bias error (MBE) and the absolute mean error (MAE) will be calculated. The predicted values from the models and observed values is represented as two vectors, $\boldsymbol{X} = [X_1, X_2, ..., X_N]$ for predicted values and $\boldsymbol{Y} = [Y_1, Y_2, ..., Y_N]$ for observed values. The mean bias exploits the average bias which gives an indication on whether the prediction over-or underestimates corresponding to observation. The mean bias can be expressed as:

$$MBE = \frac{1}{N}\sum_{i=1}^{N}(X_i - Y_i) \tag{4.3}$$

If the computation of the bias results in a positive value, hence an indication of overestimation is done by the model compared to the observation on average. Therefore a negative bias value would give an underestimation by the model. To compensate for large errors, additionally MAE

is calculated due to findings where MAE is a more natural measure rather than root mean square error (RMSE) which is unambiguous for large negative compensate for large positive errors giving a small bias. The MAE can be expressed as [Willmott and Matsuura, 2005]:

$$MAE = \frac{1}{N}\sum_{i=1}^{N}|X_i - Y_i| \tag{4.4}$$

In addition to MAE, to quantify the number of large errors between the two vectors RMSE is computed. Even though MAE gives a more natural measure, RMSE gives an estimate on the number of large errors. RMSE can be expressed as [Willmott and Matsuura, 2005]:

$$RMSE = \sqrt{\frac{1}{N}\sum_{i=1}^{N}(X_i - Y_i)^2} \tag{4.5}$$

Including looking at the errors between the two datasets, a correlation measurement is computed. This is done by finding the correlation coefficient, which stipulate the linear relationship between datasets. The coefficient ranges from $-1 \leq \rho \geq 1$, and the correlation is determined by the regression slope. A coefficient value on 1 implies an absolute perfect correlation between X and Y where all points lie on the slope, and vica versa where -1 implies an absolute negative correlation. If the value is zero, there is no correlation at all. In figure 4.1 the different correlations are illustrated.

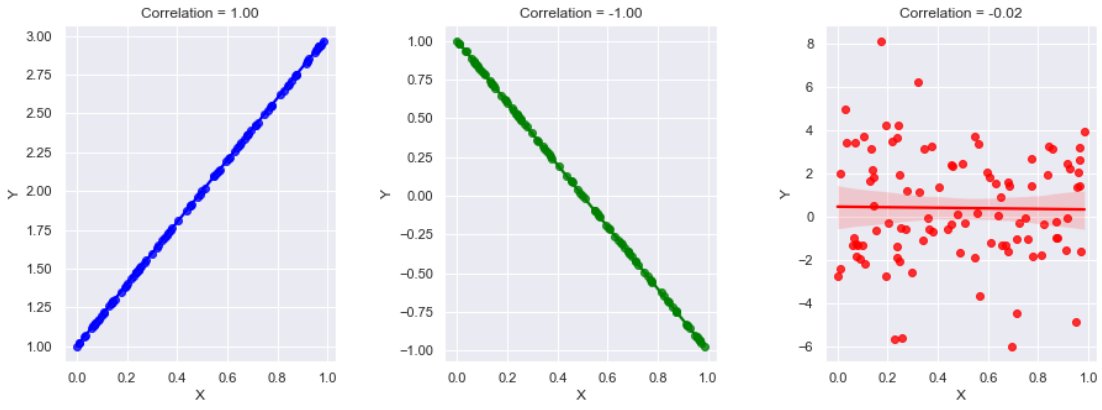

Figure 4.1: Scatter plots with datasets X and Y in three different scenarios, where correlation is displayed as the regression slope and coefficient.

The correlation coefficient has different approaches, but in this thesis, Pearsons equation is used. It can be expressed as [Asuero et al., 2006]:

$$r = \frac{\sum_{i=1}^{N}\left(X_i - \bar{X}\right)\left(Y_i - \bar{Y}\right)}{\sqrt{\sum_{i=1}^{N}\left(X_i - \bar{X}\right)^2}\sqrt{\sum_{i=1}^{N}\left(X_i - \bar{X}\right)^2}} \tag{4.6}$$

Table 4.1: The definition on the correlation coefficient

Correlation coefficient (r)	Direction and Strength of Correlation
-1	Perfect negative
-0.8	Strongly negative
-0.5	Moderately negative
-0.2	Weakly negative
0	No association
0.2	Weakly positive
0.5	Moderately positive
0.8	Strongly positive
1	Perfectly positive

4.2 Data collection

The data is collected from different sources described in this section, both modelled data and observation measurements. The electrical data is provided by *Arva*, and the weather data time frame is correlated to the electrical data. The most common time frame is in year 2020, but PV production at Husøy was installed in late 2020. Therefore, the data is only used for validation. The power quality measurement is at *Brødrene Karlsen* at Husøy, where voltages on 230 V and 400 V is measured, including the load at different points.

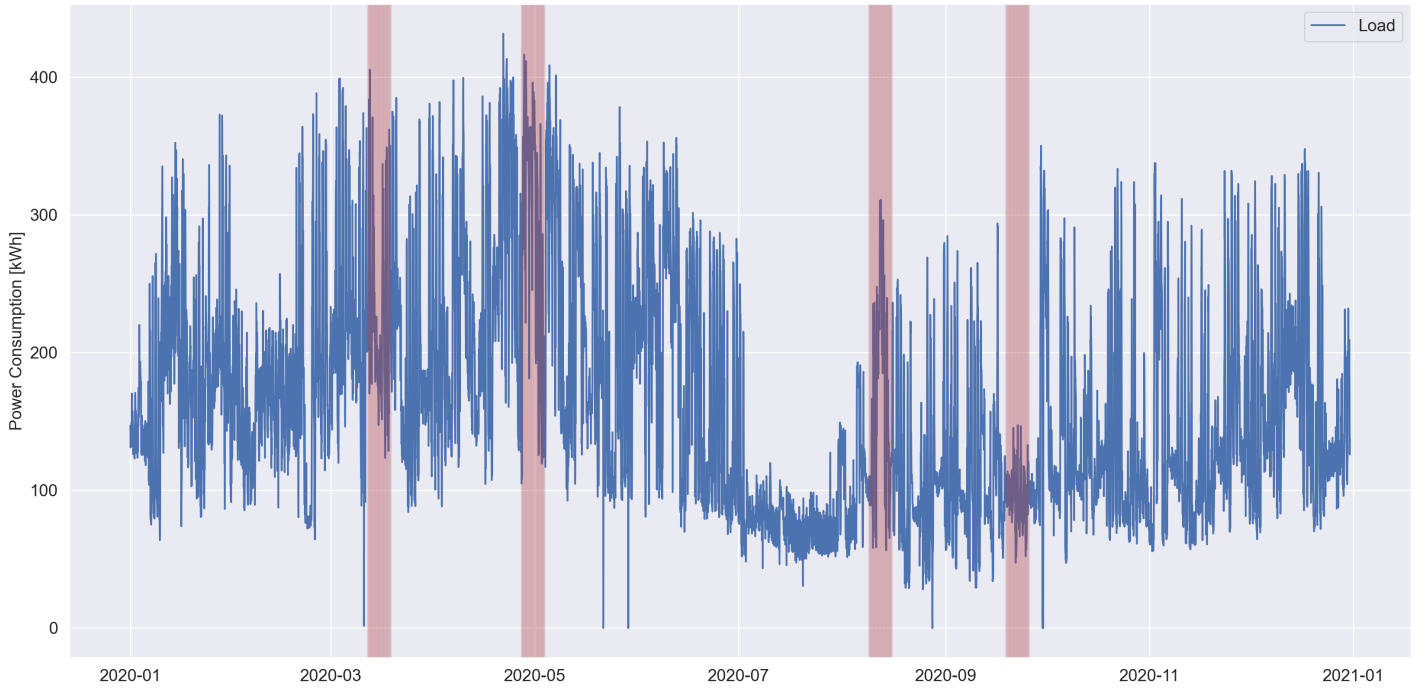

Figure 4.2: One of 5 loads used in power flow analysis. The voltage level at this load is 400 V.The red area show the periods where network simulation was done.

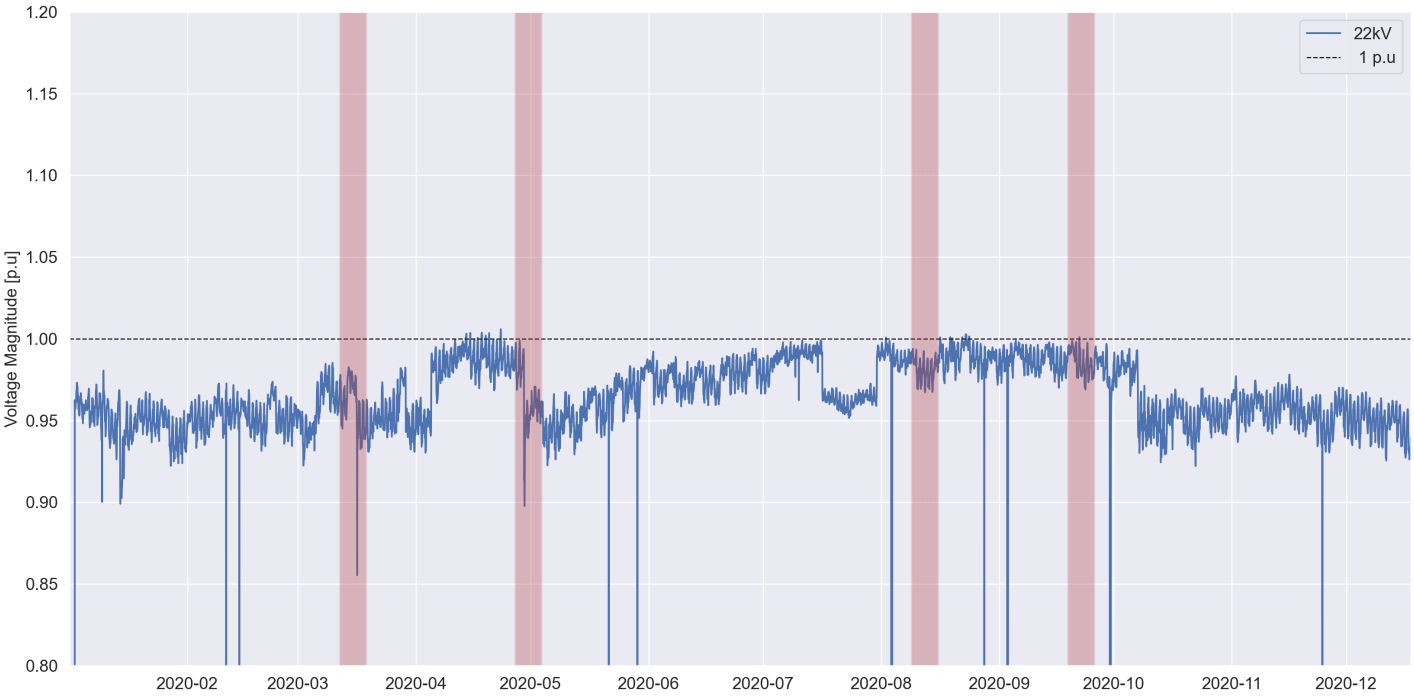

Figure 4.3: The voltage measurements of the 22 kV network at Husøy, given in per. unit [p.u]. The red area shows the periods where network simulation was done.

4.3 Models

4.3.1 ERA5 model

The European Center for Medium-Range Weather Forecasts (ECMWF) has created a fifth-generation model of an reanalysis of the global climate. The ERA5 data covers measurements and calculations since 1950 where datasets from 1950-1978 is split into Climate Data Store. In this thesis, the available data from 1979 and onwards is used. The reanalysis or high-resolution realisation (HRES) model combines global data with observations, completing datasets accordant to the laws of physics [Hersbach et al., 2018]. By using data assimilation, based on numerical weather prediction methods, where every 12 hours at ECMWF a previous forecast is merged optimal with newly observation to best estimate the state of the atmosphere. This is the analysed forecast, but the reanalysed data is spanning over a longer time period which makes better collections on observations. Using HRES gives a high quality of the reanalysed product. But the option to use ensemble or EDA product is available, which has less resolution and by-products (random uncertainty) but consist of short forecasts (18 hours) twice a day [Hersbach et al., 2018].

ERA5 contains a large number of hourly estimates on atmospheric, ocean-wave and land-surface quantities. ERA5 is updated daily with a latency on 5 days, and in case of serious errors, the error will be updated before final release (2-3 months later). ERA5 produces a 4D-Var data assimilation and model forecast according to an ECMWF Integrated Forecast System (IFS). Atmospheric data are interpolated to 37 pressure, 16 potential temperature and 1 potential vorticity level(s) by FULL-POS in the IFS [Hersbach et al., 2018]. Collecting from surface or single level, the data contains 2D-parameters such as precipitation, top of atmosphere radiation and so on. The atmospheric model is coupled up to the land-surface model (HTESSEL), which has parameters closer to the surface such as 2 m temperature [Hersbach et al., 2018].

ERA5's datasets are produced with a regular longitude-latitude grid, covering the whole globe with an horizontal resolution on $0.25° \times 0.25°$ (atmosphere) and $0.5° \times 0.5°$ (ocean waves) for the reanalysis data. The data is downloaded using CDS API to request the datasets using a python script, which can be auto generated at their website. The data format is chosen to be NetCDF, reasoning for this format is because of the convenient interactions between Python libraries. Example on extracted data is shown on the next page.

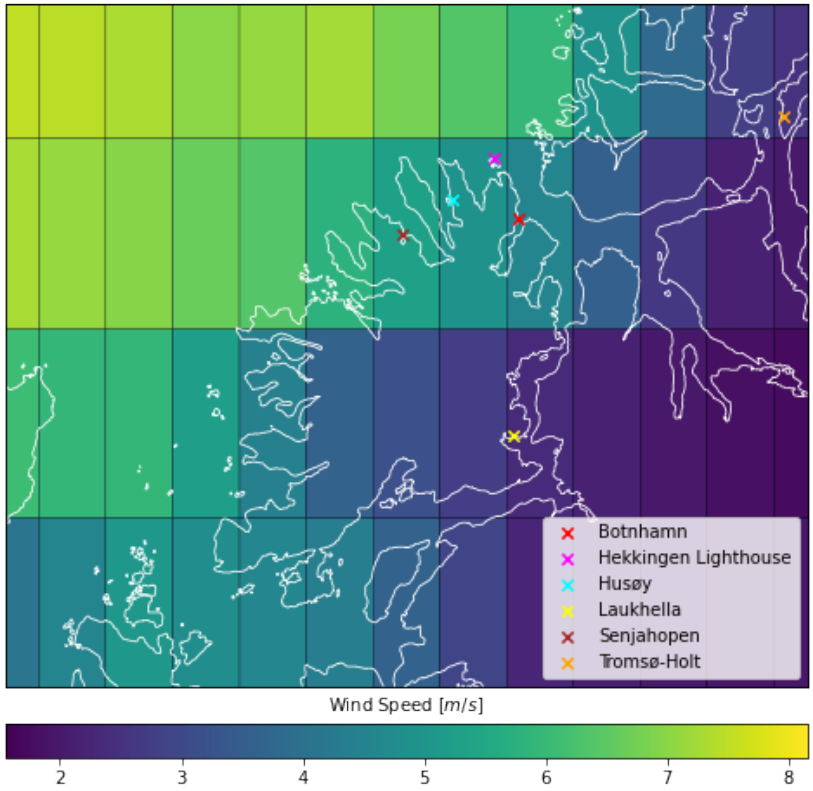

Figure 4.4: The average wind speed in 2020 with ERA5 data plotted in each grid section.Coordinates for the points is given in table 4.2.

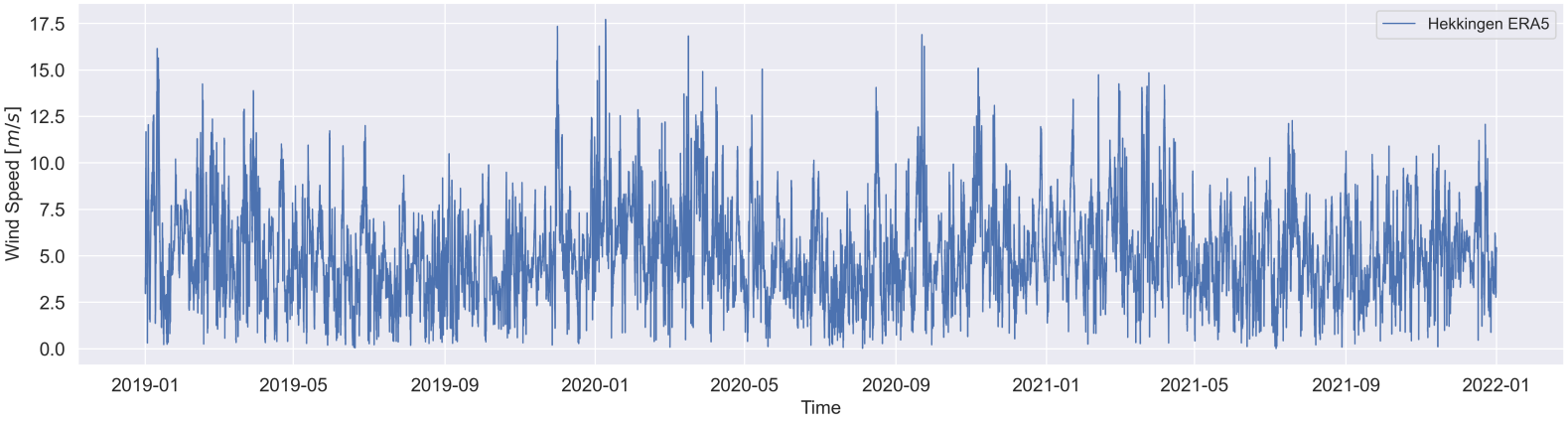

Figure 4.5: The wind speed extracted from the ERA5 model at the grid cell containing Hekkingen lighthouse.

4.3.2 AROME-Arctic Model

The Norwegian Meteorological Institute (MET) is providing forecasts of the weather since 2015 by using the model Applications of Research to Operations at Mesoscale (AROME) for the arctic region, which is called "AROME-Arctic". This model gives an accurate prediction and consist of historical data over a large area of sea, in addition to Svalbard. The development of AROME-Arctic is a collaboration with several nations, international projects and institutions.

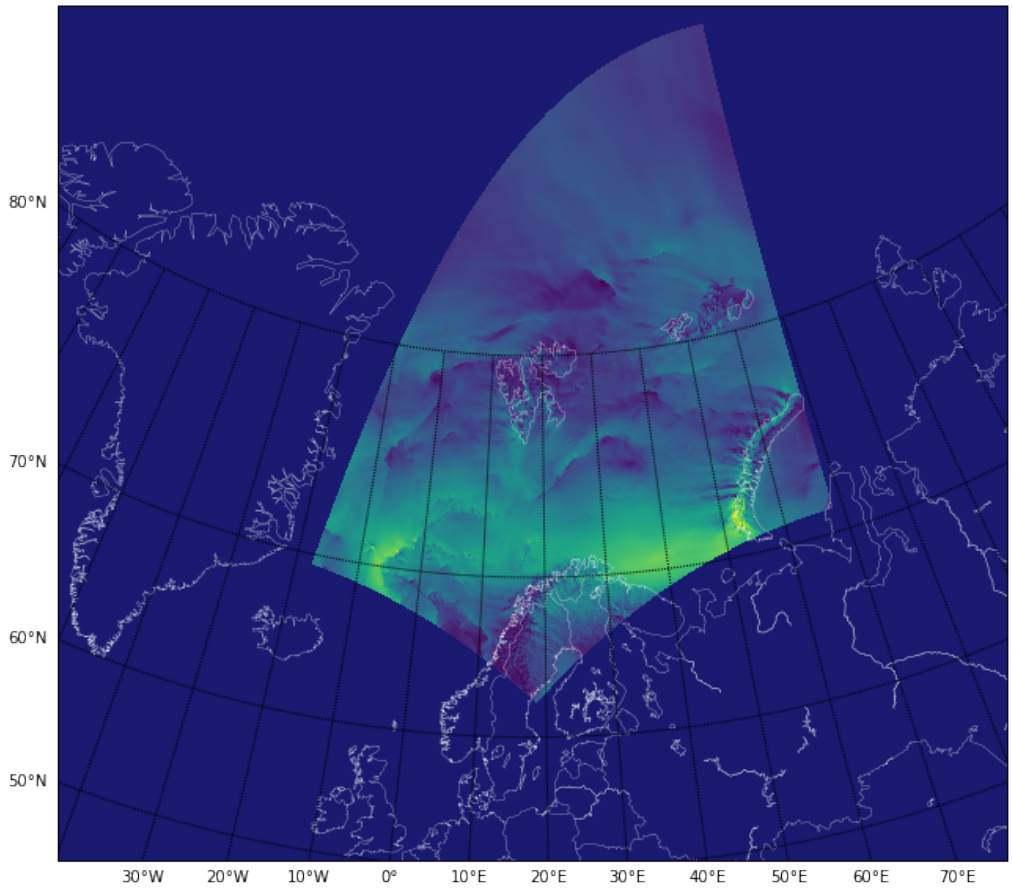

Figure 4.6: The calculated wind speed of the covered area with Arome-Arctic at *2022-02-18 18:00Z*. Based on data from MET Norway

The model itself is based on a HARMONIE-AROME, which is a configuration of the ALADIN–HIRLAM NWP system (See Acronymes) [Bengtsson et al., 2017]. The high resolution on 2.5 km grid spacing makes it capable to predict regularities and irregularities. By fetching information on forecast update 8 times a day with an interval at 3 hours, it archives a high level of accuracy. This gives an entire length of a timeseries though out the day due to frequent collection of data and calculated hourly averages in between data collection intervals [Norwegian Meteorological Institute, 2019].

In this thesis, the model is used to survey the potential wind energy in this region. By acessing the THREDDS Data Servers (TDS) and extract the necessary information using METs API without downloading any data locally on the computer. By asserting the latitude and longitude to Cartesian coordinates in the model, an extraction of the nearest 2,5 km grid to our location or extraction of a sub-region. The wind speed is extracted, seen i figure 4.8. The data given by MET has $\vec{x}$ and $\vec{y}$ values for the wind, therefore the direction is computed with equation 4.7. The $arctan2$ is a function used in programming to get Cartesian coordinates (x, y) converted into polar coordinates (r, θ_p) given in radians. The addition of 180 is to alter their origin into correct the correct quadrants and the $\frac{180}{\pi}$ is to convert radians into degrees. [Grange, 2014].

$$\theta_p = 180 + (\frac{180}{\pi}) \times \mathbf{arctan\,2}(\frac{\vec{x}}{\vec{y}}) \tag{4.7}$$

After gathering all the data from MET using the method mentioned above, a dataset in the format *xlsx* is created with hourly values on wind speed and direction. Example on extracted data is shown on the next page.

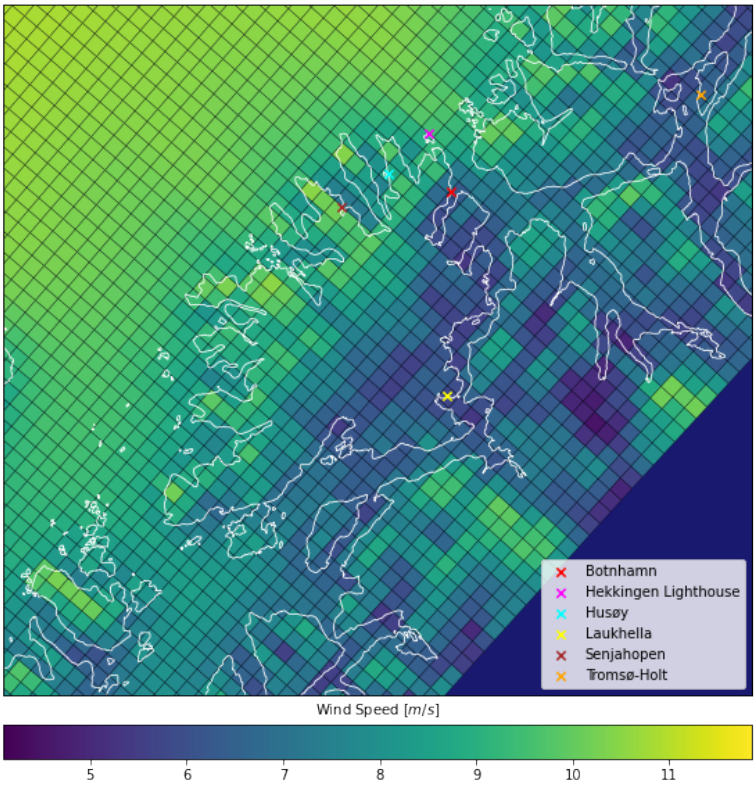

Figure 4.7: The average wind speed in 2020 with AROME-Arctic data plotted in each grid section. Coordinates for the points is given in table 4.2. Based on data from MET Norway.

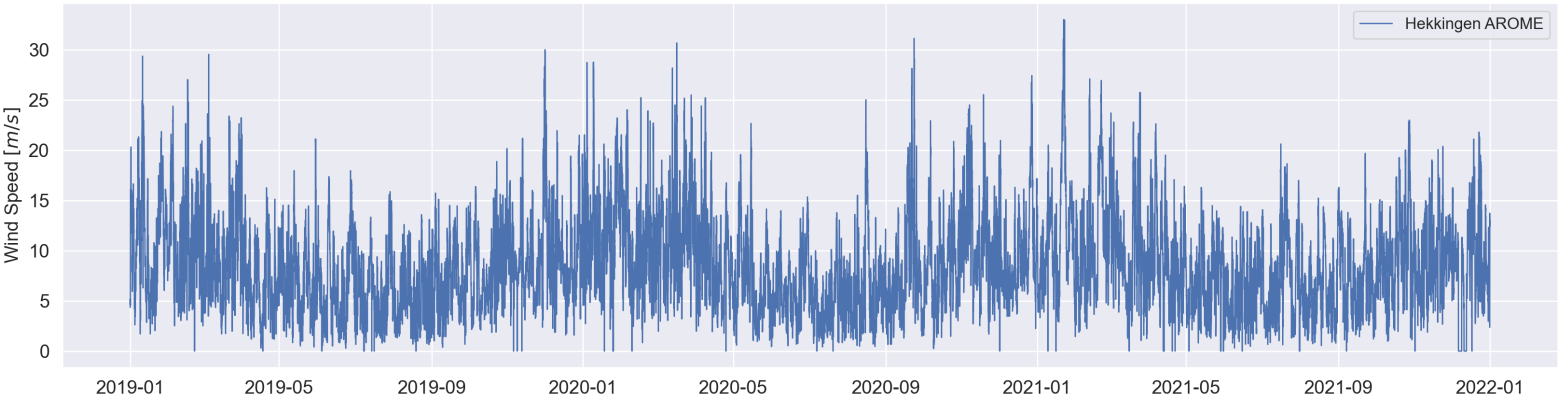

Figure 4.8: The wind speed extracted from the AROME-Arctic model at the grid cell containing Hekkingen lighthouse. Based on data from MET Norway.

4.4 Observations

4.4.1 Agrometeorology Norway (LMT)

The Norwegian Institute of Bioeconomy Research (NIBIO) is one of the largest contributes to exploiting biological resources from land and sea. NIBIO provides a service named Agrometeorology Norway with a Norwegian acronym LMT. The network of weather stations started in 1987 and provides numerous weather data, such as solar radiation, air temperature, etc. In total there are 68 stations, where this thesis uses the station located in Tromsø, "Holt" where coordinates is given in table 4.2. Hourly average observations on temperature, wind speed, wind direction and global radiation was downloaded.

LMT uses physical equipment to measure the parameters used in this thesis. The air temperature has an accuracy on $\pm 0.1°$ or $\pm 0.2°$, depending on the installed measuring device. The precipitation is measured using a instrument which has wind screening and measures throughout the year with an accuracy on ± 0.1 mm. Snow depth measures the distance between the ground using a sensor, and has an accuracy on ± 1 cm. The measurements are given in an hourly mean of the depth. Wind speed and direction is measured as an absolute value in the horizontal plane and the direction is given from 0° to 360° (0° or 360° is North and 180° is South). Global radiation is the sum of direct and diffuse solar radiation in the wavelength range of 285nm - 2800nm. It's measured with a pyranometer, which quantify amount of radiation on the horizontal surface.

4.4.2 Norwegian Centre for Climate Services

NCSS collaborates with the Norwegian Meteorological Institute (MET), the Norwegian Water Resources and Energy Directorate (NVE), Norwegian Research Centre (NORCE), and the Bjerknes Centre for Climate Research. NCSS was established for the purpose to provide easily accessible information for decision makers to make an climate change adaption. Including to supply relevant information, NCSS produces climate and hydrological data for impact studies of climate change on nature and society.

From the NCSS website, https://klimaservicesenter.no/ an easy interface is made to easily extract data from different weather stations. The downloaded weather observation from Hekkingen lighthouse was hourly average observations on temperature, wind speed and wind direction. This is the closest station to the locations of interest which monitors wind parameters. The stations at Botnhamn, Laukhella and Senjahopen is mainly used for the measurements on snow depth or

snowfall.

Table 4.2: The different relevant locations used for data collection for both models and observations.

Location	Coordinates
Botnhamn	69.5212° N 17.9175° E
Hekkingen Lighthouse	69.6005° N 17.8312° E
Husøy	69.5457° N 17.6715° E
Laukhella	69.2349° N 17.9014° E
Senjahopen	69.5000° N 17.4833° E
Tromsø-Holt	69.6538° N 18.9095° E

4.5 PandaPower

Pandapower is a *Python* model library which uses data analysis library *Pandas* and the power system analysis toolbox *PYPOWER*. Combining these libraries creates an easy-to-use network calculation program with an aim at automation and optimization of power systems. *Pandapower* has then become a stand-alone power system analysis toolbox with models and multiple solvers. The program can simulate both static and quasistatic analysis, where the power flow calculation is solved based on the Newton-Raphson method. It's an open-source tool developed by the University of Kassel and Fraunhofer Insitute for Energy Economics and Energy System Technology (IEE) [Thurner et al., 2018].

4.5.1 Network

The method to model an electrical network is an element-based network. Instead of using the bus-branch model, which is an accurate mathematical representation but often is error-prone. The element based model is less troublesome and uses separate model for its supportive electrical components. This creates a tabular data structure, meaning each table represents an element type including parameters. The output of any calculation is presented likewise and is easy to use. In table 4.3 all relevant elements and input parameters are listed [Thurner et al., 2018].

Table 4.3: The Relevant elements used in modelling a network with the necessary input parameters to execute a power flow analysis.

Element	**Input Parameter**
External Grid	Voltage at node [p.u]
	Angle at node [Degree]
Transformer	High voltage bus [kV]
	Low voltage bus [kV]
	Rated apparent power [MVA]
	Short circuit voltage [%]
	Real component of short-circuit voltage [%]
	Iron Losses [kW]
	Open loop losses in [%]
	Transformer phase shift angle
Lines	Line length [km]
	Line resistance $[\Omega/km]$
	Line reactance $[\Omega/km]$
	Line capacitance $[nF/km]$
	Maximal thermal current [kA]
Bus	Rated voltage at bus [kV]
Static Generator	Active power [MW]
	Reactive power [MW]
Load	Active power [MW]
	Reactive power [MW]
Storage	Active power [MW]
	Reactive power [MW]
	Energy capacity [MWh]

4.5.2 Simulation

In this thesis a Quasi-Dynamic simulation was used, meaning a series of power flow simulation in a chosen period. Pandapower has simulation controllers that update values for all relevant elements according to each time step. By making this object-oriented framework, users are able to use different control strategies.

The controllers are divided into different types of controllers, i.e *BasicControl* and *ConstControl*. Basic control is the base controller class, which could be subclassed when implementing custom controllers. ConsControl is specifically made for time series module. It reads data from a DataSource and implements data back to the net and write values to element table. Both controllers served its purpose in this thesis, where BESS used basic, and the rest used const. The reasoning for the use of a basic controller is to be able to update the SOC and charging/discharging of the BESS.

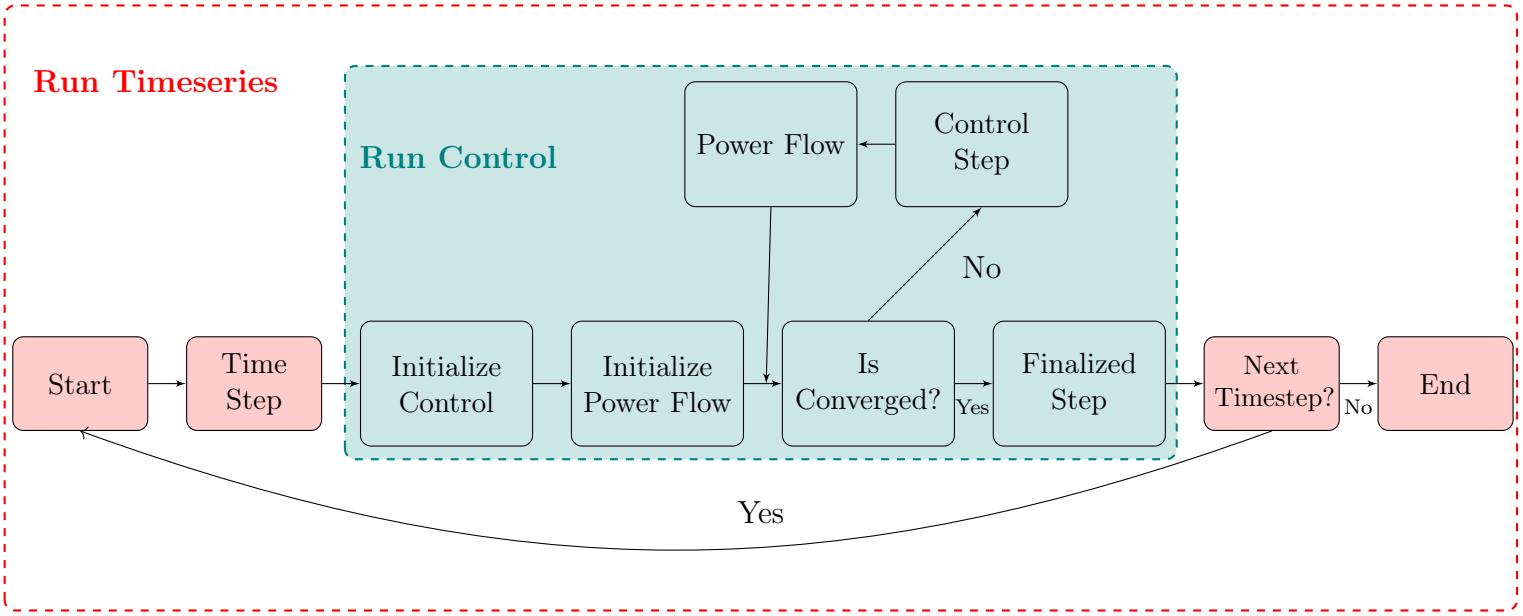

Figure 4.9: A schematic diagram illustrating the structure of the time series simulation and controller simulation. Figure is inspired by [Thurner et al., 2018].

Four periods are simulated for the distribution network. The periods two first are chosen to include the early stages of PV production, high wind power production and high load. The third period is chosen to simulate low PV production, medium wind power production and moderate load. The last period has several power failures where injection might solve some issues. The periods are:

- Period 1: 12/03 00:00 - 18/03 23:00
- Period 2: 27/04 00:00 - 03/05 23:00
- Period 3: 09/08 00:00 - 11/08 23:00
- Period 4: 19/08 00:00 - 25/09 23:00

The simulations include a system with BESS, BESS + PV, BESS + Wind power and BESS + PV + Wind power. The distribution network is set up close to figure 4.10, where the schematic a is simplified. Some assumptions were made to cut down the modelling process and development time. The discussion of consequences and verification of the model is given in the network analysis section 6.1.

The system is assumed to be in a steady state, to limit the stability issues of on and off switching of production. As mentioned earlier, hydro power plants strategies to gain maximum economical profit. The switching of the BESS was not caught, due to the complexity of it in a critical network. Since the purpose is to design and evaluate the mitigation of voltage issues form injection of renewable sources, switching injections on and off was not considered. The only purpose of the switches in schematic 4.10 is to evaluate different production sources not simultaneous.

The loads are also considered to be symmetrical and balanced since their all from one industry location. During the simulation, there is also assumed no fault or disturbances interfere. The last period consists of multiple faults reported in the provided data. The reason of the simulation during this period is to evaluate the voltage situation and new improvement. They are also limited to not supply any reactive power support.

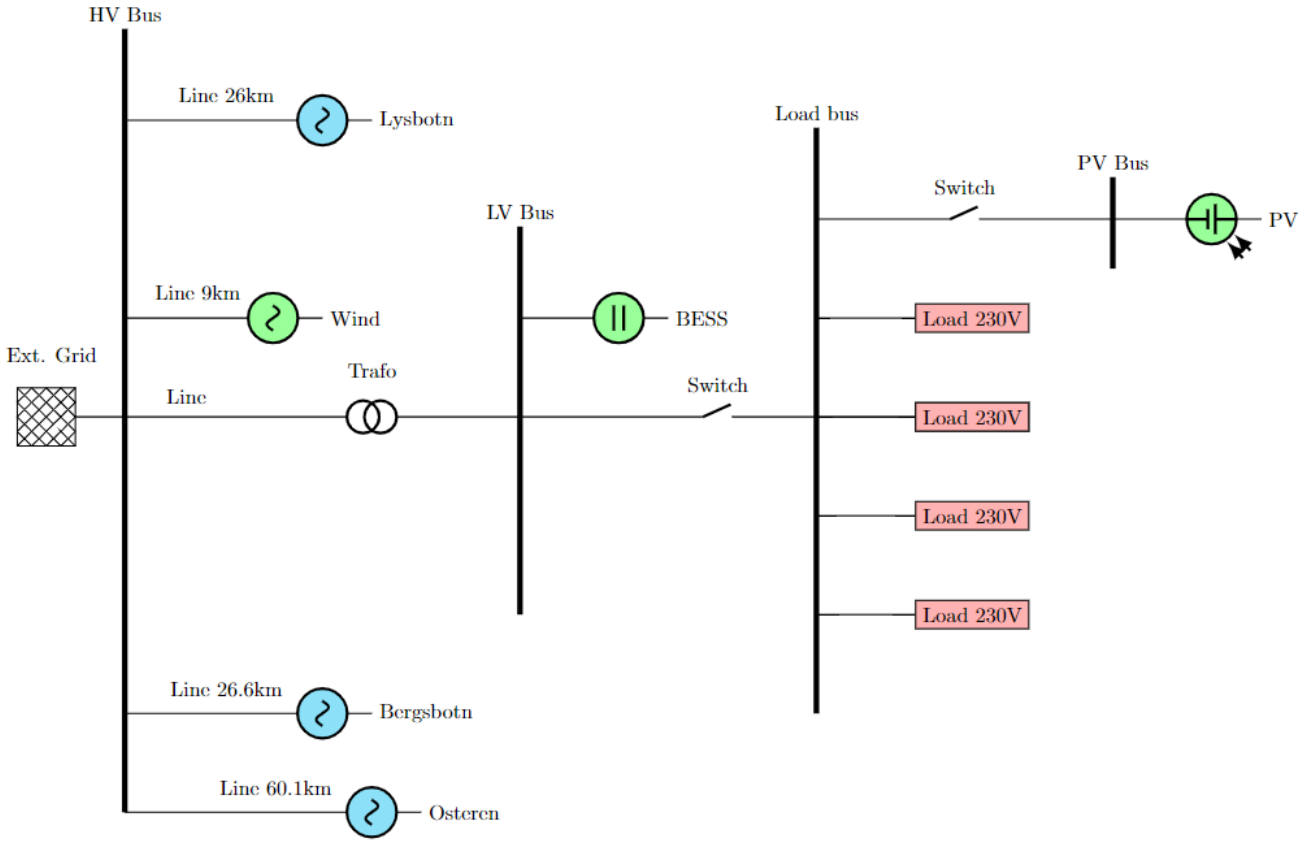

Figure 4.10: A simplified schematic of the PandaPower network of the simulations.

4.6 ArcGIS

ArcGIs is a geographical information software (GIS) produced by Esri which enables users to create interactive maps. The maps are able to contain all types of data to manage or analyse. By connecting data to a map and integrating location data, helps users to analyse patterns, relationships, and geographical context. GIS is used by several industries and are highly efficient on communicating to better management and decision making [Esri, 2022].

In the sea of enormously amount of geoprocessing tools, only a few is used in this thesis to create a solar map. To create a solar map, the most crucial date to obtain is a digital surface model (DSM). DSM is a three-dimensional representation of the bare-earth's surface. It contains arrays with values, which is calculated using a LiDAR system and captures natural and built features on the scanned surface. This differs from the digital elevation model (DEM), which captures bare-earth raster grid corresponding to vertical datum, specifically natural and built features are filtered out [Mallet and David, 2016].

The Norwegian Mapping Authority offers a various digital elevation datasets, which is available at Høydedata.no. From the national elevation model, an DSM with the resolution on $1m \times 1m$ was ordered (TIF-files) and used. In addition, using elevation data, the building footprints as a shapefile and were also obtained for the purpose of solar estimate on rooftops. It's obtained from *Geodata*, where connection to their ArcGIS server gives access to selected data.

From The Norwegian Mapping Authority, several TIF-files which covers the desired location, therefore all TIF-files were merged using the *Merge Rasters* function. To separate land and sea, a mask were created using the raster calculator. The raster calculator is a tool that allows map algebra expression returning a raster as output. By using using the expression $Raster.TIF > 0$, the output returns a raster with value 0 (ocean) and 1 (land). To reduce the file size of the merged raster, *Extrat by mask* was used to exclude the ocean using the land mask. The building footprint were also used as a mask on the merged raster to obtain data for solar calculations on rooftops. To reduce the file size additionally (reduce computational time), *Resample* with resampling technique cubic to a resolution $5m \times 5m$ was used. The technique preforms a cubic convolution and computes the new cell value based on fitting a smooth curve through the 16 nearest input cell centres [Esri, 2022]. The computational time was drastically reduced and a high resolution was kept.

Mapping the solar potential for the desired location, the tool *Area Solar Radiation* (ASR)

would quantify the amount of solar radiation. The ASR-function in determine the solar irradiance based on direct and diffuse radiation. Adding both together gives the global radiation, $Global_{tot} = Dir_{tot} + Dif_{tot}$. Parameters used in the calculation are the solar flux, transmissivity of the atmosphere, azimuth angle, zenith angle, etc. These parameters define a sky map and are essential in the total solar calculation. Detailed information on the function beside in this thesis is found at http://bitly.ws/rTsm.

In the calculation of the solar map, the option of custom parameters for diffuse proportion and transmittivity. In another thesis written by [Falklev, 2017], the parameters were found at *Holt*. The diffuse proportion describe the relationship between diffuse and direct radiation, and transmittivity scales the amount of incoming radiation passing through the atmosphere. The values range ($only\ direct$) $0 \leq$ diffuse proportion ≤ 1 ($only\ diffuse$) and $0 \leq$ transmittivity ≤ 1. These values are set accordingly to table 4.4 for the monthly solar map calculation [Falklev, 2017].

Table 4.4: Diffuse proportion and transmittivity value for each month in Tromsø [Falklev, 2017].

Month	Diffuse Proportion (D)	Transmittivity (T)
January	0.9	0.8
February	0.6	0.7
March	0.5	0.6
April	0.4	0.6
May	0.5	0.5
June	0.4	0.5
July	0.6	0.4
August	0.3	0.6
September	0.4	0.6
October	0.5	0.7
November	0.7	0.8
December	X	X

To quantify PV production using ArcGIS, a method proposed by [Eikeland, 2019] using the PV modules technical data and solar radiation values from ASR was used in the raster calculator. The approach is listed underneath, and parameters are listed in table 4.5:

1. Find number of arrays to reach a 1 kW peak:

$$N_{peak} = \frac{1000}{Array_{peak}} = [\frac{1}{kW_p}] \tag{4.8}$$

2. 1 kW peak per square meter:

$$A_{peak} = N_{peak} \times A_{PV} = [\frac{m^2}{kW_p}] \tag{4.9}$$

3. Solar radiation per kW peak:

$$B = \frac{GHI \times A_{peak} \times PR \times \eta_{PV}}{1000} = [\frac{kWh}{kW_p}] \tag{4.10}$$

4. Estimated power per square meter:

$$P_{m^2} = \frac{B}{A_{peak}} = [\frac{kWh}{m^2}] \tag{4.11}$$

5. (Optional) Total PV production of an array system:

$$PV\ Production = P_{m^2} \times A_{total} \tag{4.12}$$

Table 4.5: A table representing the relevant input parameters to estimate PV production.

Parameter	Description
GHI	Solar Radiation in each period $[Wh/m^2]$
PR	Performance Ratio [%]
η_{PV}	PV array efficiency [%]
A_{PV}	Total area of PV array $[m^2]$
$Array_{peak}$	The Watt peak of the chosen PV array $[W]$

The power production potential on the surface can be computed for different time frames. In this thesis the yearly and daily solar radiation for 2020 calculated, to evaluate the most suitable location for PV.

4.7 Peak Load Shaving with BESS

Peak load shaving has been more utilised at power grid since power demand significantly increases. Peak load shaving proposed by [Rahimi et al., 2013] suggest a simple, yet effective method. The proposed algorithm re-calculates the average aggregated load profile (P_{av}) after each time interval (τ) for the next utilization period (u_p). The charge/discharge are based on its own capacity compared to the total capacity of the BESS. This quantifies the charge/discharge rate determined by the utilization factor (u_f). The utilization factor determines the amount to shave from the actual load, which is above P_{av}, i.e u_f is defines as $0 \leq u_f \leq 1$ which $u_f = 1$ will try to shave all load above P_{av} and $u_f = 0$ does not operate at the moving mean. With inspiration from [Jacobsen, 2019], the proposed algorithm is changed to some extent, such that it finds the most optimal u_f.

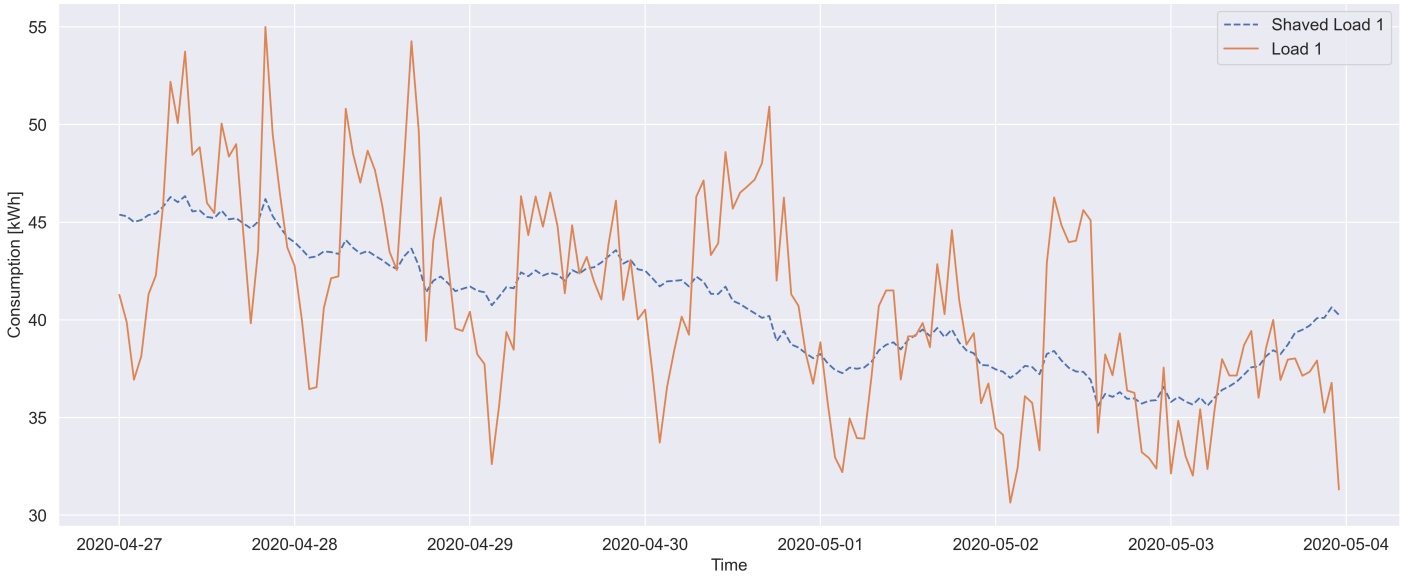

Figure 4.11: Example of the shaved loads using the algorithm proposed in this thesis.

For each time step, the charged/discharged energy for the battery can be expressed as:

$$|E_{BAT}| = (P_{actual} - P_{avg}) \times u_f \tag{4.13}$$

hence, the absolute charged/discharged battery power is defined as:

$$|P_{BAT}| = \eta \frac{|E_{BAT}|}{\tau} \tag{4.14}$$

η is the round-trip efficiency for the BESS. The power is dependent on the constrains, therefore limits are to set at the maximum rate of charge/discharge power. The first condition can be is given as:

$$P_{min} \leq \frac{|P_{BAT}|}{\tau} \leq P_{max} \tag{4.15}$$

Which limits exceeding values to be set equal as the maximum or minimum power. The second condition set the state of charge of the battery to be within predefined boundaries, that is:

$$SOC_{min} \leq SOC \leq SOC_{max} \tag{4.16}$$

Running the algorithm, the initial value for u_f is set to be 1. For each run in the utilization period, the algorithm examines if complete discharge occurs. If this is true, u_f is lowered and run again until a suitable u_f is found [Masters, 2013].

5 / Performance of Renewable Generation

5.1 Statistical Analysis of the Weather

In this section the different methods for statistical analysis are presented. The MBE, MAE, RMSE and the Pearson correlation coefficient is calculated using measured data from Holt, Husøy and Hekkingen lighthouse. The data elapse almost three years of hourly values. From 2019 to 2021, some hourly values where not registered, and are therefore replaced with a timestamp with value zero. Hekkingen lighthouse lost 21 registrations which will not have a large impact on the overall calculations. Holt's wind speed and direction registrations device failed during larger periods in the end of 2021. Data points regarding wind measurements from *17/11/2021-31/12/2021* at Holt have been removed due to poor quality. The pyranometer at Husøy was installed and active from *01/03/2019*, and only misses 1 registration till *30/12/2021*. Therefore, the data from the ERA5 model is limited during statistical calculation to corresponding time period.

Table 5.1: The yearly solar radiation from the the ERA5 model and the measured values.

Yearly Solar Radiation $[kWh/m^2]$			
Year	2019	2020	2021
ERA5 Husøy	679.86	657.75	611.90
Husøy	804.16	886.39	846.89
ERA5 Holt	560.18	531.3	490.26
Holt	724.70	717.15	660.72

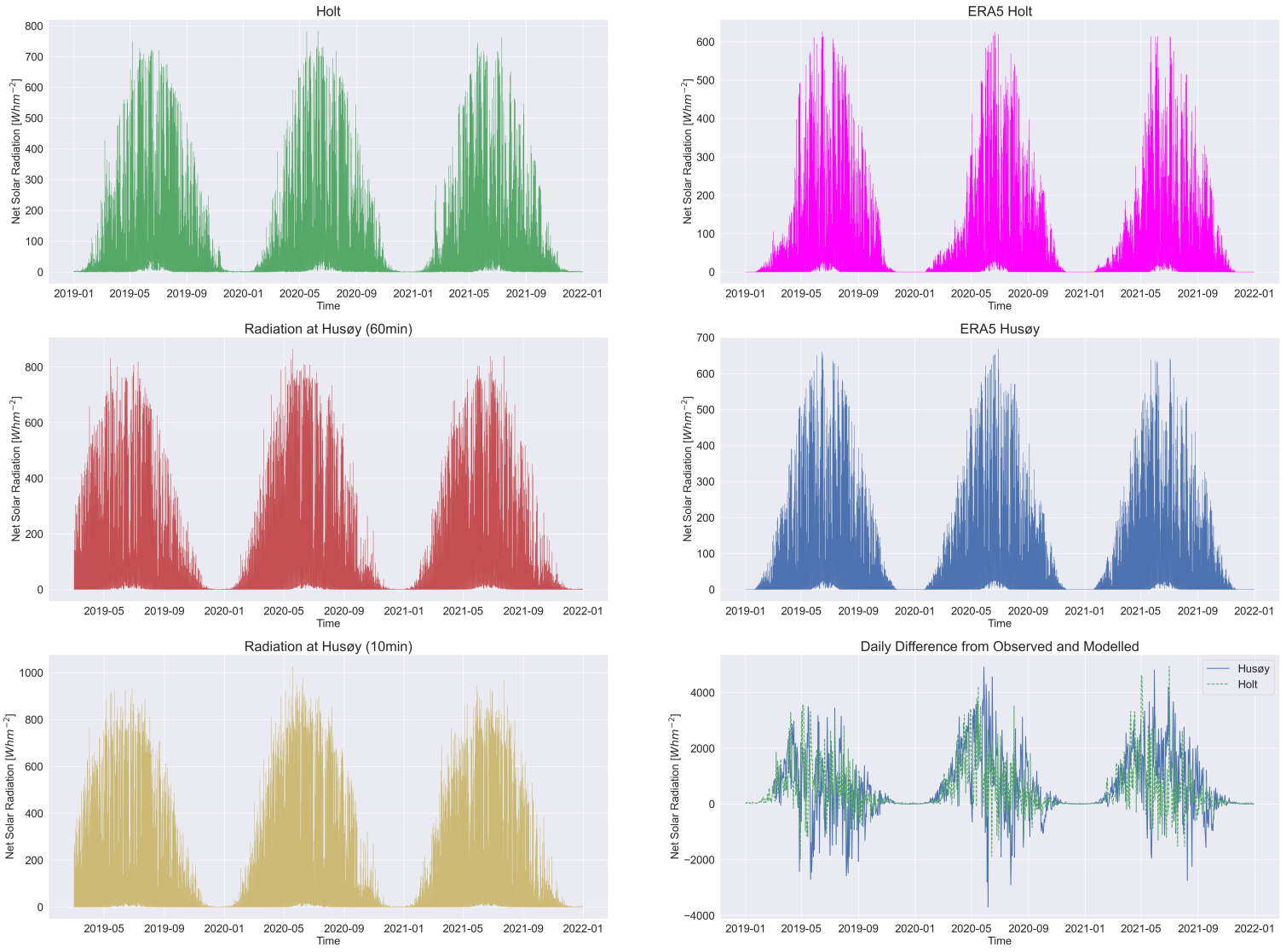

Figure 5.1: Solar radiation at Holt and Husøy for both observed measurements and modelled data from the ERA5 model. Bottom right is the difference in solar radiation from observed and modelled data. $Observed_{data} - Model_{data} = Difference$.

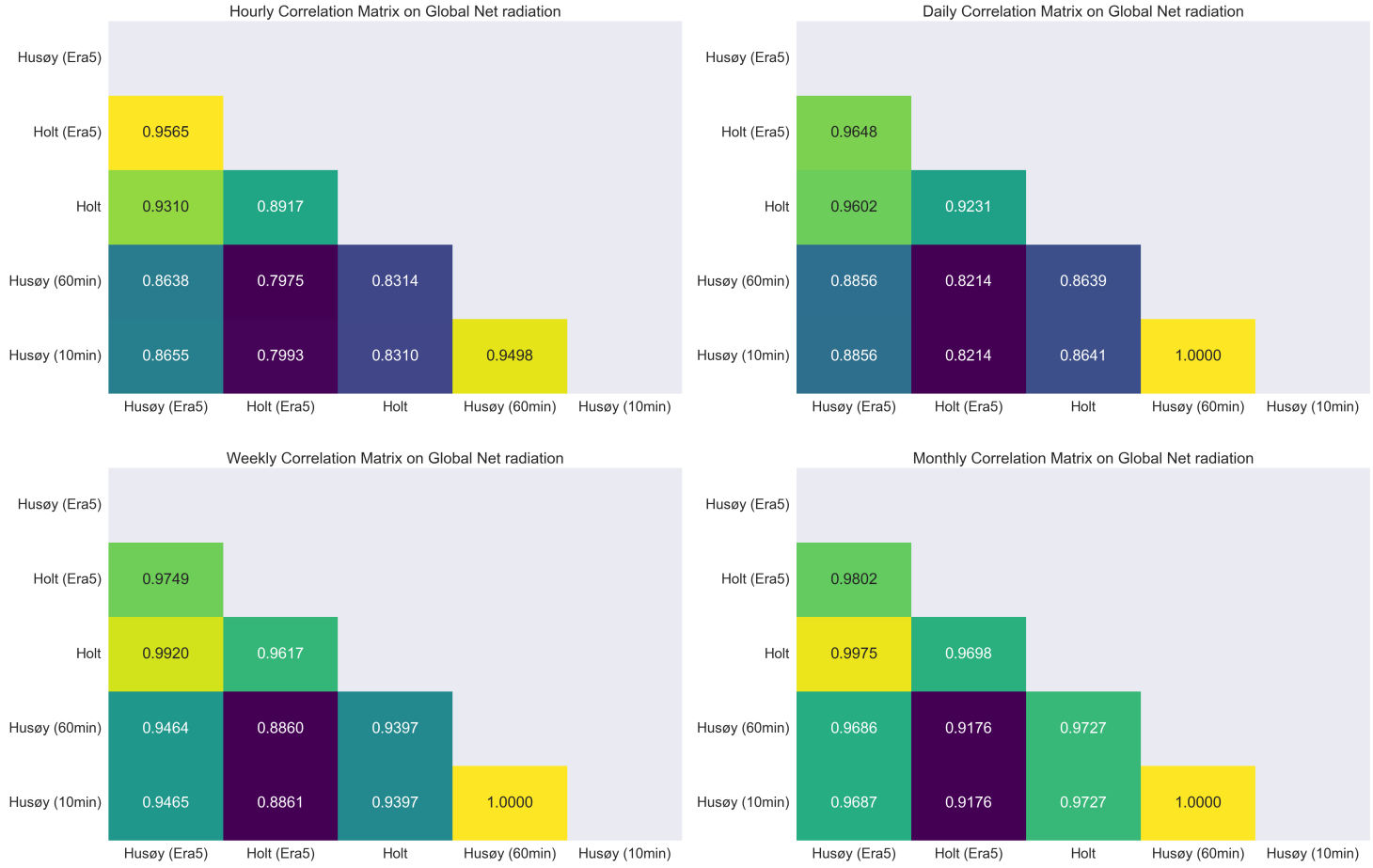

Figure 5.2: The correlation coefficient in a matrix for hourly, daily, weekly and monthly global solar net radiation.

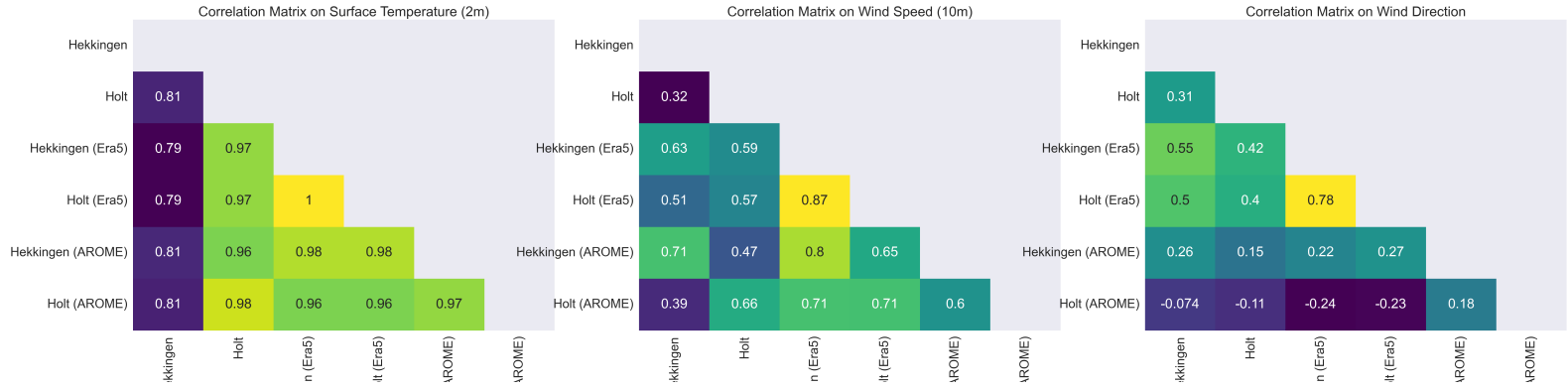

Figure 5.3: The correlation coefficient for temperature, wind speed and wind direction in a matrix for hourly data.

Table 5.2: The result of statistical methods explained in section 4.1 presented in a table. The two main stations is Holt and Hekkingen with two main models, ERA5 and AROME. The hourly datasets were used.

Holt	ERA5	AROME	ERA5	AROME	ERA5	AROME
Parameter	RMSE		MBE		MAE	
Temperature [$C°$]	1.7333	1.248	-0.0457	0.343	1.3062	0.8652
Wind Speed [m/s]	1.4609	4.4549	0.1301	-3.3759	1.1392	3.4821
Wind Direction [°]	97.2395	152.7742	-16.4564	-54.3853	61.8234	109.0165
Solar Radiation [Wh]	69.9339	-	19.8003	-	30.7476	-
Hekkingen	ERA5	AROME	ERA5	AROME	ERA5	AROME
	RMSE		MBE		MAE	
Temperature [$C°$]	4.0434	3.5323	2.0272	1.2483	2.2699	1.9428
Wind Speed [m/s]	3.3478	4.1055	1.075	-2.3052	2.7063	3.1998
Wind Direction[°]	88.9994	118.7321	4.3223	1.7801	50.034	80.8369

From table 5.2, figure 5.2 and figure 5.3, the AROME model do not consist of a radiation parameter. Since a pyranometer is installed at Husøy, the statistical values can be calculated using ERA5. The hourly values for the statistical calculation resulted in $RMSE = 92.0616\,Wh$, $MBE = 23.8617\,Wh$ and $MAE = 44.5562\,Wh$ for the ERA5 model compared to measurements at Husøy. Meaning it over-predicts the solar radiation, but the error amount differs for RMSE and MAE. The error amount is not large for both parameters, which indicates a fairly accurate prediction. At Holt the AROME-Arctic model slightly over-predicts the temperature (0.343°) and do not have a large number of errors, where RMSE (1.248) is a little higher than MAE (0.8652). The ERA5 model only under-predicts the temperature only a tiny bit (-0.0457) and do not have large amount of errors, like the the AROME-Arctic model. Wind speed and wind directions seems to be harder for the AROME model, rather than the ERA5 model. AROME under-predicting speed with $-3.3759\,m/s$ and misses the direction with $-54.3853°$. The ERA5 over-predicts the solar radiation, but the total amount of error differs from RMSE (69.9339) and MAE (30.7476).

Due to lack of measurements of solar radiation at Hekkingen, only a few parameters were considered. At Hekkingen the overall performance seems to be slight better with AROME rather than ERA5. Both temperature and wind direction are more correctly estimated by AROME, but still under-estimates wind speed. ERA5 seems to struggle a little bit due to somewhat higher RMSE and MAE.

Including using the weather models, ArcGIS was also used to propose a yearly output for 2020. Using the functionalities in ArcGIS makes it possible to extract daily solar radiation for a desired point within the area of a DTM. The daily solar radiatio output is calculated and shown in figure 5.4, where only Husøy and Holt is represented due to comparison with real observed values.

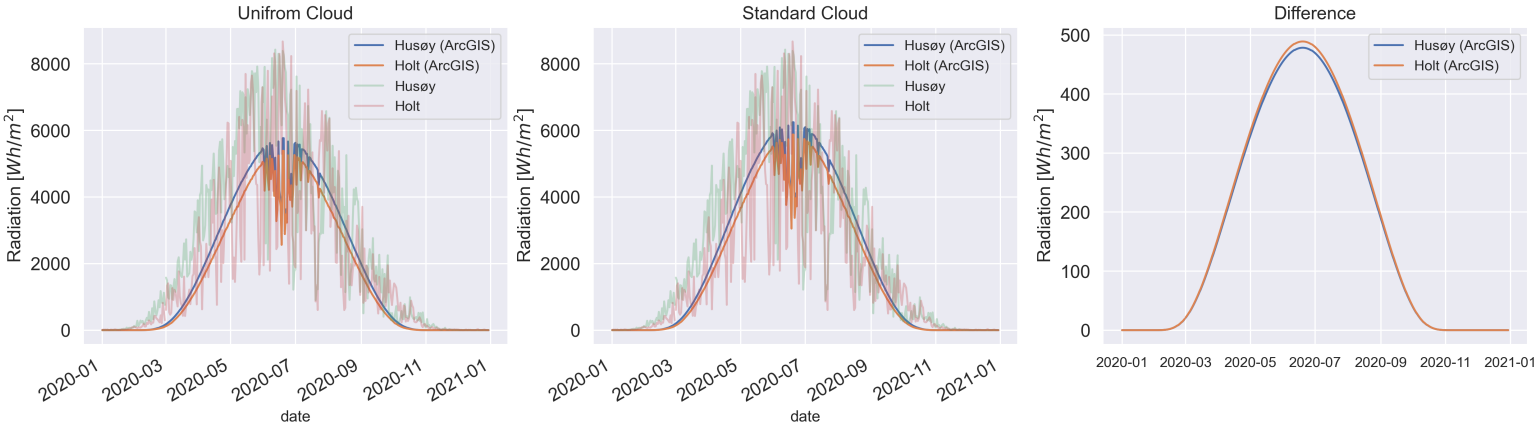

Figure 5.4: The daily solar radiation using ArcGIS with different overcast sky models. The almost transparent data is the observed data. The right plot shows the difference between the two cloud models.

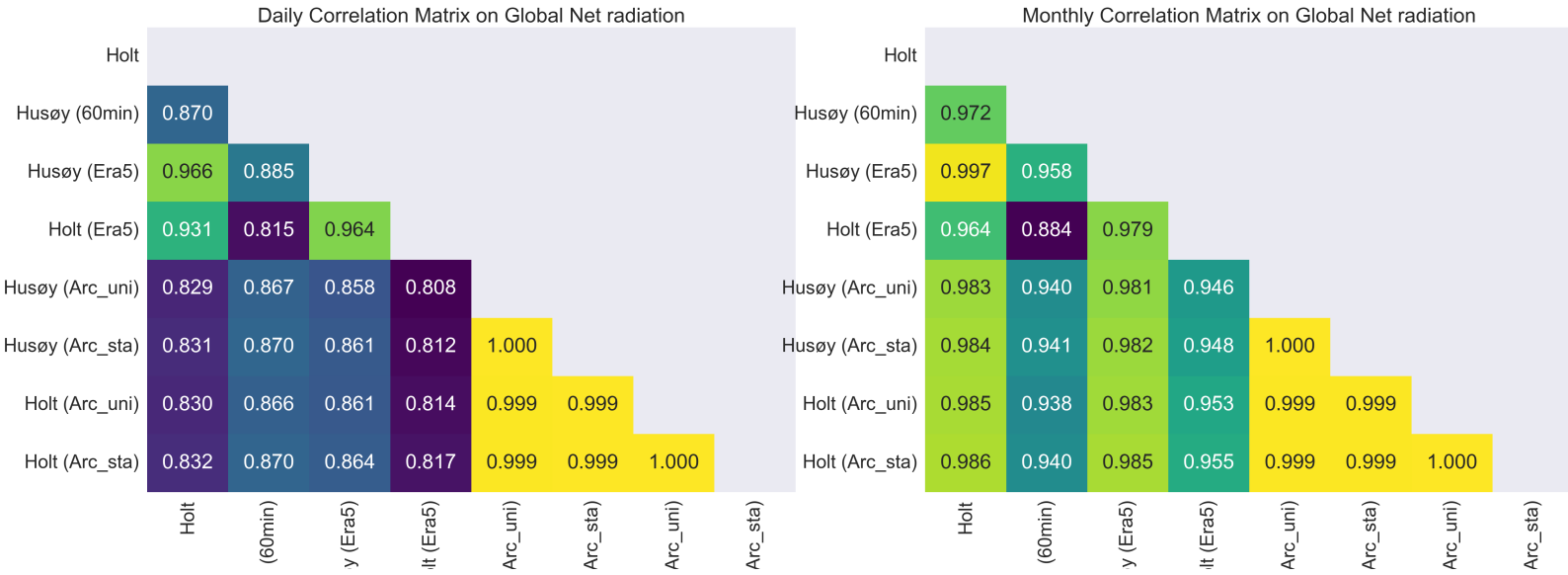

Figure 5.5: The correlation coefficient for ArcGIS data and observed measurements using daily data for solar radiation.

Table 5.3: Statistical analysis of the two different overcast sky models in ArcGIS for two locations.

	Uniform	Standard	Uniform	Standard	Uniform	Standard
Parameter	RMSE		MBE		MAE	
Husøy	1376.6045	1291.7137	576.6567	407.4164	937.3738	869.2231
Holt	1274.779	1245.1162	304.5705	131.5991	812.1906	789.9788

ArcGIS correlates well with the real world data but predicts a smooth radiation until the summer period (May-July). This is why the MBE value indicate an over-estimation by ArcGIS and why the numbers of errors is large for both overcast options. Compared to the observed measurements, ArcGIS don't reach the highest level of radiation, meaning the yearly amount is significantly less than measured data. In 2020 the measured amount was 886.39 kW/m^2 and 717.15 kW/m^2 for Husøy and Holt. ArcGIS calculates 675.33 kW/m^2 (Uniform) and 737.28 kW/m^2 (Standard) for Husøy, and 605.68 kW/m^2 (Uniform) and 668.98 kW/m^2 (Standard) for Holt.

From all the data collected regarding solar radiation, the yearly incoming radiation is listed in table 5.4. The models correlate well but estimates lower peak values. The lower peaks come from calculating the hourly average value. In figure 5.1, the 10 min interval logging data reaches a higher peak rather than the hourly interval for Husøy. Maximum peak for 10 min interval is 1026.6 Wh/m^2 and for 60 min interval is 864.9 Wh/m^2. This applies also applies for the model where hourly data might lose higher peaks.

Table 5.4: The total radiation given in kWh/m^2. Only one year was calculated with ArcGIS, 2020 and both overcast sky models uniform/standard. The red number indicates the collected data which misses data from January and February.

	2021	2020	2019
Holt	660.72	717.15	724.70
Husøy	846.89	886.39	804.16
Holt ERA5	490.26	531.3	560.19
Husøy ERA5	611.90	657.75	679.87
Holt ArcGIS	-	605.68/668.99	-
Husøy ArcGIS	-	675.33/737.28	-

To visualise the difference more easily between the observations and models wind data. Windrose was created for each station with both predicted and measured data. These are polar plots where the direction of wind ranges from $0° - 360°$ with sky direction according to observations. In addition, the hours of which directions is outgoing circles from the centre and the strength of speed is indicated in colour. The total number of hours of the wind speeds represented in histograms in the appendix, figure A.1.

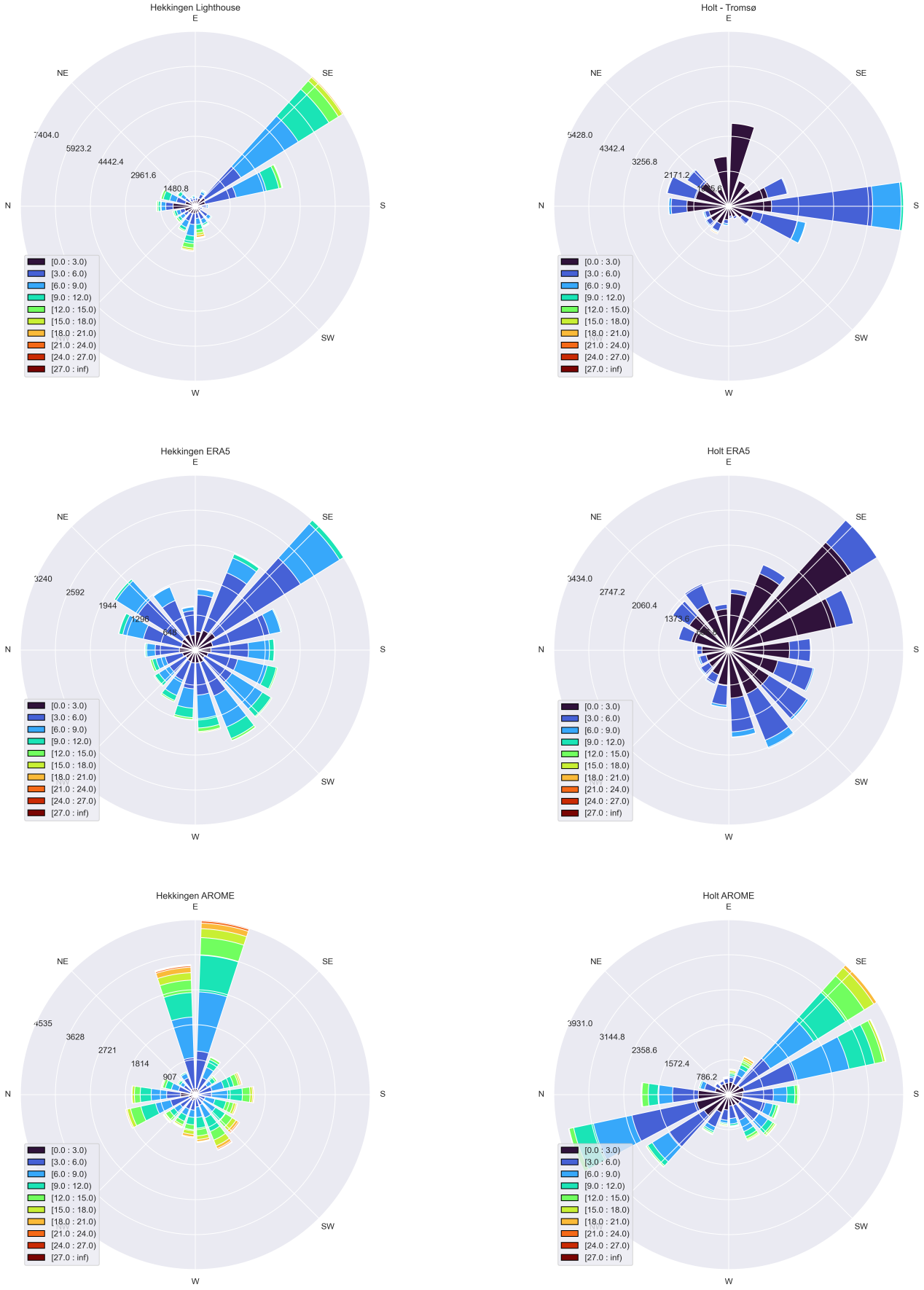

Figure 5.6: Windrose for the different locations. The plotted compass direction is rotated 90° clockwise due to a bug in used python-library, but the wind directions correspond correct to the sky direction.

5.1.1 Performance of PV system

At Husøy there are already 3 existing installed PV panels. In figure 5.14 the solar production is calculated with hourly radiation measurements from Husøy and the ERA5 model. The measured solar radiation is used to calculate electrical production with and without external effects as operating temperature, and other effects listed in appendix A.4.1. The computation using effects on PV panels gives a higher accuracy on the peak production periods and the magnitude but misses production during early (Jan-Feb) and late winter (Nov-Dec). Due to only having daily output and the most amount of error, the ArcGIS data is only used to locate suitable locations for PV at entire Senja. The PV configuration used for computation in table 5.5:

Table 5.5: Configurations of already existing PV system installed at Husøy and Senjahopen [REC, 2020].

REC TwinPeak 2 Mono Series	
Nominal Power - P_{MPP}	310 W_p
Efficiency	18.6 %
Nominal Module Operating Temperature	44.9 $C°$
Temperature Coefficient of P_{MPP}	-0.37 $\%/C°$
Area	1.67 m^2
Performance Ratio (PR)	0.9
Tilt	90 ° / 20 °
Azimuth	180 ° (S) /130 ° (SE)

Table 5.6: Using Radiation data and parameters in 5.5.

Yearly Production 2021 [kWh]			
Installed PV	With measured Rad + temp influence	With measured rad	ERA5 data
1163.15	984.86	569.62	716.45

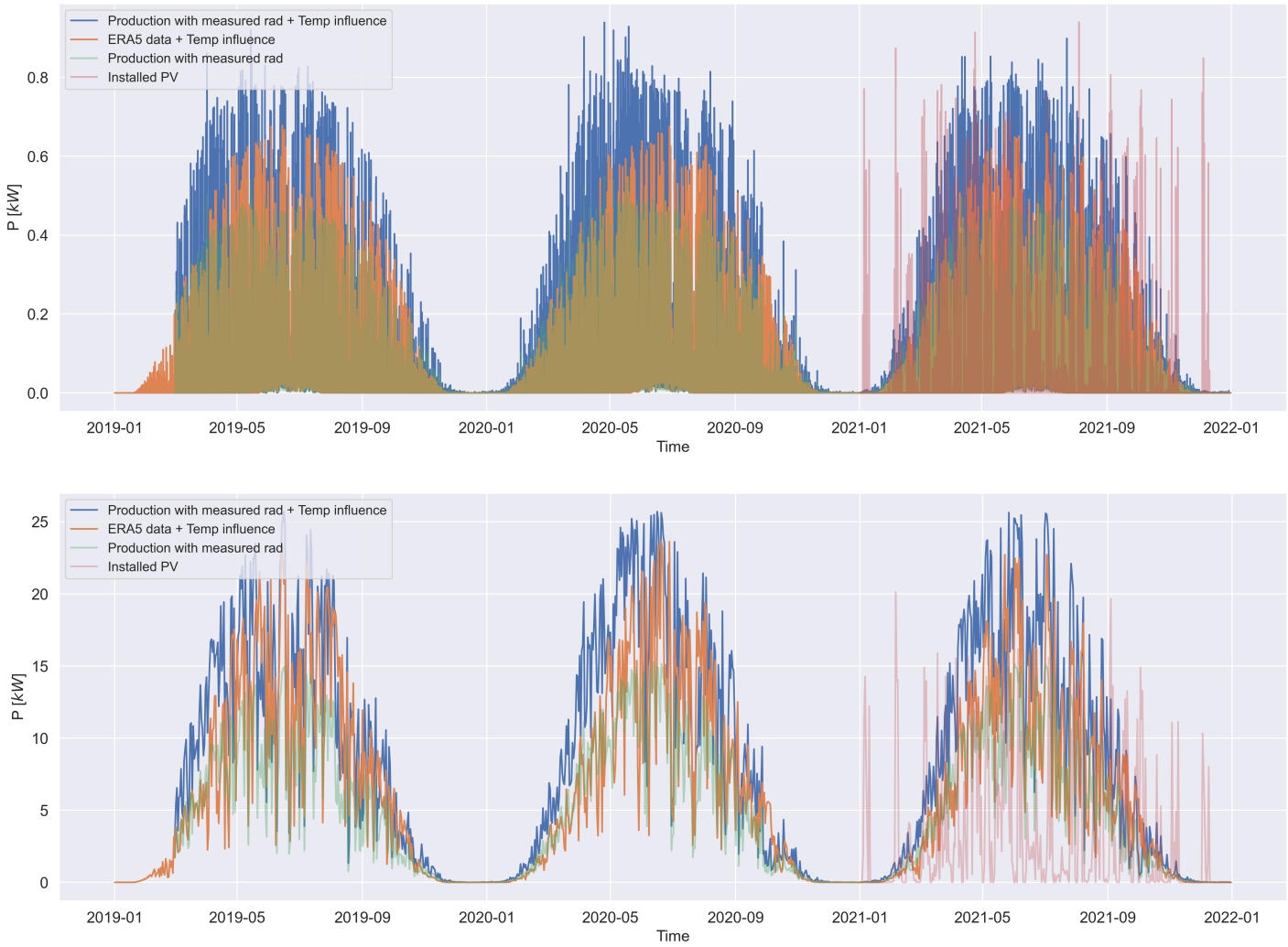

Figure 5.7: Top: The PV production at Husøy with a 90° degree tilt facing south. This corresponds with the already existing PV system at Husøy. Bottom: Daily PV production.

The installed PV system has a tilt at 90° which makes it possible to collect sunlight during the first quarter (Jan-Mar) and firth quarter (Oct-Dec). As the pyranometer isn't installed at the exact same placement as the PV panels, some measurements do not coincide with the PV production. The modelled production follows the incoming radiation data at a higher level than the real measured production. In figure 5.8, a coefficient is calculated to estimate how different tilt angles affect the solar collection. In addition to tilt affecting collection, the PV systems azimuth is calculated to estimate a coefficient on its effect. In figure 5.8 the coefficient is illustrated when its solar noon and ranging from west (-90°) to east (+90°), where 0° is south.

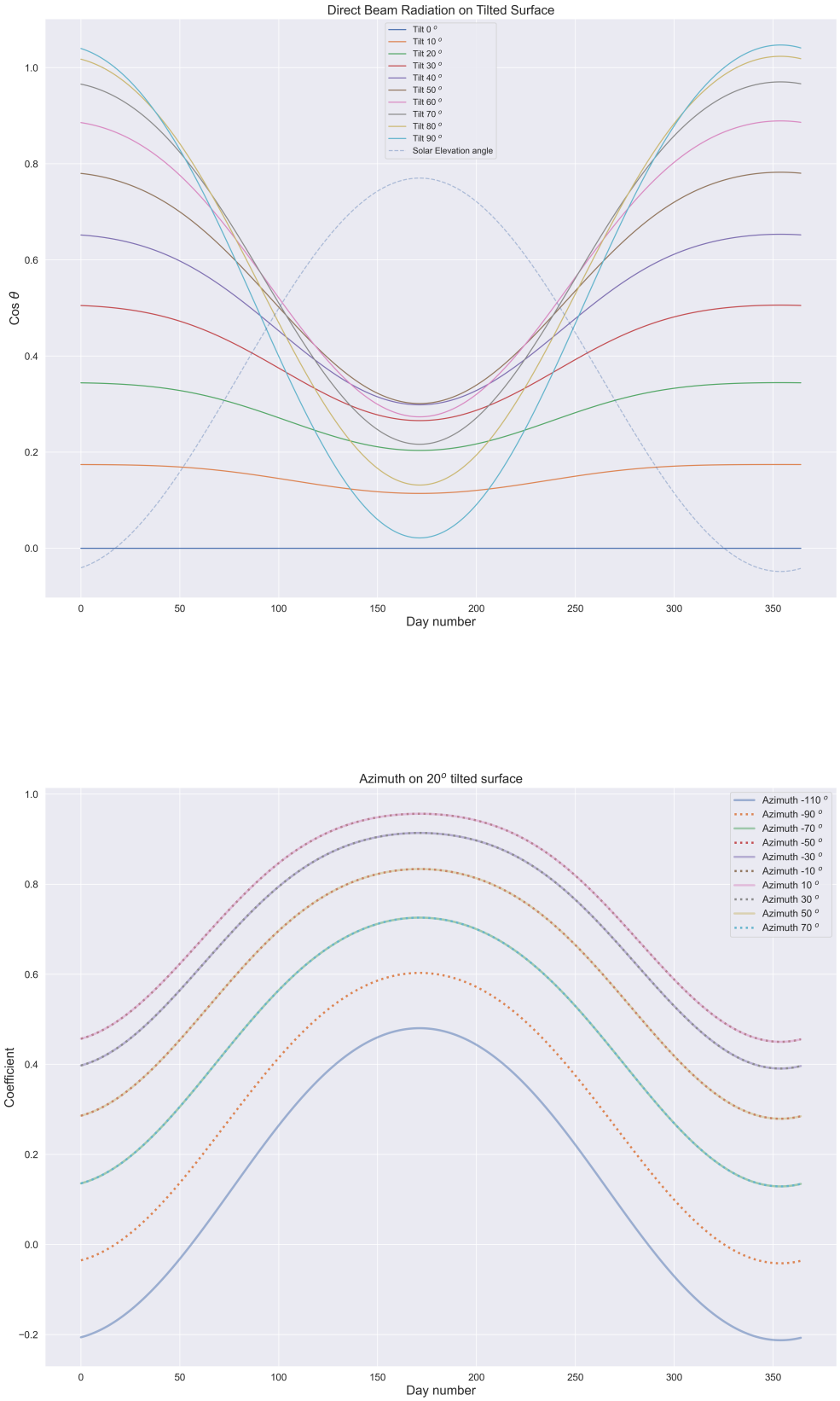

Figure 5.8: Top: The tilt coefficient with the solar elevation angle. Bottom: The azimuth coefficient. Where both calculations were done at latitude $69.32°N$.

The quarterly production at Husøy and Senjahopen clearly show the collection during Q1 and

Q4 during 2021. In the first and fourth quarter, the production during the day is around four times as large as in comparison with ERA5 at Husøy. It is lower at Senjahopen, due to less frequent production which reduces the quarterly average. The second and third quarter is also around two to three times less at than the actual peak production at Husøy. Senjahopen has high peaks during days with high radiation (clear sky) but have less frequent good days compared to Husøy. The ERA5 model simulates a smaller peak at Husøy, but longer periods of collection in both cases. As mentioned, the lower frequency of production reduces the average for Senjahopen. The actual production data has steep curves, where it primarily produces electricity at around 07:00 to 16:00. This is shown in the figure underneath.

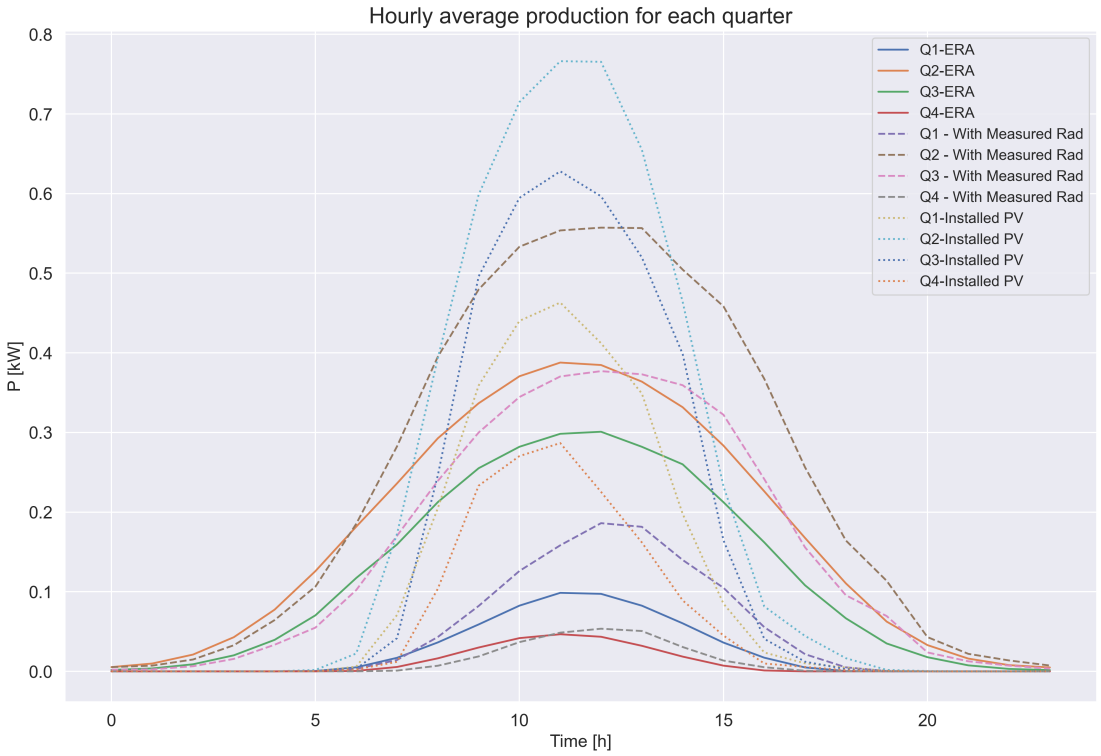

Figure 5.9: The label Q indicates the quarter, and *ERA* is modelled data, only Q label is production with measured radiation and *Installed PV* is the real production for 2021 at Husøy.

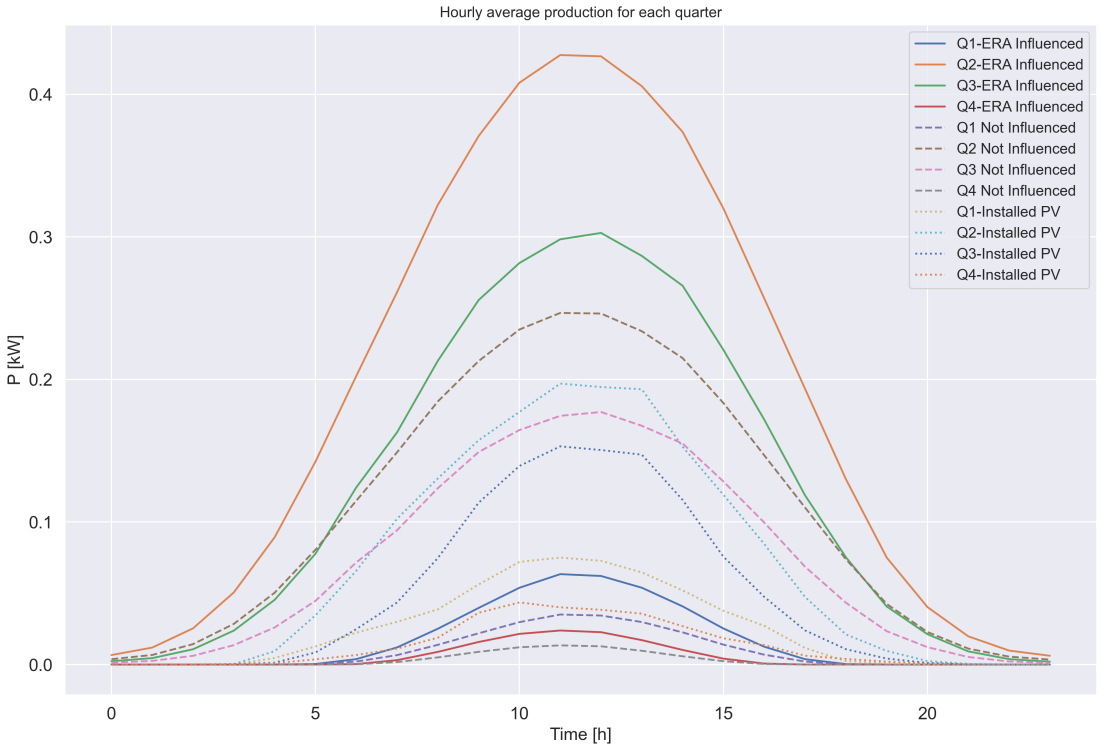

Figure 5.10: The label Q indicates the quarter, and *ERA* is modelled data, only Q label is production with measured radiation and *Installed PV* is the real production for 2021 at Senjahopen.

5.2 PV At Local Consumer

The two largest fish industries at northern Senja, Nerdgård AS and Brødrene Karlsen AS has 10 900 m^2 and 3765 m^2 available surface on the roof [Troms Kraft, 2019]. Placing PV on on of the biggest electrical consumers and assuming the roof construction is solid enough would substantially improve voltage regulation. Since there are plenty of space to avoid casting shadow at each array of PV, the shadow effects on PV are not considered. The derating factor is defined as the performance ratio (PR) and is taken into account to simulate some losses. The panels will also have different PV configurations.

Table 5.7: The different PV configuration used in simulated power production [REC, 2022] [Sunpower, 2022].

	REC Alpha Series (Conf. 1)	Sunpower Maxeon 3 (Conf. 2)
Nominal Power - P_{MPP}	380 W_p	400 W_p
Efficiency	21.7 %	22.6 %
Nominal Module Operating Temperature	44.0 $C°$	44.0 $C°$
Temperature Coefficient of P_{MPP}	-0.26 %/$C°$	-0.29 %/$C°$
Area	1.75 m^2	1.76774 m^2
Performance Ratio (PR)	0.9	0.9
Tilt	50 °	20 °
Azimuth	180 ° (S)	130 ° (SE)

Having 500 PV panels at Husøy for both configuration gives 190 kWp and 200 kWp, using an area of 875 m^2 and 883.87 m^2. The panels orientation is south facing since its one of the more optimal azimuth direction and a slope of 50° gives a high collection rate throughout the year. The production is given in the figures on the next page, where monthly production, yearly production, and capacity factor (CF).

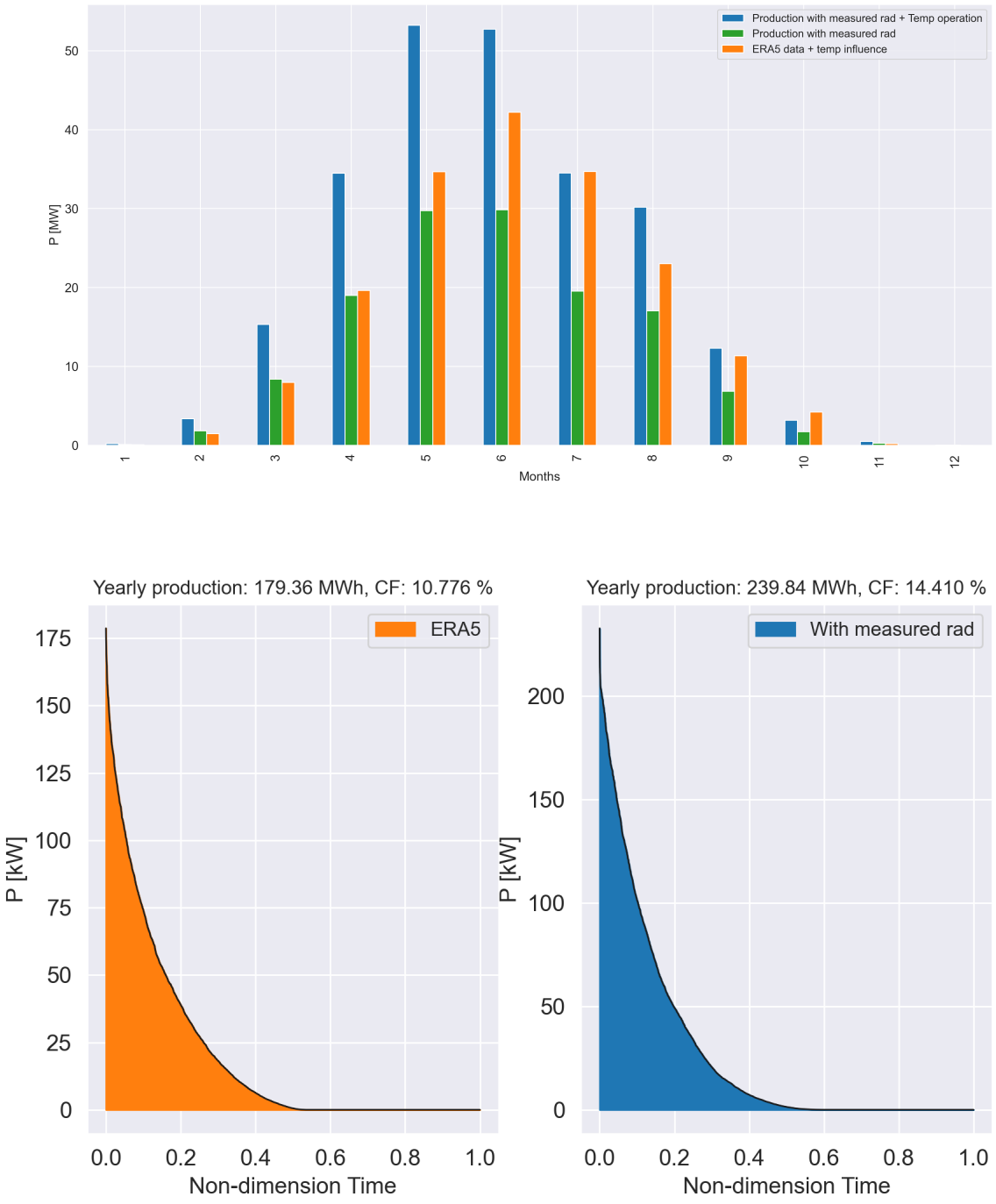

Figure 5.11: Top: 2020 Monthly PV production with the proposed PV configuration 1. Bottom: A Power duration curve for the PV system conf.1 with hourly resolution, where the filled area is the yearly production. This is given in the figure title and its capacity factor.

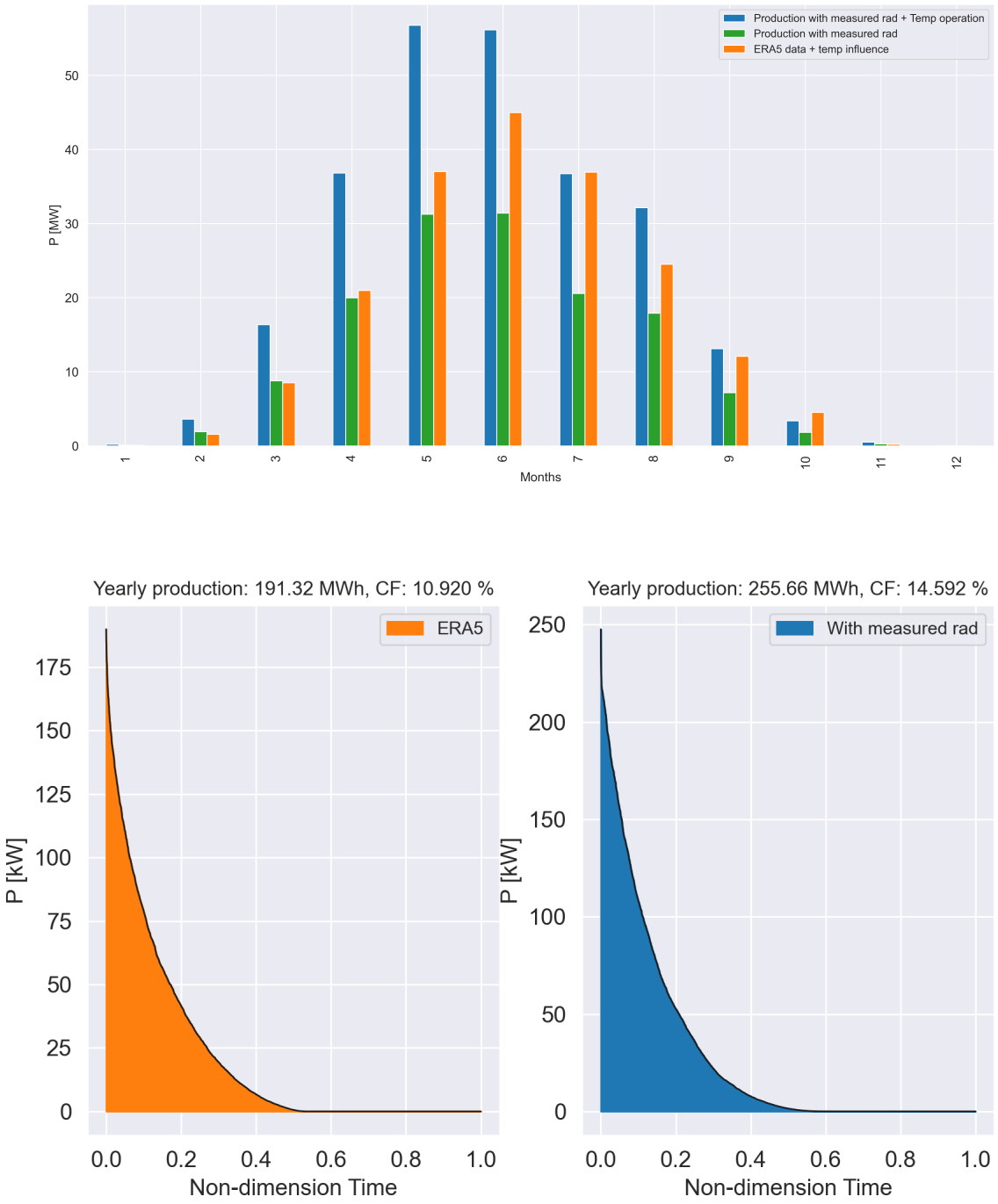

Figure 5.12: Top: 2020 Monthly PV production with the proposed PV configuration 2. Bottom: A Power duration curve for the PV system conf.2 with hourly resolution, where the filled area is the yearly production. This is given in the figure title and its capacity factor.

Having 1000 PV panels at Senjahopen for both configuration gives 380 kWp and 400 kWp, using an area of 1750 m^2 and 1767.74 m^2. The panels orientation is southeast facing since its one of the more optimal azimuth direction and a slope of 20° gives a high collection rate throughout the year. The production is given in the figure's on the next page, where monthly production, yearly production and capacity factor. Since there are no installed pyranometer, only the modelled data from ERA5 is used to simulate the power production.

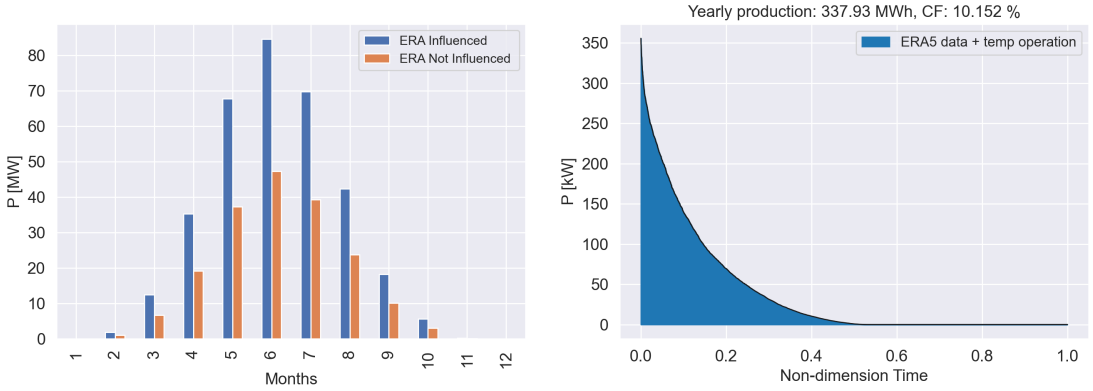

Figure 5.13: Left: 2020 Monthly PV production with the proposed PV configuration 1. Right: A Power duration curve for the PV system conf.2 with hourly resolution, where the filled area is the yearly production. This is given in the figure title and its capacity factor.

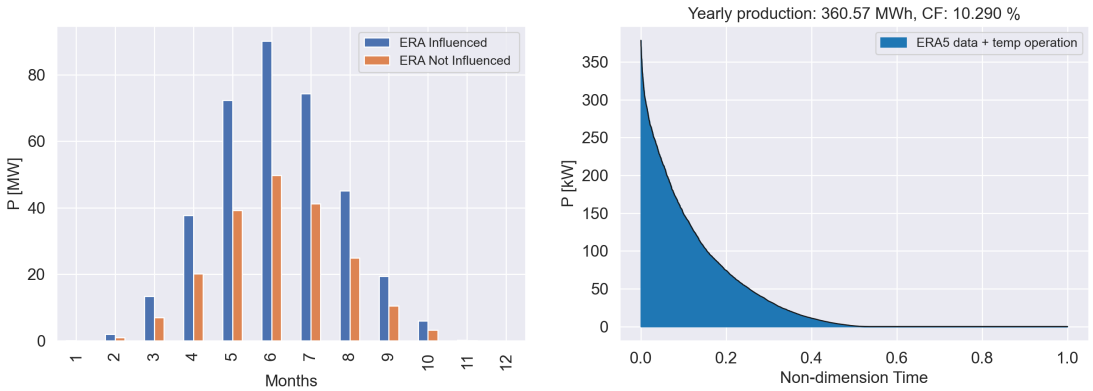

Figure 5.14: Left: 2020 Monthly PV production with the proposed PV configuration 2. Right: A Power duration curve for the PV system conf.2 with hourly resolution, where the filled area is the yearly production. This is given in the figure title and its capacity factor.

5.3 Wind Performance

5.3.1 Analysing Surface Roughness Length

There are three wind turbines proposed in this thesis, and their technical specifications is given in table 5.8. In this section, mainly the 8 MW wind turbine performance will be presented due to its being used in the main network analysis. The proposed area is at a small mountain ridge with a gradual slope nearby Hekkingen lighthouse. It's around 240 m above sea level and has mainly bare rock surface containing some trees nearby. Therefore, was multiple surface roughness length analysed to evaluate the effects.

Table 5.8: The technical specifications for the simulated wind turbines.

Wind turbine	Vestas V168/8000	Enercon E82/3000	Enercon E48/800	**Units**
Rated power	8	3	0.8	**MW**
Hub height	200	84	56	**m**
Cut in wind speed	4	2	3	**m/s**
Rated wind speed	13	17	14	**m/s**
Cut out wind speed	25	25	25	**m/s**
Number of turbines	4	4	4	

The surface roughness length is simulated at 0.1 due to presence of trees, and the effect of it is mentioned in section 2.6.2. Its not varied through the years due to small changes in the surface texture but increased and reduction of surface roughness is analysed. Increment of the surface length yields a higher wind speed at higher altitudes seen in figure 2.14, which again implies a higher production due to it's proportionality to wind speed. The sensitivity analysis of the surface roughness is shown in figure 5.16.

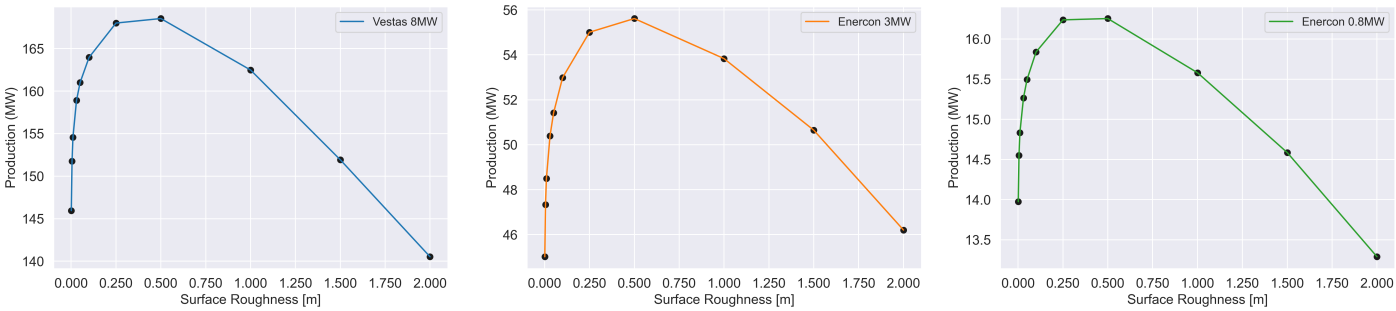

Figure 5.15: Sensitivity of the electric production due to effect of surface roughness.

Table 5.9: Percentage change of yearly production with effect of surface roughness.

Surface Rougness [m]	0.01	0.03	0.05	0.10	0.25	0.5	1.0
Vestas 8MW	-5.74%	-3.08%	-1.80%	0.0 %	2.46%	2.78%	-0.90%
Enercon 3MW	-8.46%	-4.90%	-2.96%	0.0 %	3.82%	4.97%	1.60%
Enercon 0.8MW	-6.35%	-3.60%	-2.15%	0.0 %	2.53%	2.63%	-1.63%

Table 5.9 shows the roughness length affect over 0.5 m at an altitude of 240 m will not increase the wind speed relative to 0.1m. To accurately estimate the correct roughness length, a terrain analysis in high resolution needs to be addressed. This could be done using ArcGIS with satellite data, to estimate and classify the amount of vegetation. This is not done in this thesis, and the AROME-Arctic and ERA5 do not have sufficient resolution to take this into account. The surface terrain could then be coupled to create more accurate wind speed calculations.

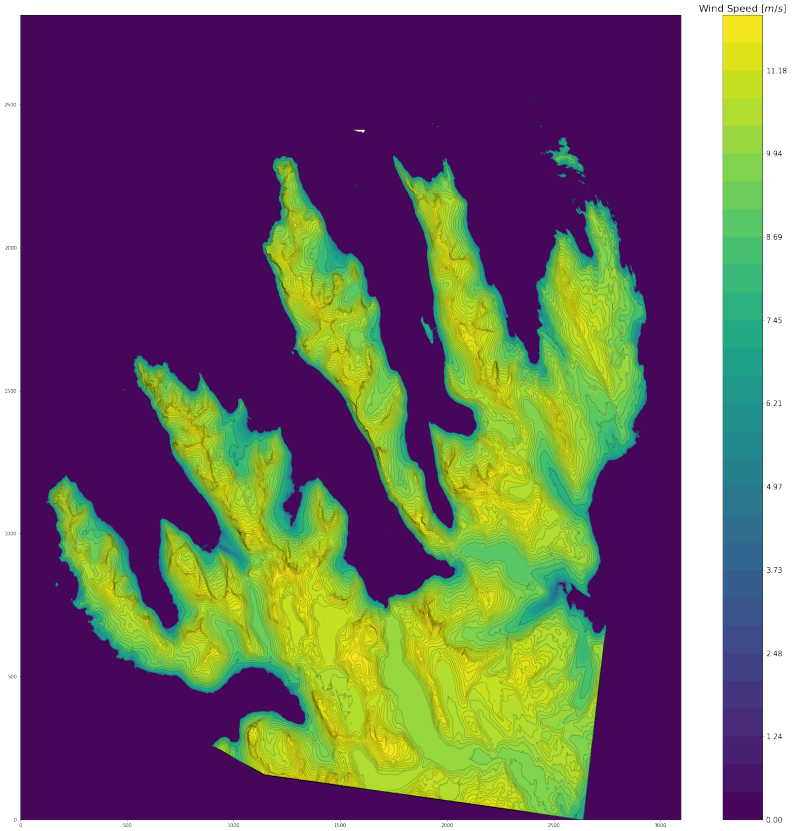

Figure 5.16: A topographic map of northern Senja on how the wind speed changes if measured speed is $v = 6\,m/s$ and the surface roughness length is 0.1 m.

5.3.2 Wind Turbine Output

The technical parameters for the wind turbines are given in table 5.8, where the corresponding power curves is given in figure 5.17.

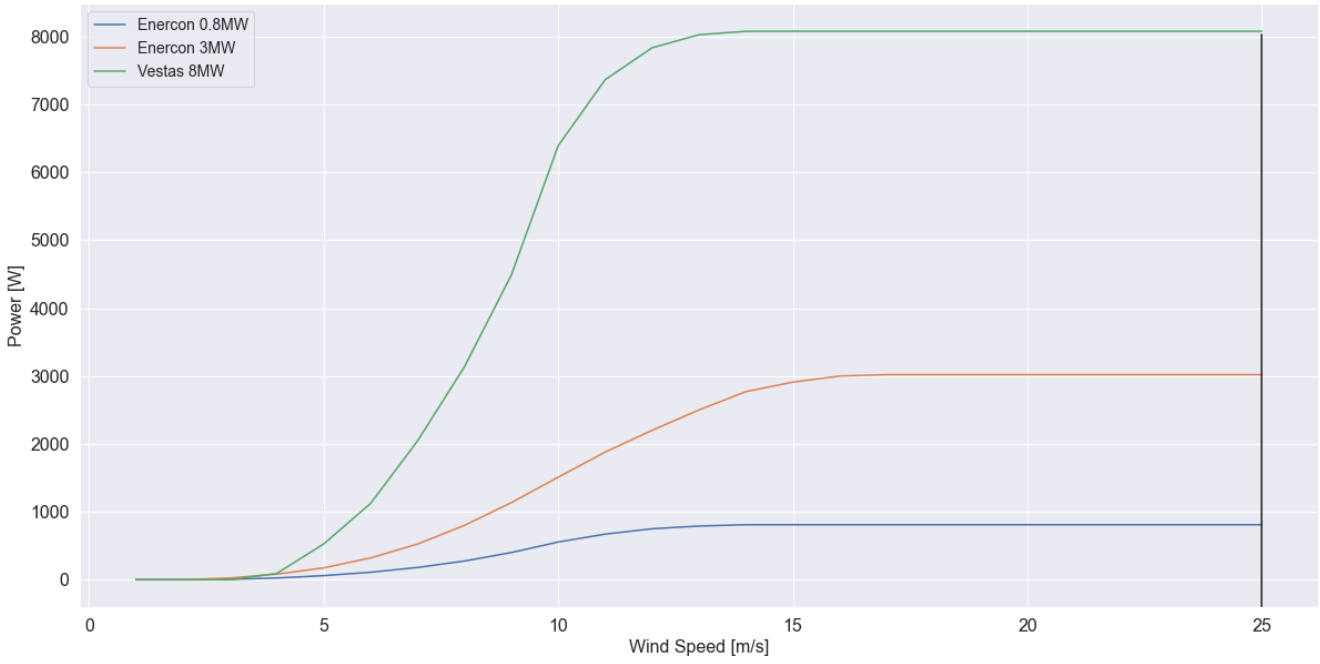

Figure 5.17: The power curves of the different wind turbines

The location is chosen to be nearby the Hekkingen lighthouse, therefore real measurements are used in yearly performance since both AROME-Arctic and ERA5 grid resolution is within area of interest and Hekkingen lighthouse. The performance of the wind systems output is done according to its power curve, setting a turbine loss on 2 % and the roughness length on 0.1 m.

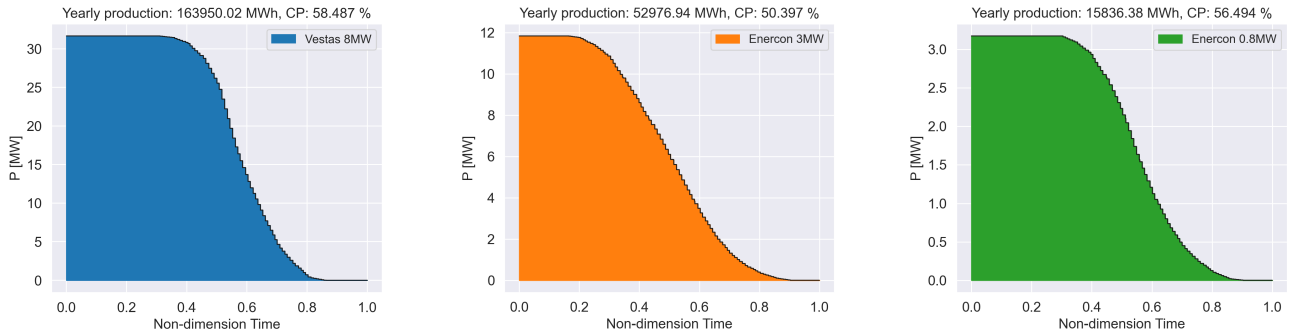

Figure 5.18: Yearly production of 1 wind turbine for the three proposed wind turbines configuration with their capacity factor presented in production versus non-dimensional time in 2020.

The yearly output for wind turbine farm shows great potential for the wind turbines. All three types retrieving a CF $>$ 50 %, which indicates power generation half the year of 2020. The average

onshore wind capacity factor in Europe is 23 % according to [WindEurope, 2022], therefore a performance on double CF is excellent. The calculated CF is most likely overestimated, due to higher loss than 2 %. Losses due to turbulence, wake, optimisation of pitch and stall control will reduce the output. In addition, the wind direction is calculated to always facing the turbine, where jaw control will be needed to adjust the turbine facing direction. The adjustment will have some time delay reducing the hours of power production for the wind turbine. The wind speed data is also given in an average hourly magnitude, where variations during the hours could decrease the steadiness of production. Throughout the year, there are some time periods where the wind speed is steady due to seasonal changes and thus the losses will be associated with wind direction. The daily average wind speed is plotted with wind turbine production in figure 5.19, where some stable periods are visible.

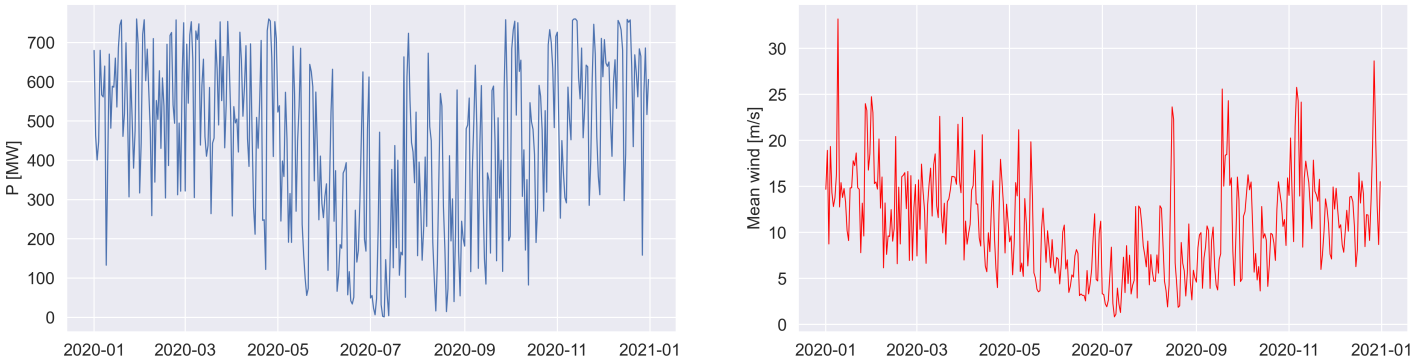

Figure 5.19: Yearly production in 2020 for Vestas 8 MW turbine, where it's given in daily production with average daily wind speed at the left.

Comparing the electrical production with a wind and PV system, its clearly shown to be more stable for wind turbines than PV systems. Production is a lot steadier than PV throughout the year, but seasonal variation will be present. This is an advantage for wind turbine systems and a solution for lack of production, where PV systems are heavily dependent on seasons. To confirm this, the average daily production profile for each quarter is calculated and plotted likewise as figure 5.10. The result is shown on the next page in figure 5.20.

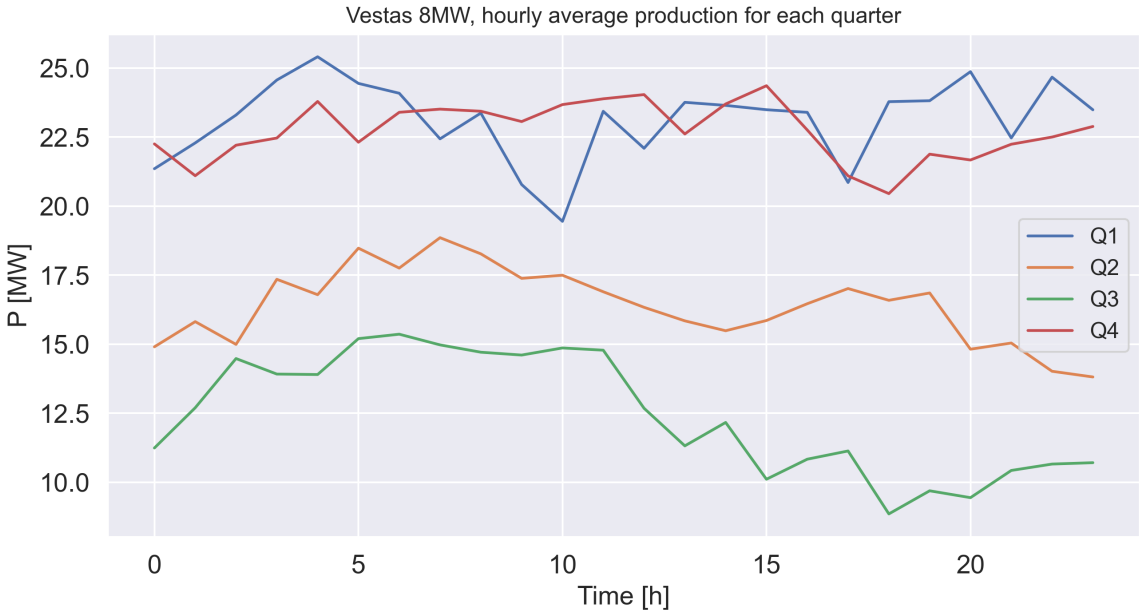

Figure 5.20: The average daily power output for each quarter in 2020. This is for the Vestas 8 MW turbine

5.4 ArcGIS Solar Map

With ArcGIS the solar map is produced to evaluate the best suitable locations for PV. The aspect is also produced to see how its correlated to solar radiation. To view the figures better, zooming is required.

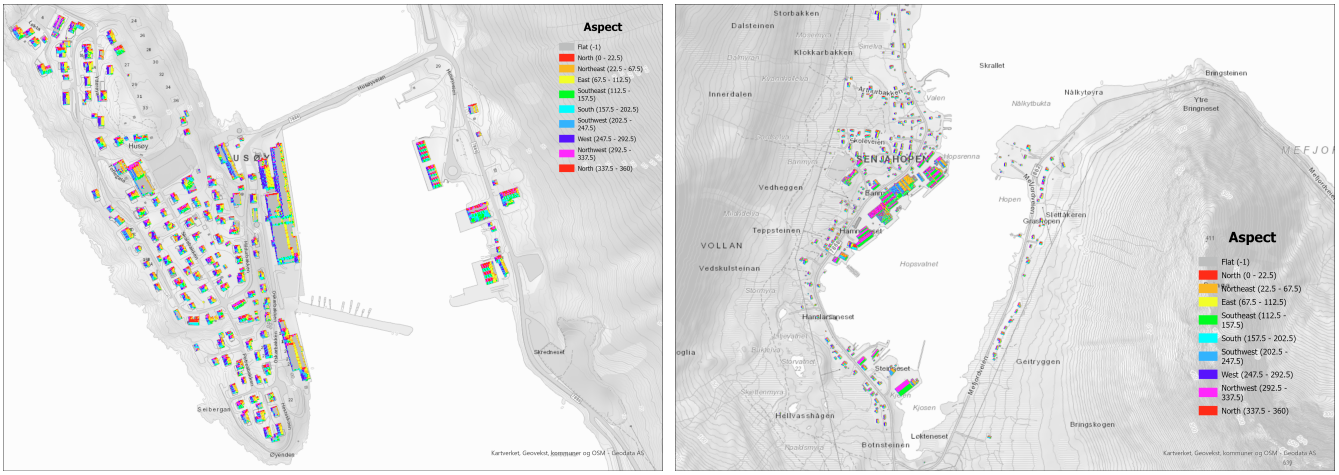

Figure 5.21: The Aspect of the buildings at Husøy and Senjahopen shown using ArcGIS. Left: Husøy, Right: Senjahopen.

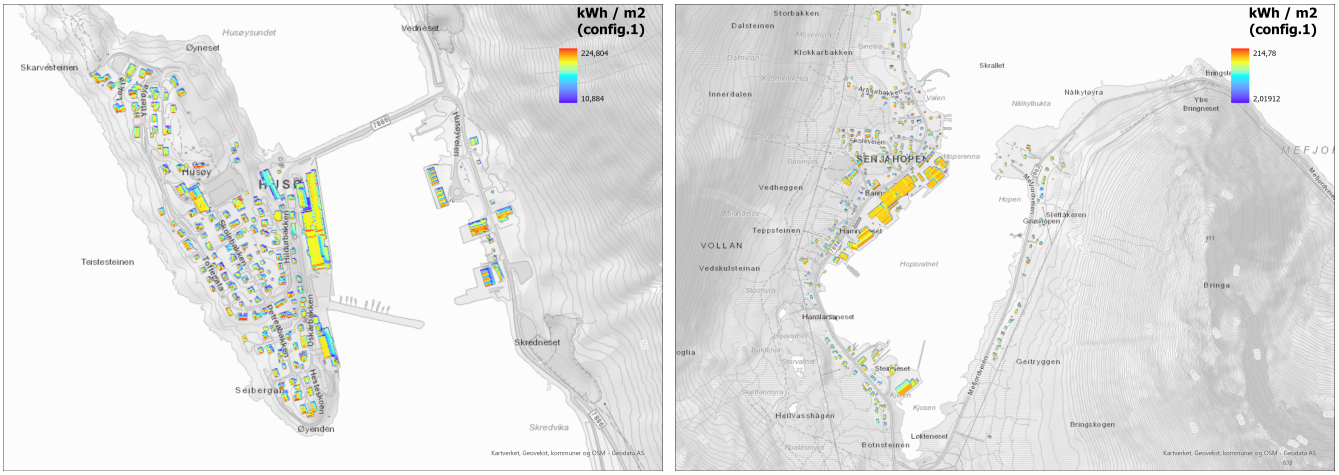

Figure 5.22: The yearly PV production per square meter with configuration 1 on the buildings at Husøy and Senjahopen shown using ArcGIS. Left: Husøy, Right: Senjahopen.

The potential yearly PV production is shown in figure 5.4, where the PV configuration 1 is used. It ranges from around 11 kWh/m^2 to 225 kWh/m^2 for Husøy and 2 kWh/m^2 to 215 kWh/m^2 for Senjahopen. For configuration 2, the values only change slightly. From ArcGIS, the fishery factories seem to have fairly good possibilities to have PV production, where Senjahopen seems slightly better. In addition is the solar map for whole Senja produced where the average yearly solar radiation [Wh/m^2] is given in a $1km \times 1km$ hexagons. It is also filtered to only take the building footprint into account, given in same format as for whole Senja.

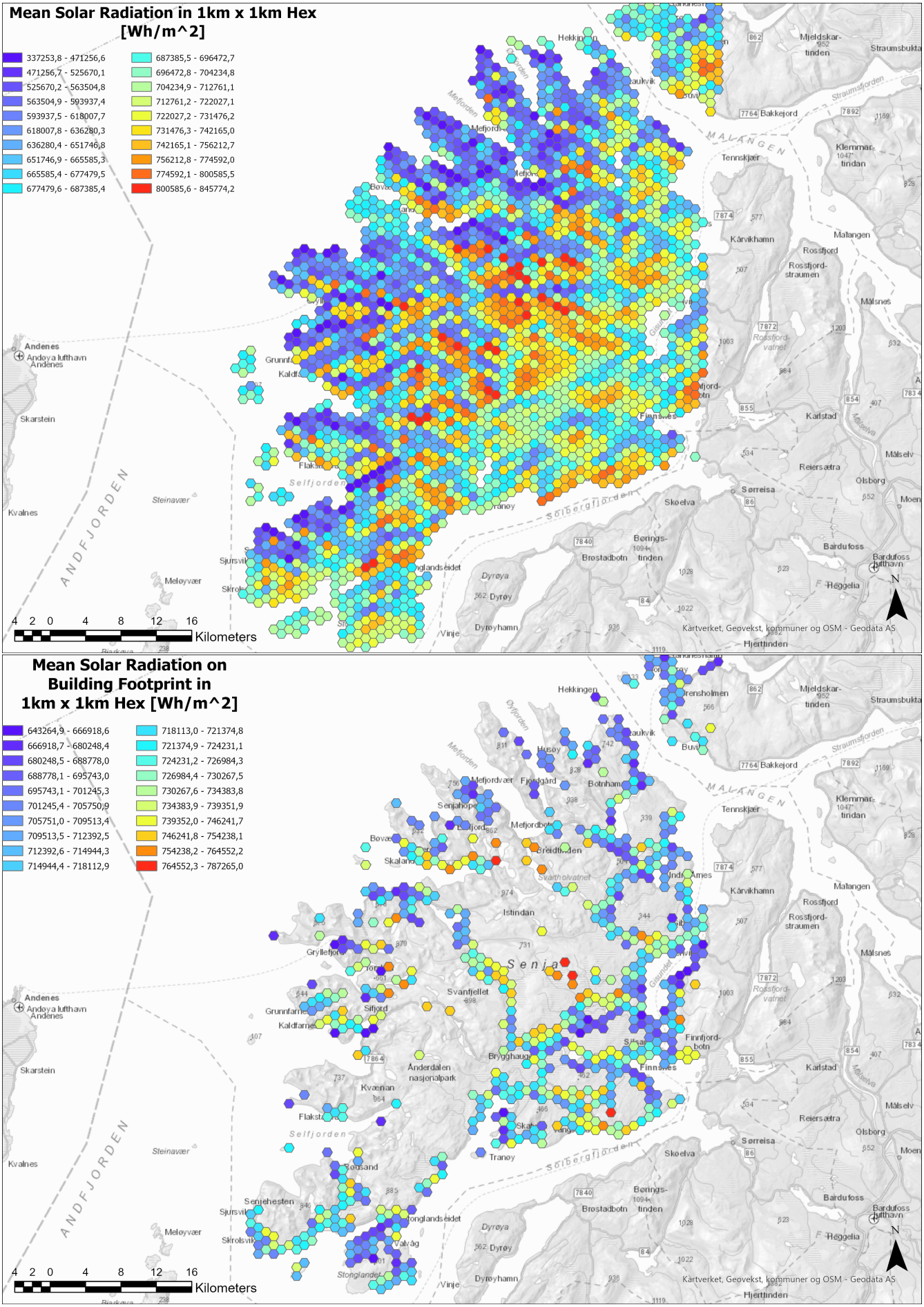

Figure 5.23: The mean yearly solar radiation in $1km \times 1km$ hexagons using ArcGIS.

5.5 Sources of Error for Renewable Power Generation

The simulated potential power output in this thesis has several sources of error which must be considered. Some are already accounted for, but this section is to summarise key factors. The weather data has some uncertainties which is addressed in the statistical analysis. The models data also has a fairly large grid resolution which make local variation hard to model, therefor were it not taken into account.

Only hourly PV production is simulated, where the quarterly hour PV cell production from Husøy has higher peaks and higher production. The daily variation has large impact, which is seen at the production during the winter months. Some hours of sunlight, high reflections and large module tilt gives a extends the PV production period throughout the year. The impact reflection with albedo is not considered, which makes the estimation under predicting during winter months. In addition to the albedo, the impact of snow covering PV modules is also not simulated. The figures for snowfall and snow depth are given in the appendix A.3.

In the wind power simulation, effect not taken into account is already mentioned. Wake and turbulence are not quantified at the location and introduces a level of uncertainties. Losses due to the mechanical system, jaw operation is ignored. Therefore, the wind direction losses is neglected and the surface roughness length losses.

6 / Network Analysis

6.1 Overview

It is observed that the simulated model does not achieve the same magnitude as the voltage variations measured at Husøy. The measured voltage is the average voltage of the three-line voltages. The illustration of the simulated model is shown in figure 6.6, where the measured voltage profiles and simulated voltage profiles based on measured voltage is plotted. The data is given in an hourly format (1 hour = 1 time step) over 8 days, where the start and end period is given in section 4.5.2. The model is moderately able to simulate the voltage profile pattern but misses 10-20 % of the voltage magnitude.

The deviation between the measured and simulated values might be a cause of multiple reasons. Reasons can be of inaccuracy of line lengths, conducting material or other parameters regarding the network. Due to lack of information about the exact parameters, the standard library in PandaPower was used, and some parameters were tweaked. The electrical production could have been able to produce more, or the transmissions lines has got an upgrade, resulting in better voltage. Other reasons might be by setting limitations and assumptions, especially assumption about the balanced system and simplifying the network. However, by simulating injection of high penetrating renewable energy sources, decisions making on purchase and installation might be easier.

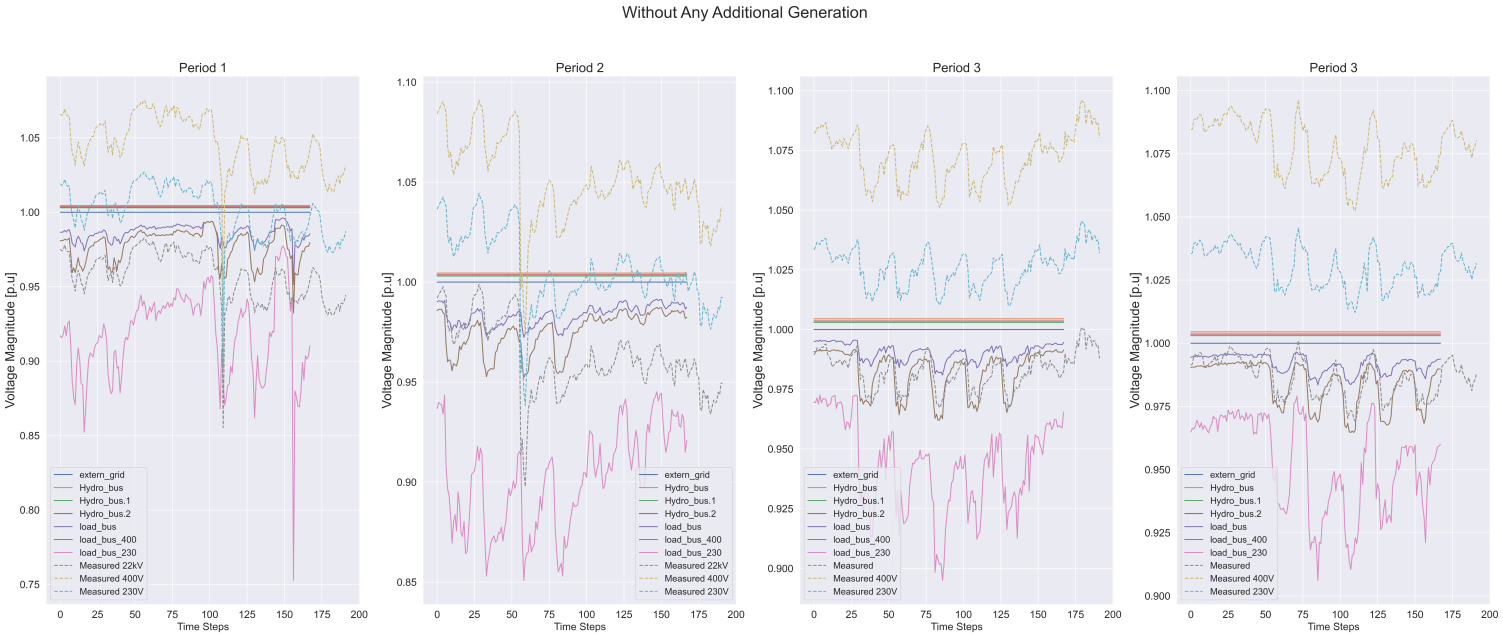

Figure 6.1: Simulated voltage profiles at Husøy in the periods given in section 4.5.2. The simulated voltage profile is compared against the average of voltage lines.

6.2 BESS

The parameters used is listed in the table 6.1, where the values are taken from the installed batteries at Husøy. The data sheet for the battery is given in the appendix A.4.6.

Name	Capacity [kWh]	P_{max} [kW]	SOC_min [%]	η [%]
Energypack QL	2373	2582	20	90

Table 6.1: The parameters used in the proposed algorithm to calculate the shaved loads.

From the highest overall improvement of the voltage magnitude, the simulation of the BESS is given in figure 6.2. The results shows that BESS gives a steadier flow of power, where the voltage variations vary less, and load peaks are substantially reduced. The simulation is limited to the assumption of no frequent switching control. The simulation is most likely underperforming due to dispatching power from the battery during low load periods. These periods could be supplied by hydro, PV or power from wind turbine and excess energy recharges the BESS. The peak shaving is reduces the high peaks quite substantially and will also be able to deliver reactive power for phase correction. If peak shaving is the best or most suitable application for BESS is debatable.

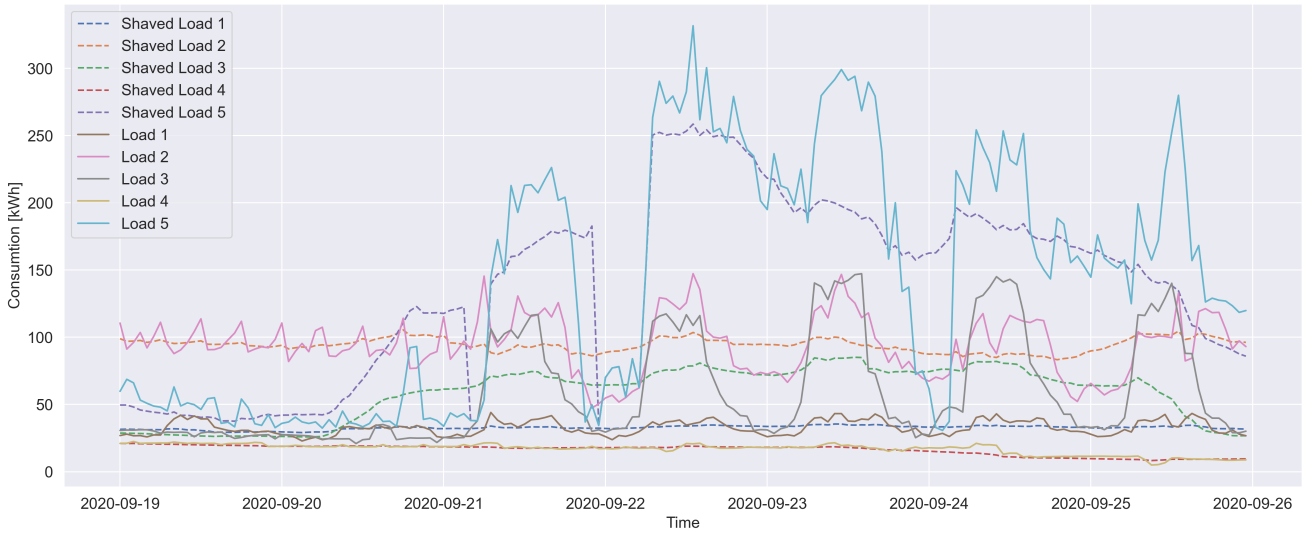

Figure 6.2: The loads from Husøy shaved with BESS in the second period (ref. section 4.5.2).

	Peak Load [kW]					Peak Load shaved [kW]				
Loads	1	2	3	4	5	1	2	3	4	5
Period 1	120.0	405.5	154.3	53.6	665.6	58.2	271.8	92.4	49.0	294.3
Period 2	55.0	416.4	152.6	39.5	368.5	46.3	357.8	94.7	29.0	262.4
Period 3	40.3	311.0	148.7	25.8	278.8	20.2	260.8	84.9	21.7	199.1
Period 4	44.0	147.3	147.2	22.4	331.0	35.5	105.4	85.1	21.0	258.5

Table 6.2: The peak load shaved from the different loads and time periods.

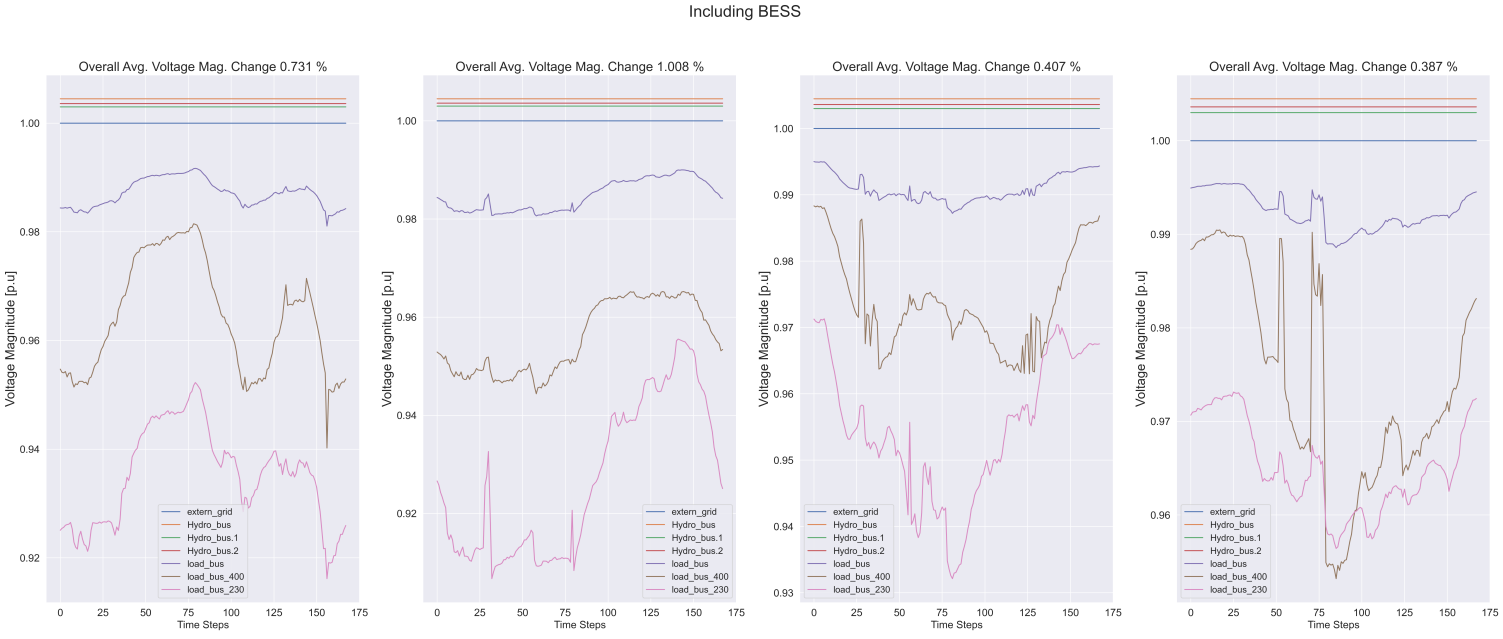

Figure 6.3: Simulated voltage profiles with injection of BESS at Husøy in the periods given in section 4.5.2.

6.3 BESS + PV

The PV system is placed at the rooftops for the local industry. In figure 6.4 the *load_bus_230* perfectly correlates with *pv_bus*, therefore the pink line is not visible. The PV system work very well in combination with the BESS. The loads are adopted from the from the BESS using peak shaving. The system is able to rise the voltage level for the low voltage busses, giving them less variation and closer to the desired voltage level. The best PV production is as expected, which is during the second period. The overall voltage is raised with 3.5 % and rarely drops under 0.94 p.u.

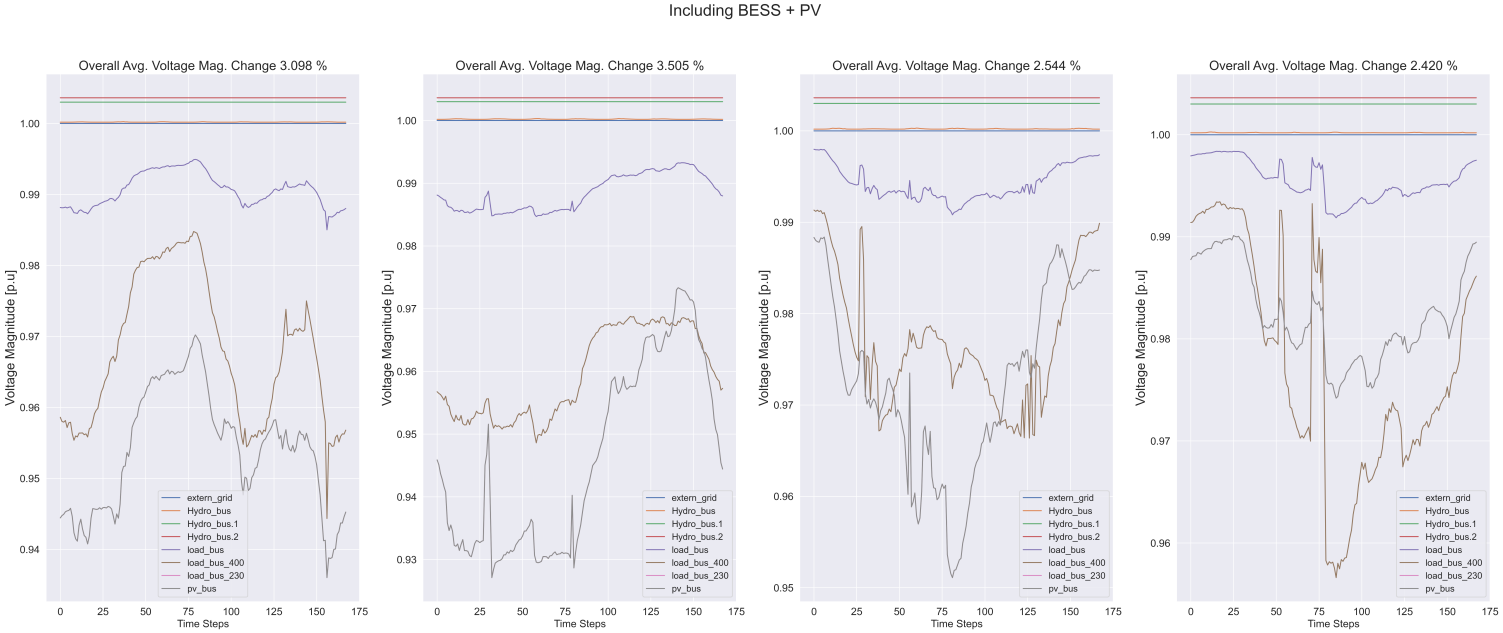

Figure 6.4: Simulated voltage profiles at Husøy in the periods given in section 4.5.2. The simulated voltage profile is compared against the average of voltage lines.

6.4 BESS + WIND

A combination of the BESS and wind turbine system would improve the voltage at the 22 kV distribution. The loads are mainly adopted from the BESS using peak shaving, creating smaller variations than today's network. By adding wind turbines gives a higher level of voltage, but the low voltage buses are shifted slightly to a lower p.u. There is possibly a sum of several reasons for the slight shift, but one reason might be the voltage variation. The high voltage bus with the hydro power connected with the plant and the wind park variate voltage due to the wind power production. As seen in figure 6.5, the highest increase in voltage magnitude is during period 2, and the wind power production is steady and sustain a lot of power.

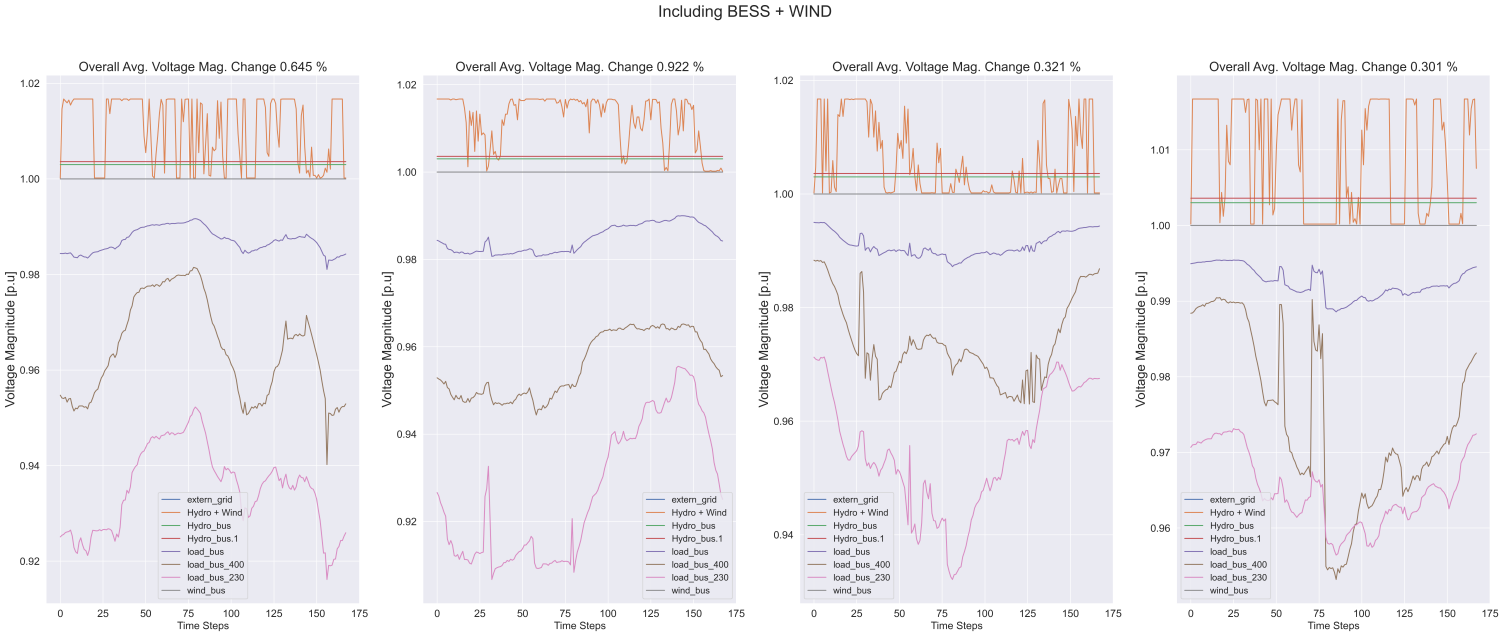

Figure 6.5: Simulated voltage profiles at Husøy with wind power injection and BESS in the periods given in section 4.5.2. The overall voltage increasement is given in the plot title.

6.5 BESS + PV + WIND

By injecting multiple renewable energy sources into the network, the overall voltage increasement is good for all four periods. The highest voltage increasement is during period 2, due to high production from wind turbines and PV. For the electrical consumers, the system is a lot steadier compared to no injection. The magnitude of the load voltage drops is severely reduced and drops less frequent under 0.96 p.u. This system consists of a injection from a wind farm located some kilometre away, 500 PV modules and is connected to the BESS.

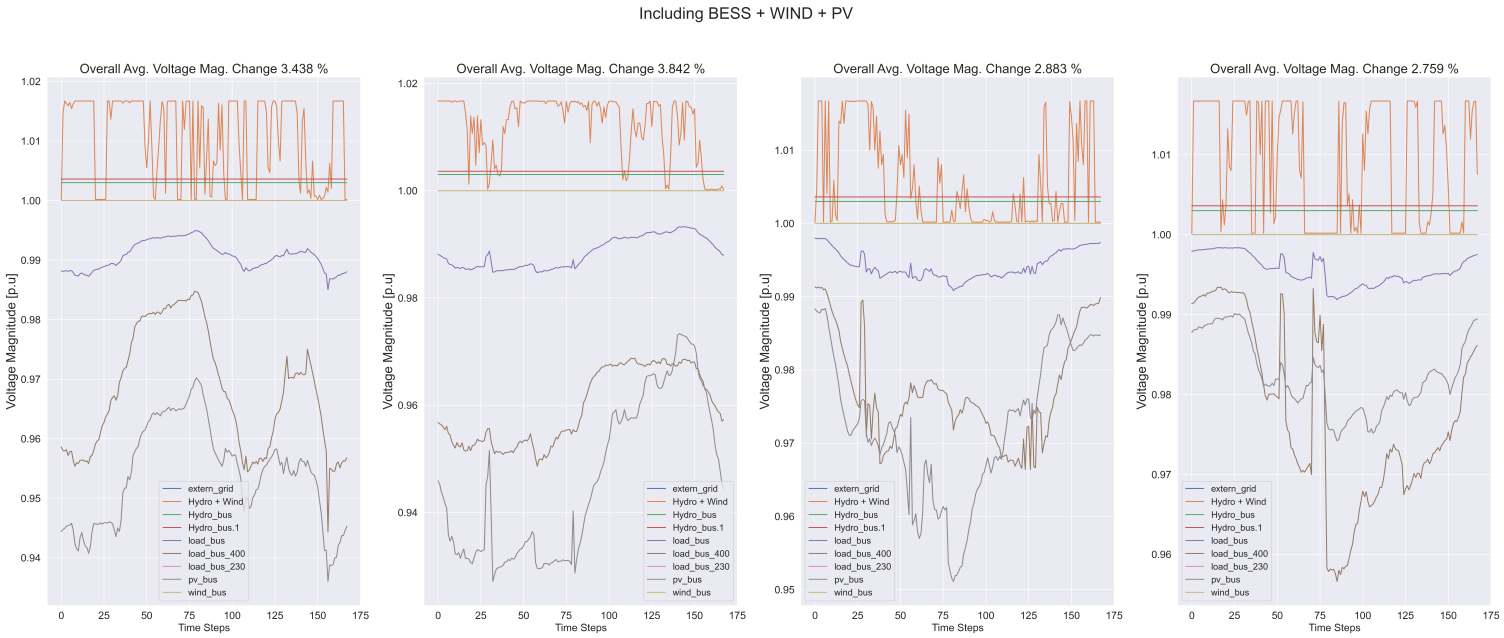

Figure 6.6: Simulated voltage profiles at Husøy in the periods given in section 4.5.2. The simulated voltage profile is compared against the average of voltage lines.

7 Conclusion and Further Work

7.1 Summary

In this thesis, this study the potential renewable energy production with power flow control on power system at the northern part of Senja, Norway. Simulating an industrial scale PV system at the local fishery industry and a small wind farm to quantify the potential yield. A network analysis was performed to evaluate the impact of renewable energy systems. In addition, a BESS is added to the distribution network and quantified by released transfer capacity.

The PV system was set with a southwards orientation and tilted 50°, because it's the optimal orientation for the industrial building, increase the installed capacity and energy yield. The best monthly electrical production is in May, giving a 65.72 MWh and a capacity factor on 13.3 %. The result is promising for the the summer months and can provide sufficient power during low season in fisheries. The first and last quarter have a small impact on compared to the consumption. The PV system combined with BESS will give the most value to supply voltage support with an overall increase at best 3.5 %.

The wind farm had an installed capacity on 32 MW and had a yearly output on 163.95 GWh with a capacity factor on 58.5 %. This gives a daily average on 448 MWh. This is an excellent location and the capacity factor is the double of the European average. The yearly variation of wind speed is most stable at the winter, which is found to correlate well with combination of PV. In addition is the highest output during wintertime, which correlates with the load peaks. Effect as turbulence and wake losses are not included in the initial simulations, which gives an over-estimation on the output. The production is initially high and a with the losses, a capacity factor above 40 % is still obtainable.

The network was simulated for the different system configuration, where BESS is included in all simulations. The highest network improvement is adding BESS, PV, and a wind farm. This

increases the voltage magnitude on from 2.75-3.84 % where quarter two and three gets the highest voltage magnitude. The network is simplified and limited to reduce process and development time, where some uncertainties are removed through assumptions. However, the simulation all over is improved by adding any form of new energy sources or control strategies with BESS.

7.2 Concluding Remarks

The main objective of this thesis was to evaluate the effect of injecting renewable energy resources into the distribution grid and the effect power flow control performance. This was done by quantifying the yearly potential and power flow with simulations. The result for Senja shows great potential for harvesting wind resources, and solar resources show potential during the summer months. The effect of the components regarding the network performance is overall positive. Its ability to improve voltage regulation, reduce losses and improve all over stability and power quality. The new improvement will enable the network to operate acceptable, also with new additional peak load patterns. The control during peak load should however be supported with hydro plants and optimal control strategies for BESS.

Even with enforcement of realising transfer capacity, the renewable energy sources will not be sufficient to relive the 66 kV distribution network for new factory loads. Without the hydro power plant, new additional energy sources will not be sufficient, and lines will still be overloaded. Wind farms are the most optimal production source to enforcement, but the wind viability enforces to sill rely on hydro power plants. The increasing power demand trend makes upgrading the transmission lines become a necessary. The simulation of the distribution network shows some promise of postponing investments in transmission capacity, but the investment must be done in the near future.

7.3 Further Work

In order to confine the scope, economic analysis and systems is not considered. In future work, this should be assessed in order to determine if renewable systems are feasible. The systems cost needs to be evaluated with respect to its generated energy through the systems lifetime. An economic analysis on the implementation of BESS system, a net present value and the savings due to reduced cost for transmission line investments. Including should multiple load control strategies of the BESS should be implemented, where an economic analysis is considered for storing energy. The economical study will assure if these systems is feasible compared to investing in convectional transmission line investments.

The smart power system at Senja should also consider large, interconnected power system and other large scale renewable sources. The interaction between all components the power infrastructure should also be simulated and analysed. By developing complex smart models of the infrastructure and simulate with respect to external factors will give a better result. The assimilated data need to be correlate and cooperate to optimise performance for the control systems used in the network. The components should be implemented in an operational regime, forming an interactive control on the network operation. In addition to the large-scale systems, one should use results like the solar map in this thesis to addressee PV and BESS at residences and cabins at Senja.

Lastly, the active monitoring of the distribution is important and will continue to be an important feature in the developing power system technology. Further study regarding the topic discussed in this thesis and this section will regardless help understanding and improve the technological advancements. Conclusively, a shift toward sustainable and green energy is necessary, improving the efficiencies in energy infrastructure will benefit towards a sustainable and green future.

A / Extra

A.1 Distribution of Wind Speed at Hekkingen

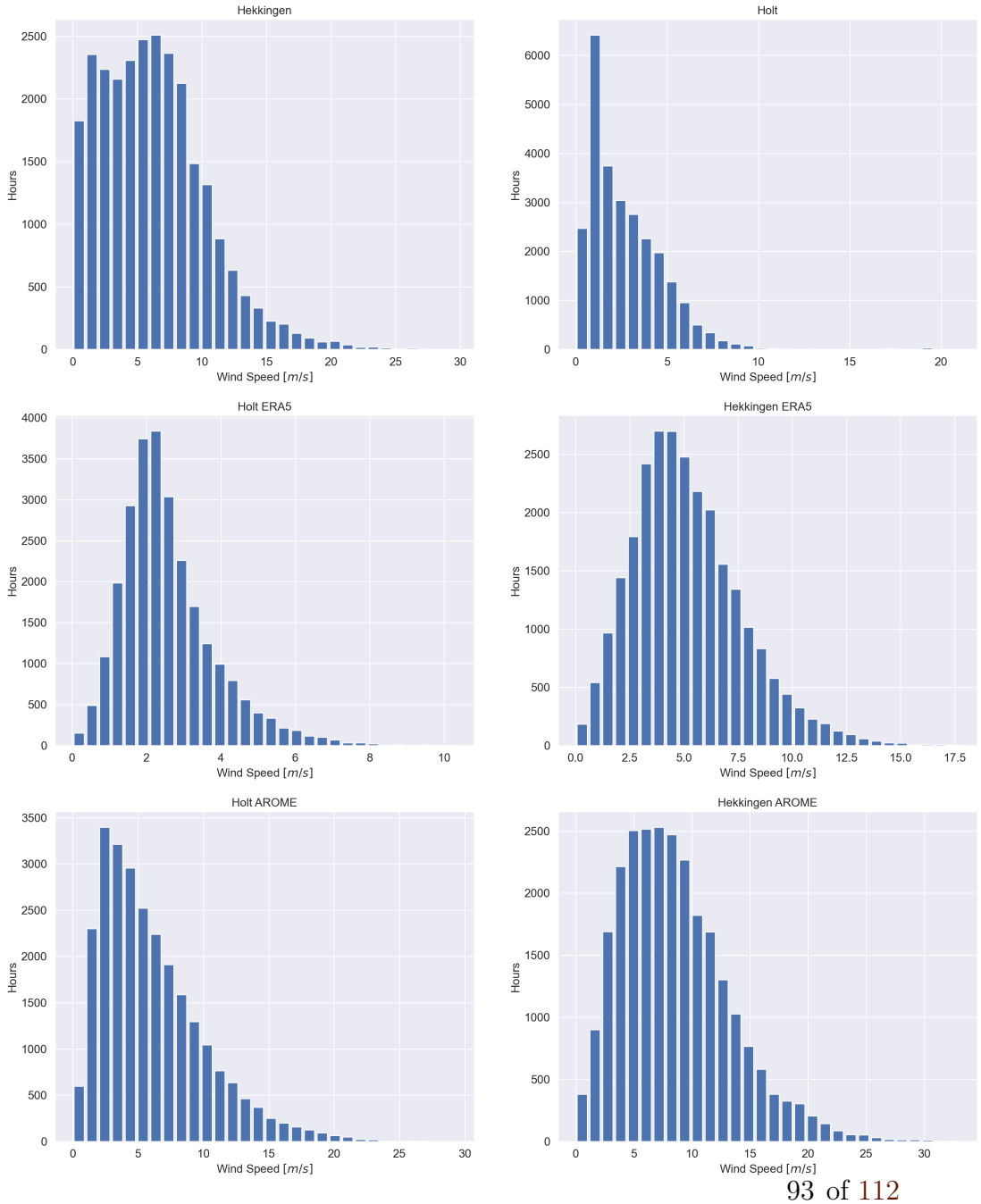

A.2 Data collection figure

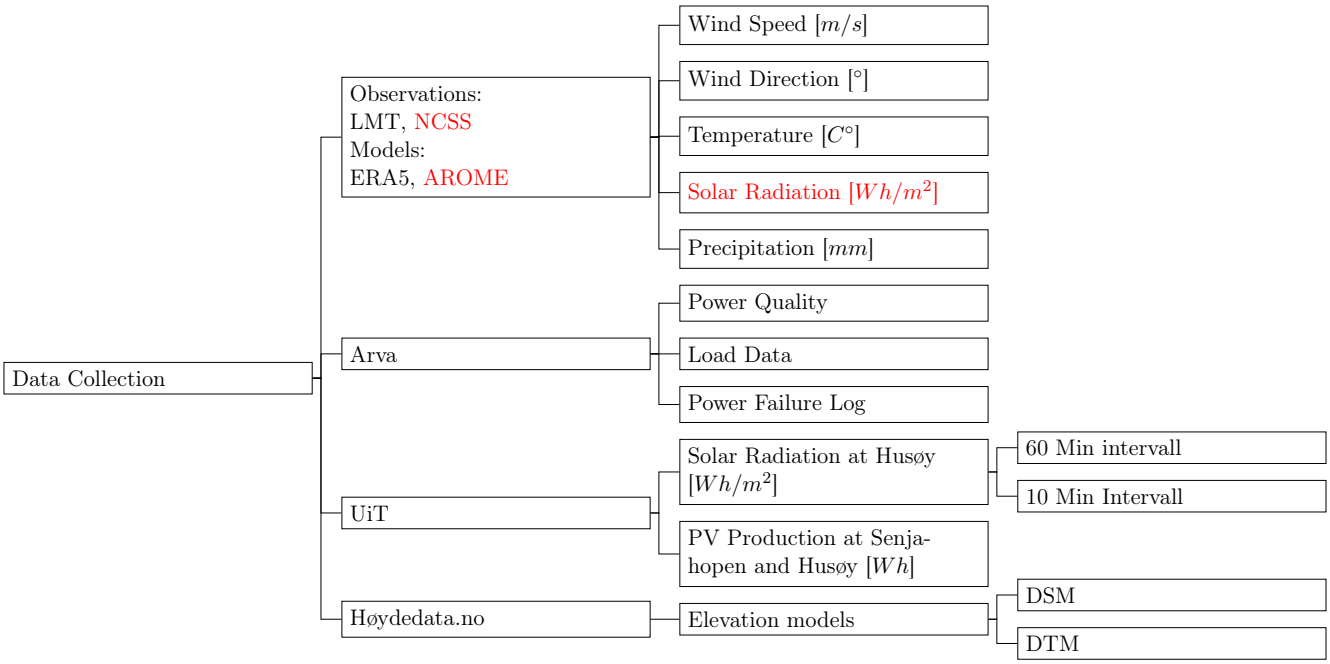

Figure A.2: An overview of the data collected in order to perform the simulations executed in this thesis. The red colour indicates parameters which is not included in the data set. The data was primarily collected from 2019-2021.

A.3 Snow depth and fall

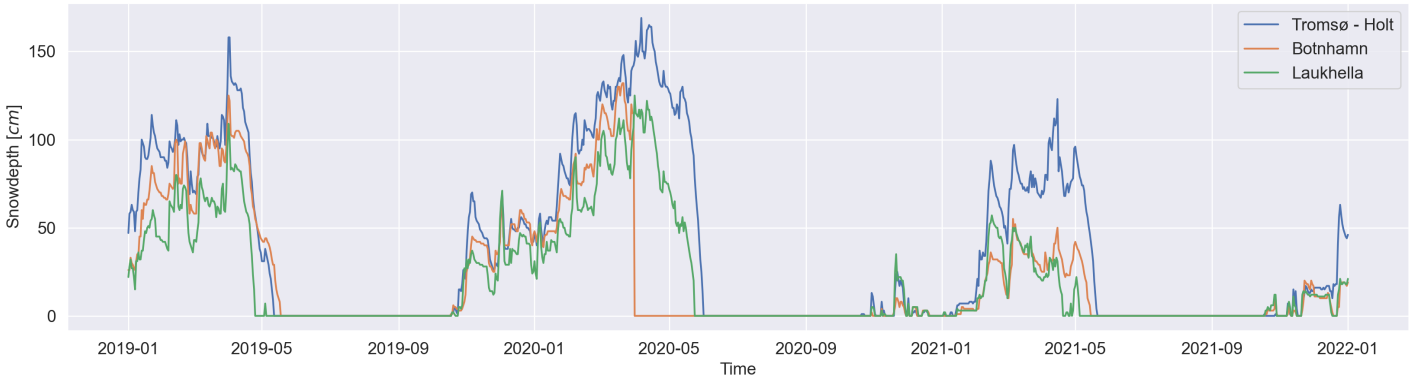

Figure A.3: Snow depth measurements from Senja and Holt from 2019 to 2022.

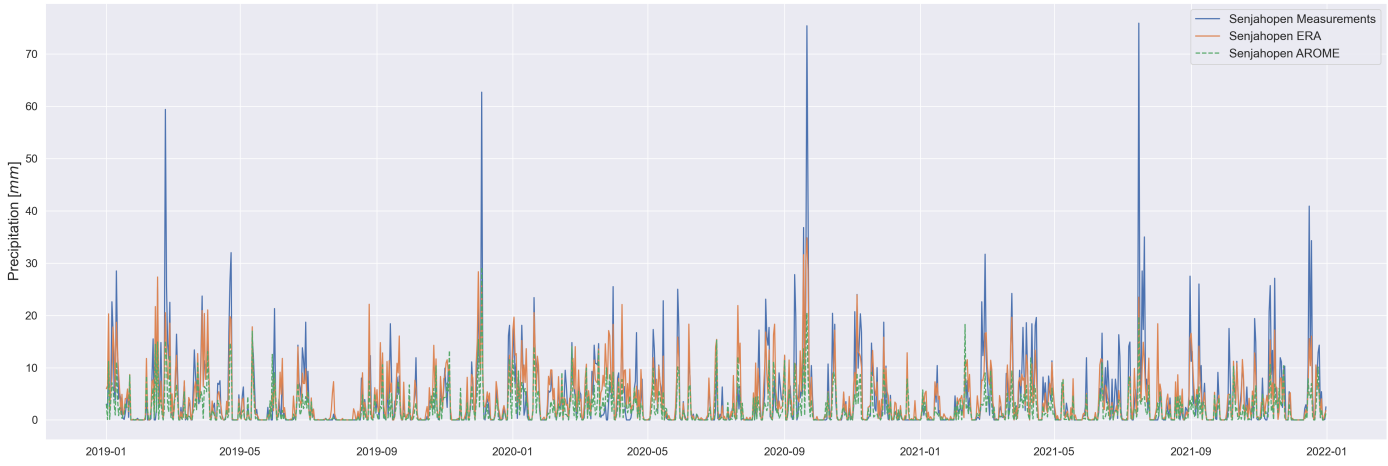

Figure A.4: Precipitation measurements with observed measurements at Senjahopen and modelled data from 2019 to 2022.

A.4 Additional Equations and Figures

A.4.1 PV cell Temp

By taking the energy balance of a PV cell, the cell temperature T_c can be expressed as:

$$T_c = T_a + G_T(\frac{\tau\alpha}{U_L})(1 - \frac{\eta_c}{\tau\alpha}) \tag{A.1}$$

Where τ is the solar transmittance covering the PV array [%], α is the solar absorptance of PV array [%]. The solar radiation at the PV array is G_T $[kW/m^2]$, η_c is the efficiecy of electrical conversation of the PV array [%], U_L $[kW/m^{2\circ}C]$ is the heat transfer coefficient to surroundings and T_a is the ambient temperature $[^\circ C]$. The expression $\frac{\tau\alpha}{U_L}$ is often given from the manufactures in terms of $NOCT$, and is expressed as:

$$\frac{\tau\alpha}{U_L} = \frac{T_{c,NOCT} - T_{a,NOCT}}{G_{T,NOCT}} \tag{A.2}$$

The values are defined as $T_{c,NOCT}$: nominal operating cell temperature $[^\circ C]$, $T_{a,NOCT} = 20\ ^\circ C$ and $G_{T,NOCT} = 0.8\ kW/m^2$. If the cells operate at its maximum power point:

$$\eta_c = \eta_{mp} \tag{A.3}$$

This means the cell temperature is given as:

$$T_c = T_a + G_T(\frac{T_{c,NOCT} - T_{a,NOCT}}{G_{T,NOCT}})(1 - \frac{\eta_{mp}}{\tau\alpha}) \tag{A.4}$$

Assumed values is $\alpha = 0.9$ and $\tau = 0.95$. The efficiency is also dependent on the cell temperature, and can therefore be expressed as:

$$\eta_{mp} = \eta_{mp,STC}\left[1 + \alpha_p(T_c - T_{c,STC})\right] \tag{A.5}$$

Where $\eta_{mp,STC}$ is the PV cells efficiency under the Standard Test Conditions. By substituting the $\eta_{mp,STC}$ with η_{mp} in A.4. The final expression is given as:

$$T_c = \frac{T_a + (T_{c,NOCT} - T_{a,NOCT})\left(\frac{G_T}{G_{T,NOCT}}\right)\left[1 - \frac{\eta_{mp,STC}(1-\alpha_p T_{c,STC})}{\tau\alpha}\right]}{a + (T_{c,NOCT} - T_{a,NOCT})\left(\frac{G_T}{G_{T,NOCT}}\right)\left(\frac{\alpha_p\eta_{mp,STC}}{\tau\alpha}\right)} \tag{A.6}$$

A.4.2 Sky Diffusion Factor

In the calculation of the direct beam radiation, the horizontal diffuse radiation I_{DH} can be be expressed as $I_B C$, where C is given as [Masters, 2013]:

$$C = 0.0095 + 0.04\sin\left[\frac{360}{365}(n - 100)\right] \tag{A.7}$$

A.4.3 Equation of Time (EoT)

It's an empirical equation which corrects the eccentricity of the relation of the Earth's orbit and the Earth's axial tilt [Honsberg and Bowden, 2019].

$$EoT = 9.87\sin 2B - 7.53\cos B - 1.5\sin B \tag{A.8}$$

where B is given as $B = \frac{360}{365}(d - 81)$ in degrees [°] and d is the day number.
The net time correction factor considers the variations of Local Solar Time in a specific zone due to longitude. Additionally, its incorporates with the EoT giving an expression [Honsberg and Bowden, 2019]:

$$TC = 4\,(Longitude - LSTM) + EoT \tag{A.9}$$

A.4.4 Geometry of solar Radiation on a tilted surface

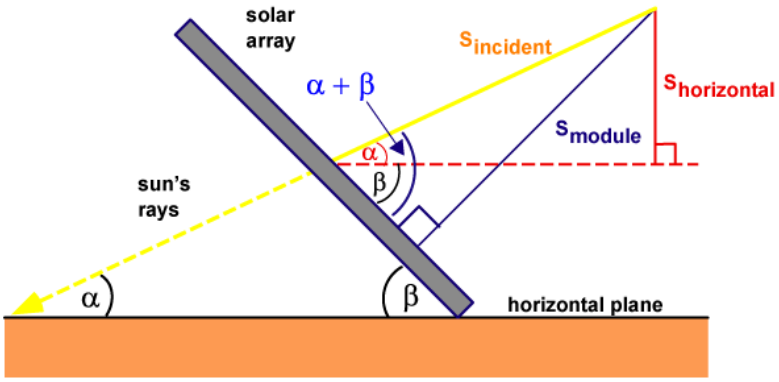

Figure A.5: The geometrical properties of a PV module tilted relative to the horizontal plane. [Honsberg and Bowden, 2019]

A.4.5 Surface Roughness at Senja.

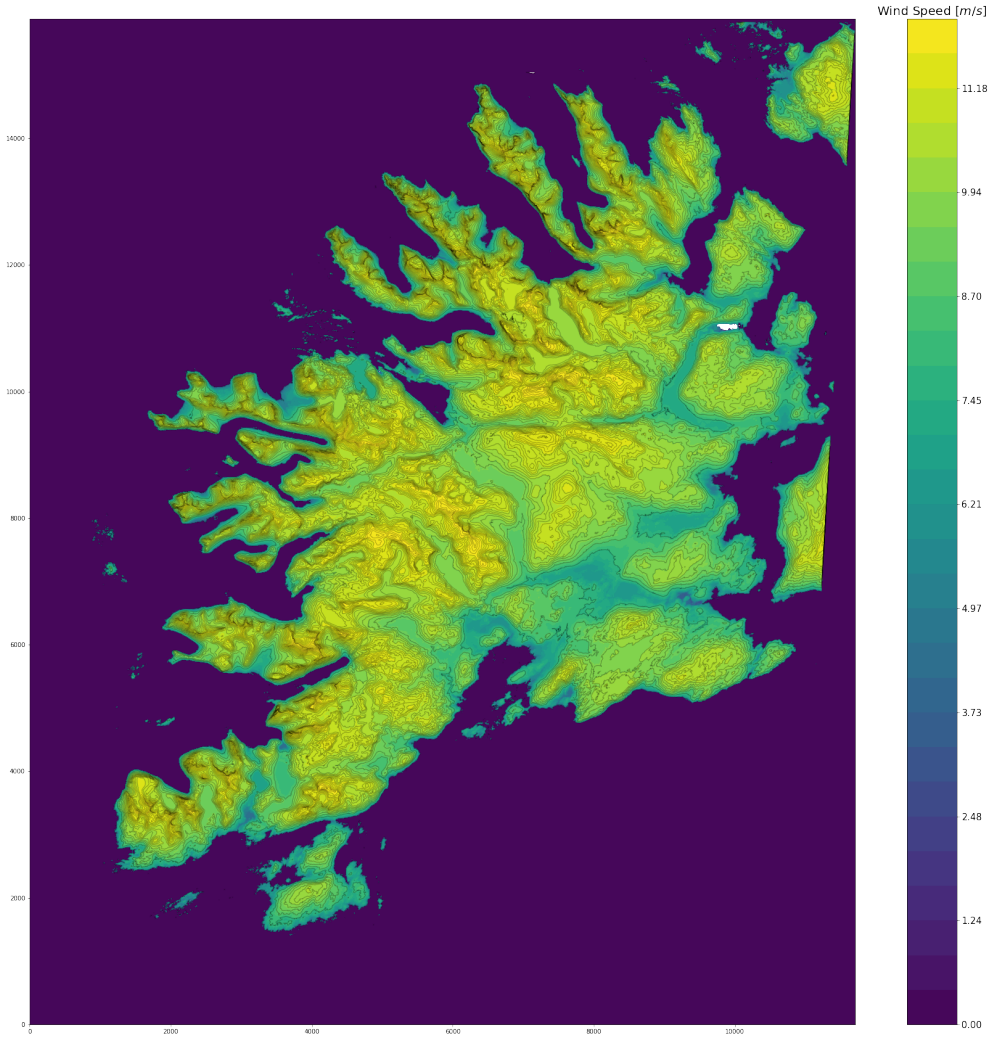

Figure A.6: A topographic map of Senja on how the wind speed changes if measured speed is v = 6 m/s and the surface roughness length is 0.1 m.

A.4.6 Battery Technical Data

Technical data - ***mtu*** EnergyPack QM / QL [1, 2]

Sections	Value	Sign	Unit	*mtu* EnergyPack QM / QL
Battery	Cell chemistry			NCM
	Nominal capacity QM / QL		kWh	up to 800 / up to 2,200
Cooling	Max. ambient temperature	T_{max}	°C	40 (50° C)
	Min. ambient temperature	T_{min}	°C	-20
Electrical	Nominal apparent power QM / QL	S_{nom}	kVA	up to 800 / up to 2,000
	AC short circuit capability		kA	50
	Grid frequency	f	Hz	50 (60)
	Max apparent power (1 min)	S_{peak}	%	110% (150%) of S_{nom}
	Nominal voltage	U_{nom}	V	515 V (400 V with internal transformer) [3]
	Power factor range	cos ϕ		0 ind. ..1 .. 0 cap
	Black start capability			yes
Housing	Corrosion protection			C3 (C5M)
	Height	H	mm	2,896
	Length QM / QL	L	mm	6,058 / 12,192
	Width	W	mm	2,438
	Protection class battery room			IP56
Interface	Supported communication protocol			Modbus-IP (Modbus-RTU, IEC 60870-5-104, IEC 61850, DNP3)
	Supported communication channels			3G / 4G 100MB/s CAT 5
System	Humidity	ϕ_{rel}	%	100% condensing
	Max. operation altitude	H_{max}	m	2,000
	Nominal round trip efficiency [4] (w/o HVAC)			up to 90%
	Weight	m	kg	up to 38,000

Figure A.7: The technical data for the BESS sytem used in this thesis [Royce, 2021].

B ArcGIS

B.1 Raster and Shapefile

A raster consists of a matrix of cells/pixels organised in a grid where all cells have value representing a form of information. Rasters are often digital aerial photographs, imagery from satellites, digital pictures, or scanned maps [Esri, 2022].

A shapefile is a simple, non-topological format for storing geometric location and attribute information of geographic features. Geographic features in shapefiles can be represented as points, lines, or polygons (regions). Workspaces that contain shapefiles can also contain dBASE tables that can store additional attributes that can be associated with the shapefile's features [Esri, 2022].

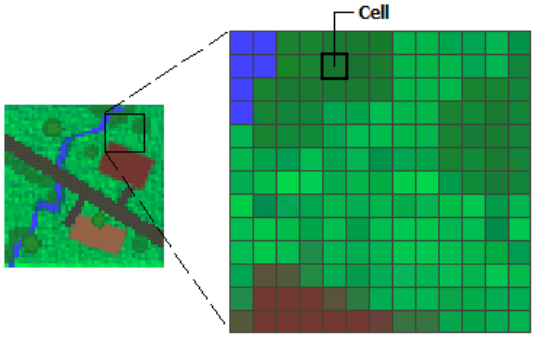

Figure B.1: A illustration of a raster containing data in a grid format. The figure is from https://desktop.arcgis.com/en/arcmap/latest/manage-data/raster-and-images/what-is-raster-data.htm

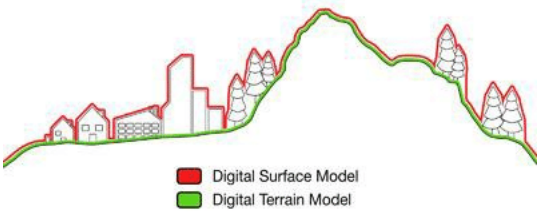

Figure B.2: An illustration on the difference between DSM and DTM [Wikantika, 2018].

B.2 Radiation at Senja

The radiation calculation using *Area Solar Radiation* in ArcGIS. The close up on Husøy and Senjahopen has a resolution on $1m \times 1m$ and Senja has $5m \times 5m$.

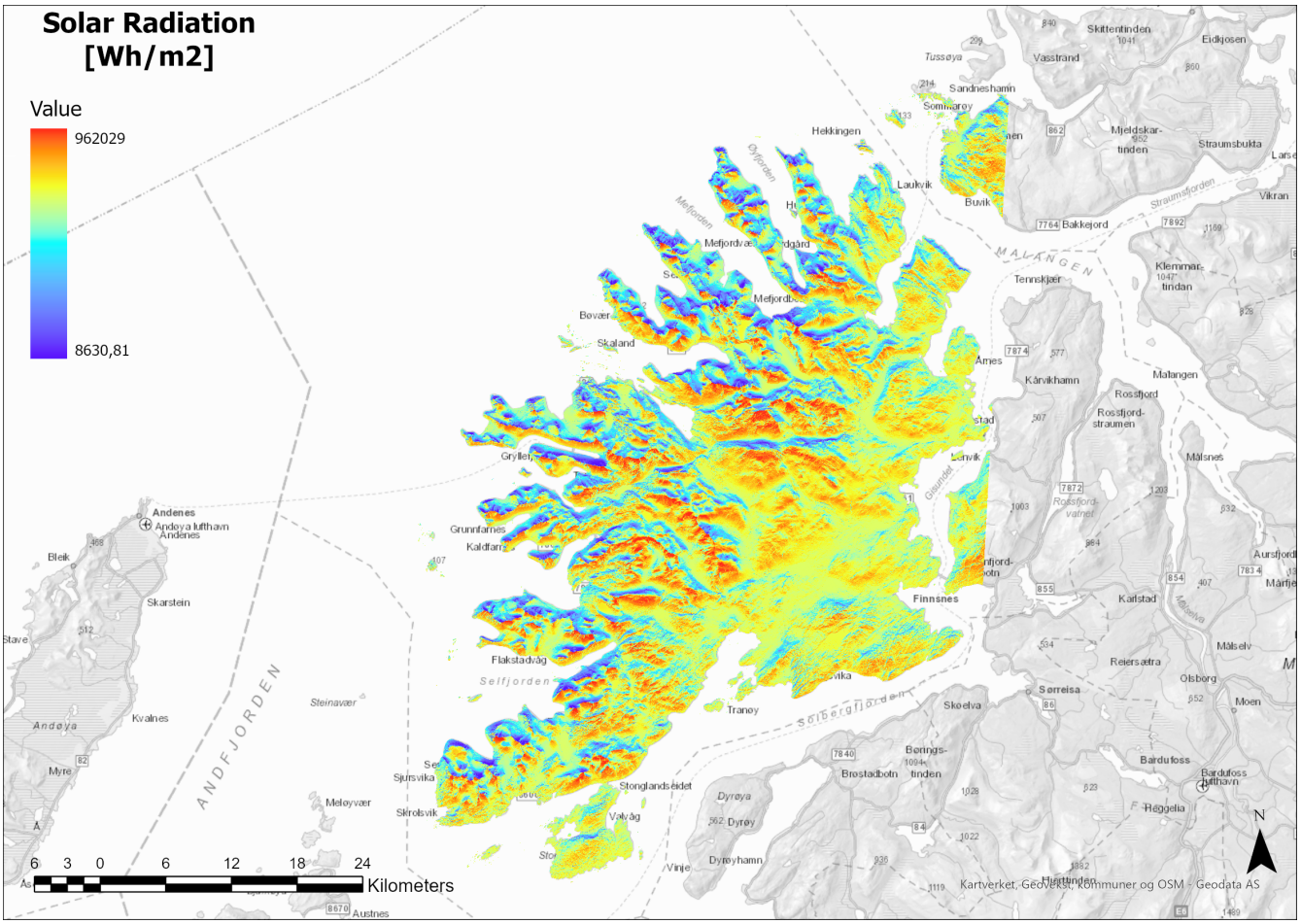

Figure B.3: Solar map of Senja, calculation is done in ArcGIS.

C / Python Code

C.1 Extraction From AROME-Arctic

```
import requests
from itertools import product
import threddsclient
import numpy as np
import matplotlib.pyplot as plt
import netCDF4 as nc
from pyproj import Proj
import pandas as pd
import xarray as xr
import datetime as dt
import timeit
from IPython import display

PROJ_LCC = '+proj=lcc +lat_0=77.5 +lon_0=-25 +lat_1=77.5 +lat_2=77.5 +no_defs +
    R=6.371e+06'
PROJ_LATLON = '+proj=longlat +ellps=WGS84 +datum=WGS84 +no_defs'

#Convert to lat/lon and opposite
def LatLon_To_XY(Lon,Lat):
    p1=Proj(PROJ_LCC, preserve_units=True)
    (x,y)=p1(Lon,Lat)
    return(x,y)

def XY_To_LatLon(x,y):
    p1=Proj(PROJ_LCC, preserve_units=True)
    (lon,lat)=p1(x,y, inverse=True)
    return(lon,lat)

start = timeit.default_timer()

```

```
years= list(range(2020,2022))
months= list(range(1,13))

coor1 = LatLon_To_XY(10.0, 68.95)
coor2 = LatLon_To_XY(20.0, 69.62)
coor = LatLon_To_XY(17.659755, 69.544514)

def grid_data(years, months, coor1, coor2):
"""
A function which scans the Threddsclient server at MET for the given years and months.
The selected parameters needs to be set in for "selected_parameter", such as x_wind_10m...
It returns the selected parameter in a grid format.
"""

    urls = []
    for y, m in product(years, months):
        catalog = f'https://thredds.met.no/thredds/catalog/aromearcticarchive/{y:04d}/{m:02d}/catalog.html'
        if requests.get(catalog).status_code == 200:
            datasets = threddsclient.crawl(catalog, depth=1)
            urls += [ds.opendap_url() for ds in datasets if '_pp_' in ds.name]

        print('url ', y, m)
        display.clear_output(wait=True)

    parameter= []
    for i in range(len(urls)):
        ds=xr.open_dataset(urls[i])
        dsloc = ds.sel(x=slice(coor1[0],coor2[0]), y=slice(coor1[1], coor2[1]))
        x=dsloc['selected_parameter'][0:3]#tid
        parameter.extend(x['selected_parameter'].values)

        print('parameter', i+1, len(urls), urls[i])
        display.clear_output(wait=True)

    for i in range(1):
        ds=xr.open_dataset(urls[i])
        dsloc = ds.sel(x=slice(coor1[0],coor2[0]), y=slice(coor1[1], coor2[1]))
        lat = dsloc.variables['y'][:]
        lon = dsloc.variables['x'][:]
```

```
69
70
71
72      return parameter, lon, lat
73  stop = timeit.default_timer()
74  print('Time: ', stop - start)
75
76  #######
77
78  start2 = timeit.default_timer()
79
80  def data_nearest_point(years, months, coor, file_name):
81  """
82  A function which scans the Threddsclient server at MET for the given years and
        months.
83  The selected parameters needs to be set in for "selected_parameter", such as
        x_wind_10m...
84  It returns the selected parameter nearest the chosen coordinates.
85  """
86
87      urls = []
88      for y, m in product(years, months):
89          catalog = f'https://thredds.met.no/thredds/catalog/aromearcticarchive/{
        y:04d}/{m:02d}/catalog.html'
90          if requests.get(catalog).status_code == 200:
91              datasets = threddsclient.crawl(catalog, depth=1)
92              urls += [ds.opendap_url() for ds in datasets if '_pp_' in ds.name]
93
94      parameter= []
95      for i in range(len(urls)):
96          ds=xr.open_dataset(urls[i])
97          dsloc = ds.sel(x=coor[0],y=coor[1], method ='nearest')
98          x=dsloc['selected_parameter'][0:3]#tid
99          parameter.extend(x.['selected_parameter'].values)
100
101     Edata = pd.DataFrame({'selected_parameter':parameter ,index=time)
102     Edata['selected_parameter'] = Edata['selected_parameter'].str.get(0))
103     Edata.sort_index(inplace=True)
104     Edata.to_excel('%s.xlsx' % file_name)
105
106     return parameter
107
```

```
stop2 = timeit.default_timer()
print('Time: ', stop2 - start2)
```

C.2 The BESS Algorithm

```
def Peak_shaving(data, SOC_max, SOC_min, SOC, eta, P_max, P_min, N, n_samples):
    """
    Peak load shaving for a given datase. The key parameters is inserted,
    and the loop runs to find the optimal uf at the given timestep.
    N: the size of the movingmean.
    """
    P_avg = np.convolve(data, np.ones(N)/N, mode='valid')
    P = data
    tau = 1
    uf = 1

    tstart = 0
    k = tstart-1
    true = 0
    i = tstart -1

    Pbess = np.zeros([len(P_avg)])
    SOCg = np.zeros([len(P_avg)])
    SOCp = np.zeros([len(P_avg)])

    while true < 1:
        i += 1
        k += 1

        Es = (P[i] - P_avg[i]) *uf
        Ebat = Es
    # Checking if Ebat exceeds P_max or P_min
        Pbat = eta*Ebat/tau
        if Ebat > P_max:
            Pbat= eta*P_max
        elif Ebat < P_min:
            Pbat = eta*P_min
    # Calculating the SOC
        SOC = SOC + Pbat
        SOCg[i] = SOC

    # Limits the SOC
```

```
38          if SOC <= SOC_min:
39              SOC = SOC_min
40              Pbat = 0
41          elif SOC >= SOC_max:
42              SOC = SOC_max
43              Pbat = 0
44      # Calculating the new SOC and Power
45          Pbess[i] = Pbat
46          SOCp[i] = 1-(SOC/SOC_max)
47          if k == tstart + n_samples:
48              if np.in1d(0, SOCp[tstart:tstart + n_samples]) == 1: #checking the
    max SOC is reached in new SOC
49                  i = tstart -1
50                  uf = uf-0.01
51                  k=tstart-1
52                  SOC = .5 * SOCmax
53
54                  Pbess = np.zeros([len(P_avg)])
55                  SOCg = np.zeros([len(P_avg)])
56                  SOCp = np.zeros([len(P_avg)])
57              else:
58                  true=1
59      #Calculating the new load profile and returns it
60      load_ps = P[tstart:tstart + n_samples] - Pbess[tstart:tstart + n_samples]
61      return load_ps, Pbess, SOCg, SOCp
```

Bibliography

[Andrews et al., 2021] Andrews, J., Andrews, J. G., Jelley, N. A., and Jelley, N. (2021). *Energy science: principles, technologies, and impacts*. Oxford university press.

[Asuero et al., 2006] Asuero, A. G., Sayago, A., and Gonzalez, A. (2006). The correlation coefficient: An overview. *Critical reviews in analytical chemistry*, 36(1):41–59.

[Bengtsson et al., 2017] Bengtsson, L., Andrae, U., Aspelien, T., Batrak, Y., Calvo, J., de Rooy, W., Gleeson, E., Hansen-Sass, B., Homleid, M., Hortal, M., et al. (2017). The harmonie–arome model configuration in the aladin–hirlam nwp system. *Monthly Weather Review*, 145(5):1919–1935.

[Birkeland et al., 2020] Birkeland, I., Fløtre, I., Bergland, L.-A., and Skeie, O. (2020). Batterier i distribusjonsnettet. *Norges vassdrags- og energidirektorat*.

[BKK, 2021] BKK (2021). Bli kjent med strømnettet. https://nett.bkk.no/artikkel/7f59a21f-cdbd-454e-a5c0-d13173cb6bd4 [accessed: 12.12.2021].

[DNV, 2019] DNV, G. (2019). Strømnettet i et fullelektrisk norge. *Teknisk rapport, okt*.

[Eikeland, 2019] Eikeland, O. F. (2019). Investigation of photovoltaic energy yield on tromsøya by mapping solar potential in arcgis. Master's thesis, UiT The Arctic University of Norway.

[Elbilforening, 2019] Elbilforening, N. (2019). Ladeklart norge 2025.

[Energy Facts Norway, 2019] Energy Facts Norway (2019). Electricity production. https://energifaktanorge.no/en/norsk-energiforsyning/kraftproduksjon/#hydropower [accessed: 31.05.2022].

[Energy Facts Norway, 2021] Energy Facts Norway (2021). The electricity grid. https://energifaktanorge.no/en/norsk-energiforsyning/kraftnett/ [accessed: 25.05.2022].

[Esri, 2022] Esri (2022). What is gis? https://www.esri.com/en-us/what-is-gis/overview [accessed on 30.04.2022].

[Falklev, 2017] Falklev, E. H. (2017). Mapping of solar energy potential on tromsøya using solar analyst in arcgis. Master's thesis, UiT The Arctic University of Norway.

[Fraunhofer Institute for Solar Energy Systems, 2022] Fraunhofer Institute for Solar Energy Systems, I. (2022). Photovoltaics report. *Fraunhofer, ISE*.

[Freund and Wilson, 2003] Freund, R. J. and Wilson, W. J. (2003). *Statistical methods*. Elsevier.

[Gao, 2015] Gao, D. W. (2015). *Energy storage for sustainable microgrid*. Academic Press.

[Grange, 2014] Grange, S. K. (2014). Averaging wind speeds and directions. *no. October*, page 12.

[Hersbach et al., 2018] Hersbach, H., Bell, B., Berrisford, P., Hirahara, S., Horányi, A., Muñoz-Sabater, J., Nicolas, J., Peubey, C., Radu, R., Schepers, D., et al. (2018). Era5 hourly data on single levels from 1979 to present. copernicus climate change service (c3s) climate data store (cds). https://cds.climate.copernicus.eu/cdsapp#!/dataset/reanalysis-era5-single-levels?tab=overview [accessed: 14.04.2022].

[Homer Energy, 2020] Homer Energy (2020). Homer pro user manual. https://www.homerenergy.com/products/pro/docs/latest/how_homer_calculates_the_pv_array_power_output.html [accessed: 09.05.2022].

[Honsberg and Bowden, 2019] Honsberg, C. and Bowden, S. (2019). Photovoltaics education website. https://www.pveducation.org/ [accessed: 30.05.2022].

[Jacobsen, 2019] Jacobsen, T. T. (2019). Distributed renewable generation and power flow control to improve power quality at northern senja, norway. Master's thesis, UiT The Arctic University of Norway.

[Jung and Schindler, 2019] Jung, C. and Schindler, D. (2019). The role of air density in wind energy assessment–a case study from germany. *Energy*, 171:385–392.

[Kirkeby and Seljeseth, 2014] Kirkeby, H. and Seljeseth, H. (2014). Utfordrende elektriske apparater. *Sintef Energi AS,[Internett]. Available: http://www. sintef. no/contentassets/8f3be4a5285b4a7a85a2987a9d397615/rapporter/9.3 _kirk eby_ henrik—utfordrende-elektriske-apparater. pdf.[Funnet 11 2014]*.

[Løvvold, 2020] Løvvold, I. (2020). Pumped hydropower conversion and renewable hybrid power plants at senja. Master's thesis, UiT The Arctic University of Norway.

[Machowski et al., 2008] Machowski, J., Lubosny, Z., Bialek, J. W., and Bumby, J. R. (2008). *Power system dynamics: stability and control*. John Wiley & Sons.

[Mallet and David, 2016] Mallet, C. and David, N. (2016). Digital terrain models derived from airborne lidar data. In *Optical Remote Sensing of Land Surface*, pages 299–319. Elsevier.

[Manwell et al., 2010] Manwell, J. F., McGowan, J. G., and Rogers, A. L. (2010). *Wind energy explained: theory, design and application*. John Wiley & Sons.

[Masters, 2013] Masters, G. M. (2013). *Renewable and efficient electric power systems*. John Wiley & Sons.

[MIT, 2008] MIT, E. (2008). A guide to understanding battery specifications. *Retrieved from Massachussetts Institute of Technology: http://web. mit. edu/evt/summary_ battery_ specifications. pdf*.

[Nagsarkar and Sukhija, 2014] Nagsarkar, T. and Sukhija, M. (2014). *Power system analysis*. Oxford university press.

[Norwegian Meteorological Institute, 2019] Norwegian Meteorological Institute (2019). About arome-arctic. https://www.met.no/en/projects/The-weather-model-AROME-Arctic/about[accessed: 10.02.2022].

[NVE, 2019] NVE (2019). Kraftproduksjon. https://www.nve.no/energi/energisystem/kraftproduksjon/ [accessed: 31.5.22].

[NVE, 2021] NVE (2021). Tema kart. https://temakart.nve.no/link/?link=nettanlegg [accessed: 31.05.2022].

[Olje- og energidepartementet, 2020] Olje- og energidepartementet (2020). Forskrift om leveringskvalitet i kraftsystemet.

[Rahimi et al., 2013] Rahimi, A., Zarghami, M., Vaziri, M., and Vadhva, S. (2013). A simple and effective approach for peak load shaving using battery storage systems. In *2013 North American Power Symposium (NAPS)*, pages 1–5. IEEE.

[REC, 2020] REC (2020). Technical datasheet twinpeak 2 mono series.

[REC, 2022] REC (2022). Technical datasheet alpha series.

[Robson and Bonomi, 2018] Robson, P. and Bonomi, D. (2018). Growing the battery storage market 2018. In *Energy Storage World Forum*.

[Royce, 2021] Royce, R. (2021). Battery energy storage system. https://www.mtu-solutions.com/eu/en/applications/power-generation/power-generation-products/energy-storage-system.html.

[Saadat, 2010] Saadat, H. (2010). Power system analysis.

[Saheb et al., 2014] Saheb, D., Koussa, M., and Hadji, S. (2014). Technical and economical study of a stand-alone wind energy system for remote rural area electrification in algeria. *Renewable Energy and Power Quality Journal*, 1(12):638–43.

[Sjømaklyngen Senja, 2021] Sjømaklyngen Senja (2021). Energiforbruk i sjømatregion senja 2016-2030 (versjon ii, januar 2021).

[Smart Senja, 2021] Smart Senja (2021). Smart senja, fremtidens energisystem. https://smartsenja.no/ [accessed: 30.05.2022].

[Smets et al., 2015] Smets, A. H., Jäger, K., Isabella, O., Swaaij, R. A., and Zeman, M. (2015). *Solar Energy: The physics and engineering of photovoltaic conversion, technologies and systems*. UIT Cambridge.

[SSB, 2021] SSB (2021). Elektrisitet. https://www.ssb.no/energi-og-industri/energi/statistikk/elektrisitet [accessed: 31.05.2022].

[Sunpower, 2022] Sunpower (2022). Technical datasheet maxeon.

[Thurner et al., 2018] Thurner, L., Scheidler, A., Schäfer, F., Menke, J., Dollichon, J., Meier, F., Meinecke, S., and Braun, M. (2018). pandapower — an open-source python tool for convenient modeling, analysis, and optimization of electric power systems. *IEEE Transactions on Power Systems*, 33(6):6510–6521.

[TKN, 2020a] TKN (2020a). 132 kv kraftledning silsand/brensholmen - til ny transformatorstasjon ved botnhamn konsesjonssøknad med konsekvensutredning.

[TKN, 2020b] TKN (2020b). Regional kraftsystemutredning for område 21.

[TKN, 2021] TKN (2021). Årsrapport 2021. *HOVEDRAPPORT*.

[Troms Kraft, 2019] Troms Kraft (2019). Sluttrapportering på konseptutredning.

[Wikantika, 2018] Wikantika, K. (2018). Three dimensional city building modellingwith lidar data (case study: Ciwaruga, bandung).

[Willmott and Matsuura, 2005] Willmott, C. J. and Matsuura, K. (2005). Advantages of the mean absolute error (mae) over the root mean square error (rmse) in assessing average model performance. *Climate research*, 30(1):79–82.

[WindEurope, 2022] WindEurope (2022). Wind energy in europe: 2021 statistics and the outlook for 2022-2026. *WindEurope*.